Seismic Imaging using Image Point Transform
for Borehole Seismic data

Lab. of Engineering Geology,
Dept. of Civil and Earth Resources Engineering,
Kyoto University, Japan

Changhyun Lee

July, 2008

IP 変換を利用した坑内弾性波データにおける弾性波イメージング

京都大学大学院工学研究科
社会基盤工学専攻地質工学分野

李昌鉉

2008 年 7 月

Abstract

As the progress of the technology, geophysical prospecting has succeeded in advance of data acquisition and analysis and has enlarged its' application areas to not only oil and gas exploration but also civil and environmental engineering, GIS, disaster prevention and safety test of the structures. The main goal of geophysical prospecting may be said to reconstruct the imaging of survey area and investigate the physical properties and their relation like velocity, resistivity, density, porosity and so on. With those results, it is possible to give useful information to determine the drill point of oil and gas exploration, to design of the structures of bridges, tunnels and buildings and to evaluate the change and the distribution of CO2 sequestration.

Borehole seismic survey like Vertical seismic profiling (VSP), reverse VSP (RVSP) and crosswell tomography is one method of the prospecting and has the position in the resolution and the coverage of the survey between the surface survey and the borehole logging because of use of one or more borehole in data acquisition.

Borehole seismic surveys have some difference in the geometry of field acquisition but follow almost same processing in data analysis and interpretation. These processing are based on the reflection seismic techniques. As the imaging method, VSP-CDP mapping and migration schemes of Kirchhoff and wave propagation has been applied and given considerable results.

However, the concept of image point (IP) transform has been reported by Cosma and Heikkinen and the application for the multi-offset VSP data has showed the validity of IP transform. IP transform is one type of Radon transform, but has different integral path. Radon transform integrates the data on time-space domain along the path of the straight line whereas IP transform lies does according the hyperbolic path Thus, transformed data of Radon lies on the τ-p (intercept time - inverse velocity) domain and the data of IP transform lies on space-space.

The basic concept and properties of IP transform are confirmed by applying synthetic data of various models and source-receiver geometries. The IP of reflection waves are accumulated on IP domain because of the hyperbolic integral path. Because of this accumulation of reflection waves by the transform, the signal to noise (S/N) ratio is enhanced in IP domain and the reconstructed waves of the reflection by inverse IP transform is much more distinguishable than the original reflection waves.

The characteristics of several filters in IP domain are investigated, e.g. muting, wave separation and dip filter. By definition of IP transform, the position of sources

might be seem not to affect on the IP transform but the only dips and the dips and strikes of the reflectors in some cases can be defined with the information of the reflection on IP domain and sources. The dip filter using discrimination of each reflection on IP domain is applied and the reflection wave of the specific dip is separated by inverse transform. Some waves like multiple, refractions and tube waves are difficult to be separated in common gather. It is known by applying synthetic data and field data of VSP that these are easily dealt with in IP domain. The IP of multiples by the surface and tube waves of down going are located upper parts of ξ (receiver axis of IP domain) in VSP. These wave separations are also useful tool to enhance the S/N ration of the data.

As one of RVSP geometry, that is, receivers are planted on the surface and sources are placed in the downhole, radial location of receiver lines is considered. Trough applying synthetic data of two dipping reflector model in homogeneous model, the interesting and important thing is found that the positions of ρ-distance of the origin and IP- of one reflector in IP domain are invariable over all receiver lines but the positions of ξ-location in axis of IP- are variable. Moreover, the vertical projections of those ξs cross one point which is located on perpendicular line to the strike of the reflector. With this property, the transform is developed, that is, IP transform to an arbitrary line and this are named generalized IP transform. The generalized IP transform is valid to search the vertical direction of the strike of reflectors or to be a mid-step to image the reflector if the information of the strike is known.

Conventional imaging methods like VSP-CDP mapping, equal travel time and migration are mapping or imaging the reflection point or related point to the reflection. The mapping method of mid-point between the IP of reflection and the source is developed in this paper. The mid-point mapping is derived from the fact that the mid-point between IP of reflection and a source is located on the reflector. The reflection does not happen at the mid-point and the mid-point is decided by the IP and the source not by receivers. Basically, the mid-point mapping has the characteristic of accumulating the imaging point, therefore the full information of the reflector is difficult to be determined by only one source however it is possible for the conventional methods in synthetic data. The weak point can be overcome by increasing the source points and multi-sources survey are common recently. The capability of the mid-point mapping scheme as a imaging tool is confirm the result of application to the synthetic data and field data

Contents

List of Figures

Chapter 1

Introduction

1.1. Background and Purpose

Geophysical prospecting becomes a common and essential method to imaging the underground. In early stage of the geophysical prospecting, it is developed to find the geological structures in oil and gas exploration field. Recently, its' uses are expanded to the various fields such as, civil and environmental engineering, GIS, disaster prevention of land slide, earthquake and tsunami and safety test of the structures.

Geophysical survey scheme would be roughly divided into three fields, that is, surface survey, borehole survey and borehole logging. Generally, the coverage of the survey area is the widest in the surface survey and the accuracy of data is the highest in the borehole logging. The borehole surveys like VSP, RVSP, crosswell and tomography may be narrower than the surface survey and less precise than the borehole logging but in other word, they are better than the opposite sides. Borehole seismic schemes are known to give more accurate and precise results than the surface survey schemes and cover wider survey area than the logging. VSP, RVSP and crosswell are different in geometries of sources and receivers but they are sometimes similar in the data processing and imaging.

Vertical Seismic Profiling (VSP) survey was firstly proposed for oil and gas exploration as a subsurface imaging tool by using check-shot data and it had achieved successful results (Van Schaack, 1995; Zhang et al, 1997; Gulati et al, 2004). Since then VSP has been widely applied to the geotechnical problems like the monitoring of CO2 sequestration, site survey for high-level radioactivity material disposal and identifications of fracture zone in tunneling (Cosma and Heikkinen, 1996, Ashida et al, 1998, Matsuoka and Ishikaki, 2005). Also the reverse VSP (RVSP) method was proposed and it is opposite to VSP in the geometries of sources and receivers. Sources are set in the borehole and receivers are set at the surface.

The data processing and imaging methods for VSP data are expanded from the surface reflection seismic methods. Among imaging methods, the concept of VSP common depth point (CDP) is common and it is widely adopted (Watty and Watty, 1981; Cheng *et al.,* 2000). Kirchhoff migration scheme (Dillon, 1988) and common image gather method (Biondi and Tisserant, 2004) are also applied to mapping the VSP data. Ashida *et al.,* (1998) also succeed to image the geological fracture in horizontal tunnel site by using the concept of equal travel time plane mapping.

Cosma and Heikkinen (1996) and Cosma and Enescu (2002) showed a good imaging result for steep dip fractures from offset VSP data. In their research, they introduced the idea of the image point (IP) transform. Offset VSP data are transformed into IP domain and some processing like polarization analysis and dip analysis are applied in this domain. Imaging results are obtained with the reconstructed data by the inverse IP transform after these processing.

This study is focused on expanding the IP transform in various geometries and clarifying those characteristics. For the purpose, at first the expansion of the IP transform in RVSP is investigated theoretically and the new transform concept named the generalized IP transform is derived and the new mapping methods of the mid-point imaging of the sources and the IP of the reflection is introduced. Secondly, the data are synthesized for the various models in 2-D and 3D and those are used to analysis the basic concept of the IP transform and the mid-point mapping scheme. Finally, the application to the field data of VSP, RVSP and crosswell acquisitions is conducted and the characteristics investigated in numerical studies are confirmed.

1.2. Outline of the dissertation

Chapter 1 is introduction of this research, including the background and the objective. The outline of this paper is also summarized.

Chapter 2 consists of the theoretical background of this research. In the early part of this chapter, the basic concept and the uses of the transforms used in geophysical field are explained. The later, the Radon transform which is the origin of the Image Point (IP) transform, is described. The last part of this chapter is involved with the explanation of the IP transform. The IP transform derived by Cosma (1996) is reviewed and is expanded to the 3-D RVSP case. Generalize IP transform is also derived in 3D-RVSP when the geometry of sources is placed in radiation. The mapping scheme of the mid-point between the IP and the source is explained.

Chapter 3 consists of the 2-D and 3-D numerical modeling and those IP transform to understand the characteristics of the IP transform. At first, the numerical modeling is done for the simplest model of horizontal two-layer model and the basic concept of the IP transform is discussed. These studies are carried out for more complicated but still simple model of one dipping reflector to understand the change of the reflection in IP domain according to the dip angle of the reflector. Two dipping reflector model in RVSP scheme is also investigated and the mapping method of the mid-point between the IP and the source are discussed. As the most complicated case of 2D model, the data is synthesized for six reflectors model with various dipping angles in VSP scheme and the reflection wave of each reflector is discussed in IP domain. 3D model of two dipping reflector in RVSP where receivers are placed radially is adapted and the IP transform and the generalized IP transform are done to confirm those properties in IP domain which are derived and discussed in chapter2. The applicability of the mid-point mapping scheme for this model is also addressed.

Chapter 4 discusses the applicability of the transform for the three cases of 3D RVSP, VSP and crosswell filed data. First, in RVSP data where receivers are almost placed radially, the characteristics of the generalized IP transform of the reflection is mainly discussed. Second, in multi-offset VSP case, the capability of the IP transform as a filter is discussed by comparing with the commonly used filters. Especially, these are done for the tube wave removal, that is, the tube wave removal in IP domain is compared with filters like the velocity filter (F-K filter) and Eigenvalue filter. The mid-point mapping scheme is also discussed by comparing the imaging results of Kirchhoff migration. Finally, the conventional processing is performed for the crosswell data and the model is reconstructed by the result. Synthetic data is achieved for the model and the feature of the reflection is addressed by comparing the data in IP domain of the synthetic and field data.

In chapter 5, the conclusions of this study are summarized and some comments for the future work are addressed.

Chapter 2

Image Point Transform

2.1. Transform

Transform means to convert one function like observed data on one domain to on another domain, for example, observed data in time series to in frequency domain by Fourier transform. Many transforms in geophysical field like Fourier transform, Radon transform, image domain transform and so on, are used to enhance the signals of data or imaging result and make them to be more clearly understood. For example, we encounter frequently noises in field data caused by power line, micro-ground move, car and human activities and correlated signals by different propagation ray path. In these cases, we might mute or delete the clear noisy data in time domain but in much more cases, it is much easier and more efficient to deal the data in frequency domain rather than time domain.

Fig 2-1 illustrates the advantage of dealing the data in frequency domain than time domain. Fig 2-1(a) is the simulation result of three different dip reflectors in time domain, (b) is the result of 2D Fourier transform and inverse transform result after muting one event in frequency domain is shown in Fig 2-1(c). All of Fig 1 are calculated by Seismic Un*x (Cohen and Stockwell, 2001) which is published by CWP (Center for Wave Phenomena, Colorado School of Mines)

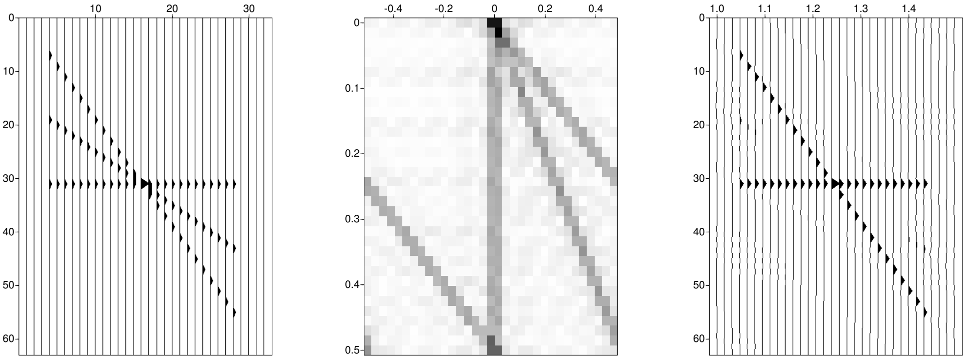

(a) Common offset (b) 2D Fourier transform (c) filtered result

Fig 2-1 Example of transform for three dip reflector model.

As we know this example, we can also classify 3 waves of different velocities in time domain but if we want to eliminate the mid velocity event in time domain, we face some difficulty even if it might be possible to mute the signal inside of the lowest and highest velocity signal in Fig2-1 (a). Whereas the three waves in frequency domain are much more discriminated than in time domain (Fig2-1(b)) and elimination is also much easier and it's well know as velocity filter in f-k domain.

2.2. Radon Transform

Radon transform is commonly used in geophysical data processing and its' forward and inverse transform equation are given by (Anger and Portenier, 1992)

$$R(p,\tau) = \int g(x, y = \tau + px)dx \qquad (1)$$

$$g(x,y) = \frac{1}{2\pi}\int \frac{d}{dy} H(R(p, y - px)dp \qquad (2)$$

Here, p is slope and τ is intercept point on y axis. As illustrated Fig 2-2, Radon transform converts the data in (x,y) domain to (p, τ) domain, and the integral is conducted along the line with the slope p and intercept.

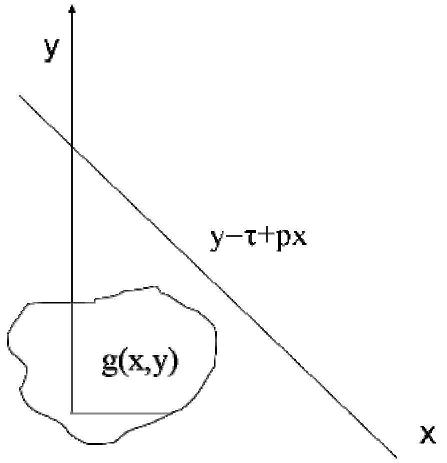

Fig 2-2 Schematic diagram of Radon transform

In seismogram which is recorded data in space-time domain, y is changed to time, t, and p and τ in equation (1) can be interpreted respectively to the slowness, that is, inverse of velocity, and the intercept time. The Radon transform is also called as called tau-p transform because of parameters of the equation or slant stack because of the characteristics of the integral path.

Let's consider a simple case, that is, a plane wave source and receivers for homogeneous medium as shown in Fig 2-3. Here, we set the velocity of the medium as v then the inverse of the horizontal phase velocity, also kwon as the ray parameter, p is given by

$$p = \frac{1}{v_{hor}} = \frac{\Delta t}{\Delta x} = \frac{\sin\theta}{v} \qquad (3)$$

Here, is v_{hor} the horizontal velocity and θ is the incident angle of plane wave at receivers. As we infer by definition, Radon transform decomposes the wave into the plane wave components.

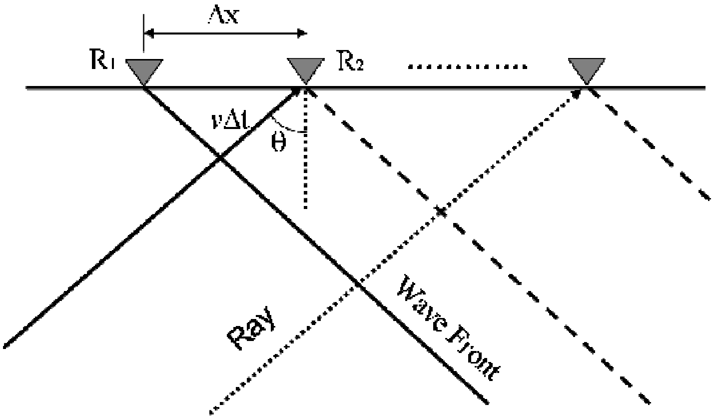

Fig 2-3 Schematic diagram of plane wave

The synthetic seismogram shown in Fig2-1(a) is the simulation result of three different dip reflectors model, then it also can be thought as the reflection result of a three different apparent velocity, that is, different slowness. So, the result of Radon transform is accumulated in three parts on tau-p domain as illustrated in Fig 2-4.

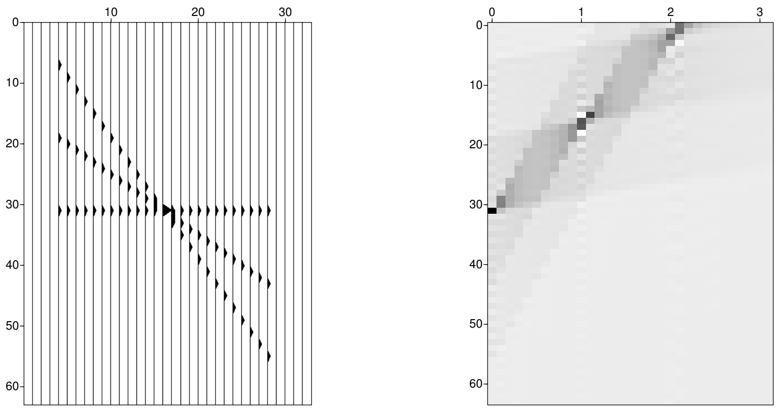

(a) Common offset results (b) Radon transform result

Fig 2-4 Example of Radon transform for three dip reflections

The most focused parts of Radon transform in Fig2-4 coincide with the intercept time and slowness of three reflectors. Assuming that the plane wave propagates vertically to the depth, the difference of apparent velocities-horizontal velocities- or slowness is caused by the dip of reflectors. The dips of three reflectors can be calculated by the equation (3), that is, the steeper a reflector is, the slower an apparent velocity would be.

2.3. Image Point Transform

Let us consider more general but simple two horizontal layer model as illustrated in Fig 2-5, and source is the delta function, δ(t) excited at 0 time. Then the first reflection at a receiver R, *g(x,t)* is given by

$$g(x,t) = \delta(t - t_0),(t_0 = \frac{\sqrt{x^2 + 4D^2}}{v_1}) \qquad (4)$$

Here, D is the depth of the first reflector and x is offset which is distance between a source and a receiver. Radon transform of the common shot gather *g(x,t)* is expressed by substituting equation(4) for (1).

$$R(p,\tau) = \delta(px + \tau - \frac{\sqrt{x^2 + 4D^2}}{v_1}) \qquad (5)$$

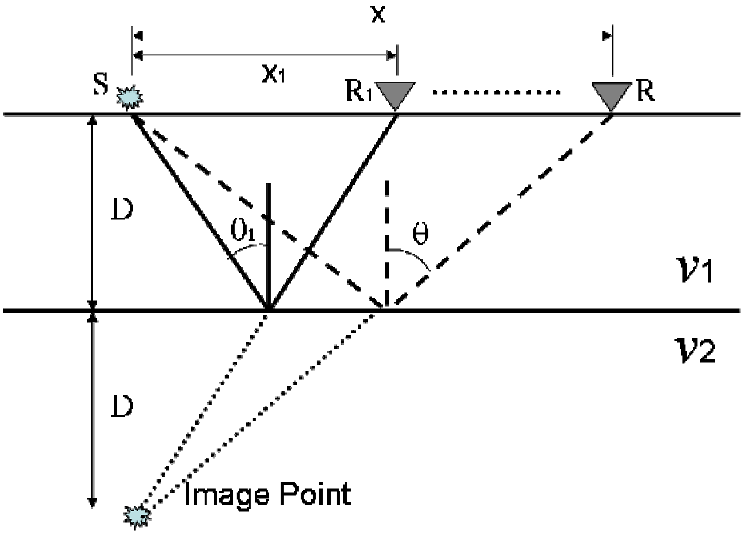

Fig 2-5 Two layer model

Let us change the view point of the integral of the Radon transform. Instead of integration along the slope and intercept in Radon transform, integrating along the time t_0 path changes equation (4) to an equation like below equation (5).

$$I(\rho,\xi)=\int_{t_0}\delta(t-t_0)dx=\delta(\rho-2D) \qquad (5)$$

Here, $t_0=\sqrt{x^2+\rho^2}/v_1$ and ξ is the axis same to the receivers line. As seen in equation (5), the seismogram is focused at one point and that point is the imaginary point called the image point (Fig 2-5). Fig 2-6 illustrates the concept of this transform named image point transform. Radon transform is used to suppress multiples and linear noises like ground roll (Yilmaz, 1987), so image point transform derived from Radon transform is also available and has similar characteristics.

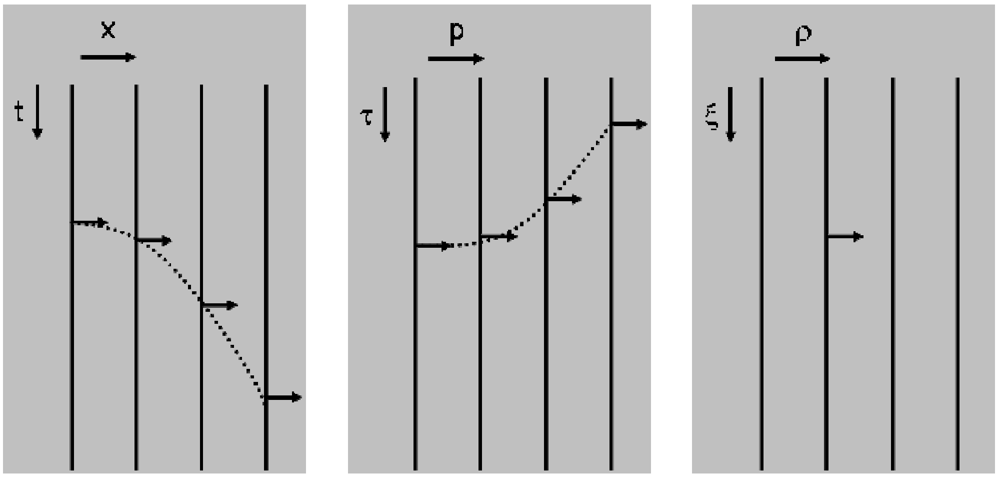

(a) Seismogram (b) Radon transform (c) Image Point transform

Fig 2-6 Illustration of transforms

Let us consider more generalized case of one reflection plane in homogeneous medium in order to simplify the discussion (Fig 2-7). IP transform is derived in case of vertical seismic profile (VSP), which converts time-space domain signal to geometrical space domain (Cosma and Heikkinen, 1996). In this paper I expand this transform to RVSP data set. Geologically we can consider this reflection plane is an isolated fracture plane in the homogeneous rock mass. In this simple case, the image point (IP) for one source is defined geometrically as shown in Fig 2-7 as the mirror image point of the source with respect to the reflection plane. Also the mid point is defined as the central position between the source and the IP and it is on the reflector plane. In Fig 2-7, the origin of the coordinate, (0,0), is set at the borehole head and x and ξ are the surface receiver line axis and the source inside the borehole is at d in ζ axis.

The IP transform for RVSP data set can be given by the following equation

$$I(\xi,\rho)=\int g(x,t=t_r(\rho,\xi;x))dx \qquad (6)$$

Here, g(x,t) is a common shot gather and t_r is the total travel time from a source to a reflection point and to a receiver position which is equal to the travel time from the image point (IP) to the receiver position at surface. If velocity is symbolized by *v*, travel time can be expressed as follows:

$$t_r = \sqrt{\zeta^2 + (\xi - x)^2} / v = \sqrt{\xi^2 + \zeta^2 + x^2 - 2x\xi} / v \qquad (7)$$

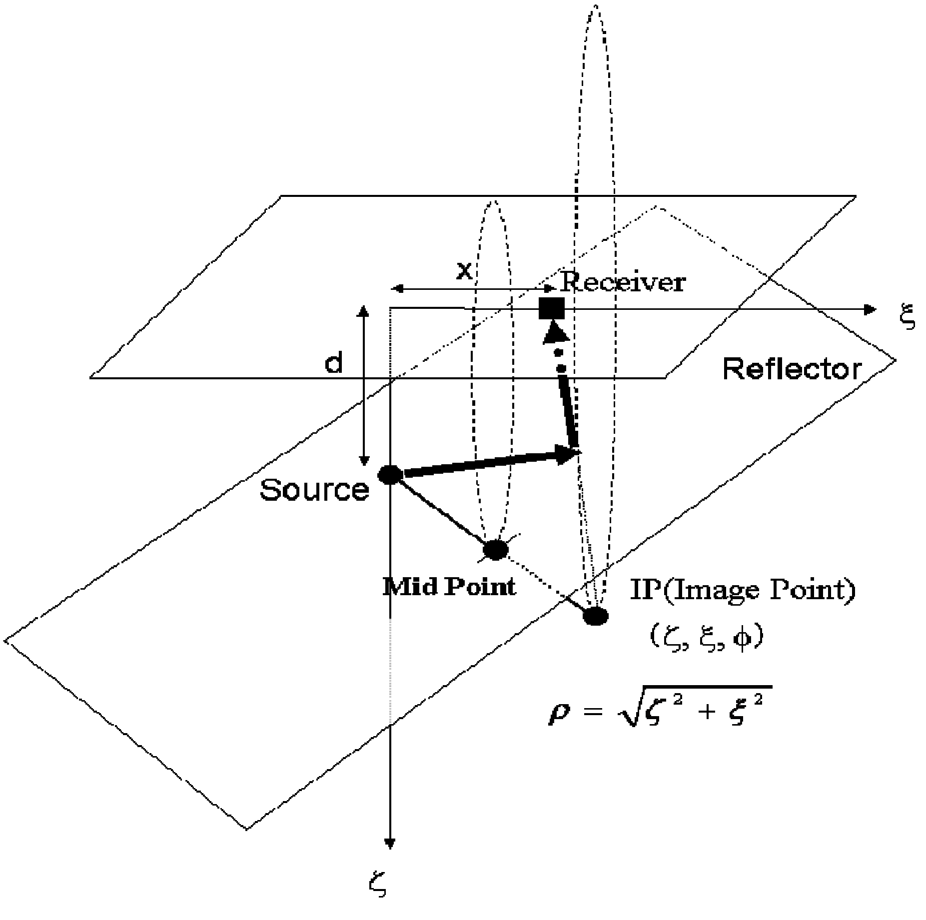

Fig 2-7 Schematic of Image Point for RVSP case of 3D

If ρ is considered as the distance from the origin, (0,0), to the image point, equation (7) can be written as:

$$t_r = \sqrt{\rho^2 + x^2 - 2x\xi} / v \qquad (8)$$

By applying IP transform to the RVSP data set with the assumption of given velocity information, the reflected signals are focused to the image point while other signals like noises are less enhanced.

Like Radon transform, we can define the inverse IP transform and it is expressed as equation (9).

$$g(x,t) = \frac{1}{2\pi v^2 t} H_t \frac{\partial}{\partial t} \int I(\xi; \rho = \rho r(x,t;\xi)) d\xi \tag{9}$$

Here, H_t means Hilbert transform and ρ_r is written as follows.

$$\rho_r = \sqrt{v^2 t_r^2 - x^2 + 2x\xi} \tag{10}$$

2.4. Generalized IP transform

Let us consider one source, receivers and one reflector which are illustrated in Fig 2-8. One source is located z in depth and two receivers symbolized by colors red and green rectangles are on axis ξ_1. The axis ξ_0 is vertical to the strike of a reflector and the angles ϕ_0 and ϕ_1 are the rotation angles from the reference axis to the axes ξ_0 and ξ_1 respectively.

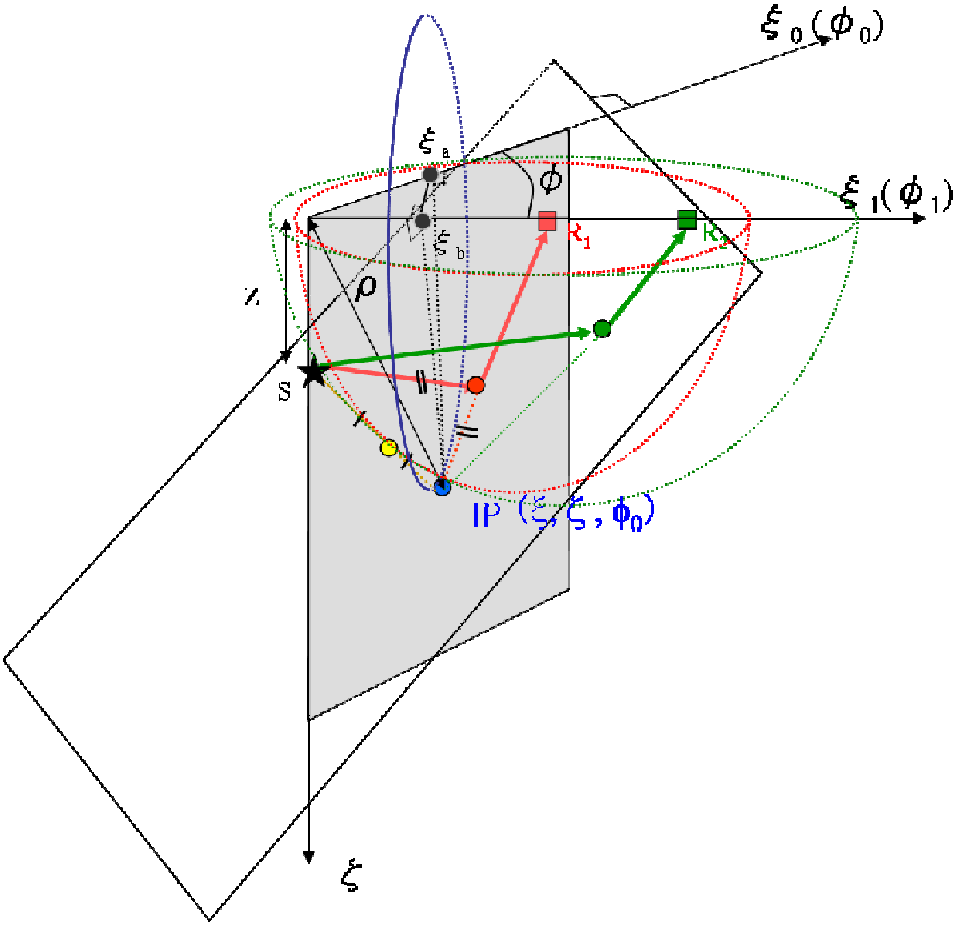

Fig 2-8 Schematic diagram of generalized IP transform

As the definition of the image point and addressed above section, the image point of one reflector and one source is uniquely determined. In this case, we can imagine one plane which contains the image point and the vertical axis of the strike of a reflector and it is illustrated with gray color in Fig 2-8. Let us set ξ_a and ξ_b as the projection of the image point to the axes ξ_0 and ξ_1 respectively, then the line connecting ξ_a and ξ_b is perpendicular to the axis ξ_1. That is undoubtedly true because ξ_a is also the projection to the surface plane. Therefore, the plane including the ξ_a, ξ_b and the image point is perpendicular to the line on this plane of ξ_a and ξ_b and is also vertical to the axis ξ_1. Let consider the angle between two axis ξ_0 and ξ_1 as ϕ, then the relation of ξ_a and ξ_b is expressed by

$$\xi_b = \xi_a \cos\phi \tag{11}$$

By the definition of the image point, the travel times of reflection from a source(S) to receivers are equal to the times from the image point to receivers. Assuming that the travel times is considered as $tr1$ and $tr2$ then, they are given by,

$$tr1 = \left|\overrightarrow{\mathrm{IP}} - \overrightarrow{\mathrm{R}_1}\right| / v\ , \qquad tr2 = \left|\overrightarrow{\mathrm{IP}} - \overrightarrow{\mathrm{R}_2}\right| / v \tag{12}$$

Here, v is the velocity.

If velocity is constant that is homogeneous medium and the travel time of reflection at receiver R_1 is known but the position of a reflector is unknown, therefore the position of the image point is also unknown. Then, the image point of a reflection lies on the semi-sphere illustrated as red semi-sphere in Fig 2-8 by the equation (12). It can be also done for a receiver R2 and illustrated as green semi-sphere. The intercept points of two red and green semi-spheres, which are the equal travel time plane from each receiver, consist in a semi-circle drawn as blue circle. A circle is illustrated here instead of a semi-circle for convenience. For the receivers lied on one line, the intercept points of all equal travel time planes lie on only one semi-circle and the semi-circle is located in the plane which consists of ξ_a, ξ_b and the image point. Generally, the image point of one reflector is determined by three equal travel time planes whose receivers don't lie on one line.

If the IP transform of receivers of one line is defined, it's also possible to convert the IP transform to the vertical direction line of a reflector by equation (12) and is given by

$$
\begin{aligned}
GI(\xi_0,\rho) &= \begin{pmatrix} 1/\cos\phi & 0 \\ 0 & 1 \end{pmatrix} I(\xi_1,\rho) \\
&= \begin{pmatrix} 1/\cos\phi & 0 \\ 0 & 1 \end{pmatrix} \int g(x, t = t_r(\rho,\xi_1;x))\,dx
\end{aligned}
\tag{13}
$$

It can be generalized to one receiver and is useful in case the receivers are distributed irregularly or lines of receivers are curved. This generalization is done by determining the angle of a rotation as the angle between the vertical axis of a reflector and the line of the origin to a receiver point. If the strike of a reflector is unknown which is the case in common field data or only known limited to geometry of a reflector, this transform would be also available by assuming the vertical direction and converting all image points to this direction. Because the transformed images of a one image point are accumulated in only one direction which is perpendicular to the strike of a reflector. The image point transform from one direction to the vertical direction of a reflector is named as generalized image point transform.

2.5. Mapping using IP transform

The subsurface imaging technique with the VSP or RVSP data are mainly from conventional reflection imaging concepts like VSP-CDP (Watty and Watty, 1981; Yilmaz , 1987; Cheng *et al.,* 2000), and Kirchhoff migration scheme (Dillon, 1988). The VSP-CDP transform concept converts the data to reflection position by calculating the travel time. The method of equal travel time methods is also applied to horizontal seismic profiling (HSP) survey which is geometrical equal to VSP (Ashida *et al.,* 1998). The isochron image scheme (Hubral et al, 1996; Tygel et al, 1996) and inversion for VSP(Dewangan and Grechka, 2003; Slawinski et al, 2004, Grechka and Mateeva,2007)scheme are applied .

Conventional VSP-CDP method transforms the data recorded at X1 and X2 to the common depth point (CDP) by calculating the travel time of reflection points (Fig 2-9). Let us assume the model and geometry drawn in Fig 2-9 then, CDP for X1 and X2 are determined as the points of projection R1 and R2 on X axis. The final image of true reflection points is given by migration. The equal travel time scheme get the image by projection the data of sources and receivers geometry into the equal travel time plane drawn as red ellipses in Fig 2-9.

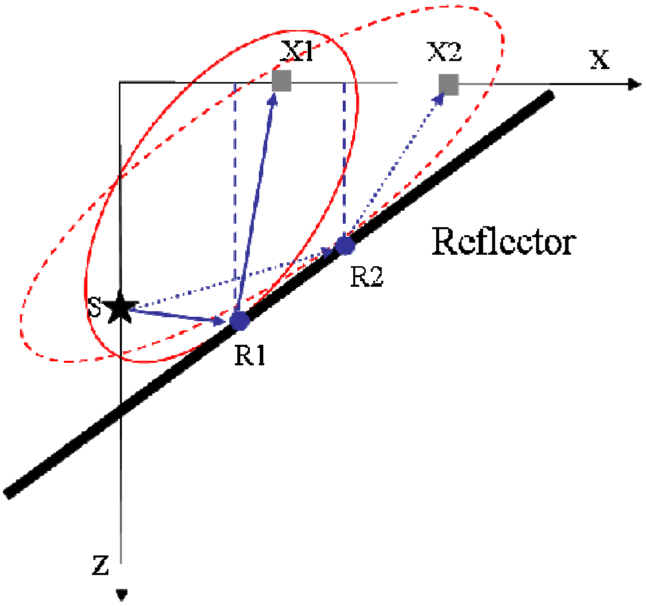

Fig 2-9 Conventional VSP imaging methods

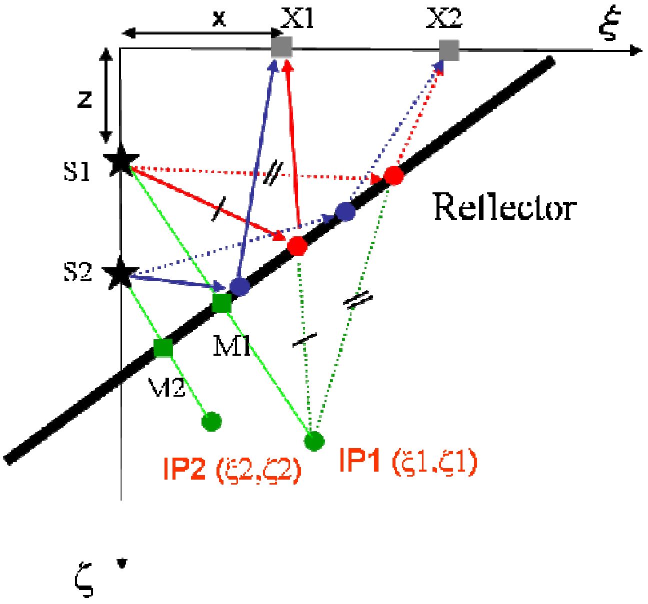

Fig 2-10 Mapping method using image point

Cosma and Heikkinen (1996) applied IP transformed data as a mid-step to go to the imaging. That is, they transformed the original data to IP domain and some filters like dip filter and polarization analysis and inverted to the time domain data by inverse IP transform. We consider the new mapping concept which is somewhat different but efficient to the conventional imaging method as shown Fig 2-9 and 2-10. In conventional

VSP image methods, the cross points of reflecting wave and the reflector are imaged, but we use a fact, that is, the mid points of sources and IPs are also lied on the reflector nevertheless the reflection is not occurred in the mid point (Fig1). The mid point mapping method does not image the real reflection point but image one arbitrary point of a reflector. When using one source and one reflector data, the image by the mid point mapping is accumulated at one point so the dip and strike of a reflector can not be known. While the conventional imaging methods might be successful to get the image of a reflector using only one source. But the mid point mapping method also provides the information of dip and strike of a reflector if multi-sources are used. As seen in Fig 1, two point, M1 and M2 are the mid points of sources (S1,S2) and image points(IP1, IP2) respectively and lied same reflector, so that face makes us assume the dip angle. So the mid point is written as the following.

$$(\mathrm{X}_{\mathrm{m}},\mathrm{Y}_{\mathrm{m}})=(\frac{\xi}{2},\frac{(\zeta+S)}{2})=(\frac{\xi}{2},\frac{(\sqrt{\rho^2-\xi^2}+S)}{2}) \qquad (14)$$

Here, (X_m,Y_m) is mid point of a source(S) and an image point(ρ,ξ), and ρ is distance of the origin of the coordinate (0,0) and an image point.

Chapter 3

Characteristics of IP transform on numerical data

3.1. 2D model

In this section, three different models, horizontal layer model, one dipping reflector model, two dipping reflectors model and six variant dipping reflectors model are studied to understand the IP transform.

For horizontal layer model, the basic characteristics of IP transform of each wave like direct wave, multiples and reflected wave are surveyed. For dipping reflector models, IP of reflections according to changing the sources and receivers geometry are investigated and imaging method in IP transformed domain is also studied.

3.1.1. Horizontal layer model

Model

The Simple two horizontal layer model illustrated in Fig 3-1 is conducted to investigate the basic concept of IP transform. The simulation is conducted by staggered grid finite deference method of forth order scheme for space and which is widely used as an accurate computation scheme (Levander, 1988). Absorbing boundary condition (Clayton and Enquist, 1977;Shin, 1995) is added with 25 grids on the three boundaries of bottom, left and right side of model and the top of model is supposed the free surface.

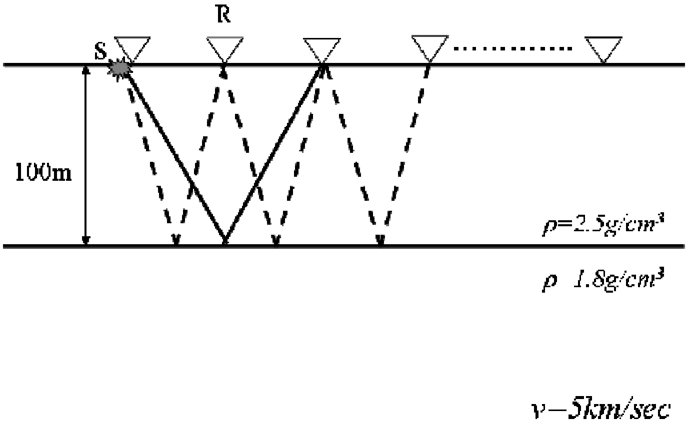

Fig 3-1 Horizontal layer model

The numerical modeling parameters are summarized in Table 3-1. Only acoustic wave-P wave- is considered in modeling and the density change is considered on the boundary of the layer for simplicity. 51 receivers are placed on the surface in every 10m interval and first receiver is positioned above the source set in (0m,5m).

Table 3-1 Model parameters

Model size	500m* 250m	Grid	1m * 1m
Time sampling	0.1msec	Calculation time	200msec
Density of 1st layer	2.5g/cm^3	Density of 2nd layer	1.8g/cm^3
Depth of two layer boundary	100m	Source position	(0m,5m)
Receiver No.	51	Source wavelet	Peak:100Hz Ricker wavelet

IP transform and inverse IP transform.

Numerical simulation result and its' IP transform are shown in Fig 3-2. Direct wave from the source is shown in the earliest time illustrated with the bold arrow and the reflection wave and its' multiples follow which are illustrated with dot arrow and dash-dot arrows in Fig 3-2(a).

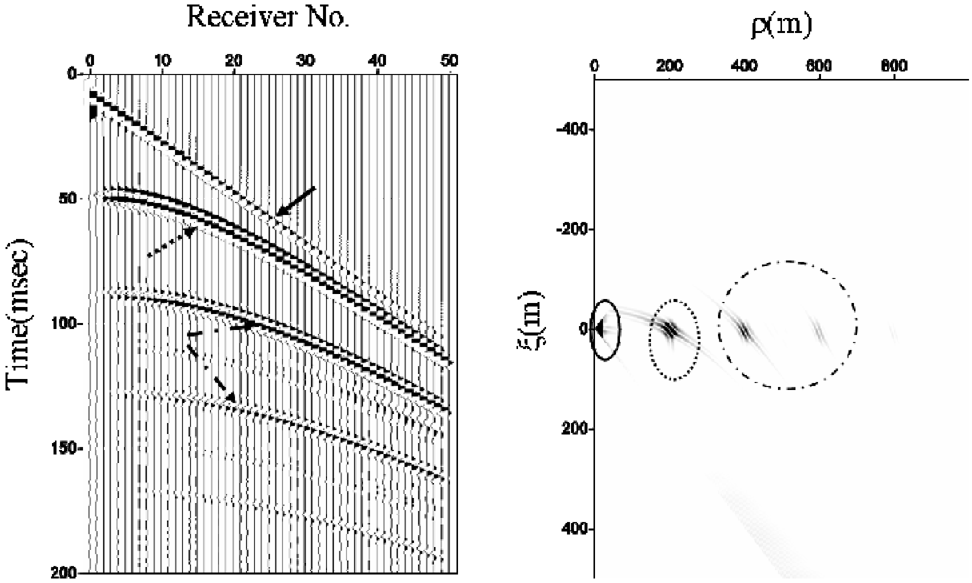

(a) Original wave (b) IP transform result

Fig 3-2 Simulation result and its' IP transform

As expected from the definition of IP transform, the IP transform results of every waves are accumulated in some areas (Fig 3-2(b)). The parts drawn with line, dot and dash-dot represent direct wave, reflection and multiples respectively. The IP of reflection and multiples are positioned 0m in ξ axis and the ρ of each IP are changed. Because the model is a horizontal layer, the IPs of them are placed below the source in depth and the distance from the origin to IPs, that is ρ, varies only. The positions of IP of reflection can be calculated by simple math and is (195m, 0m) in IP transform domain (ρ–ξ domain) because the IP of the reflection are below the source and the distance from the source to the boundary of the layer are same as that from the IP to the boundary. The IP of multiples are also done with the same and they are (395m, 0m) for first multiple and (595m, 0m) for second multiple(Fig 3-3). As shown in Fig 3-2, the multiples are revealed sequentially after the reflection in original wave and IP domain and the interval of ρ is concerned with the depth of the first layer illustrated in Fig 3-3.

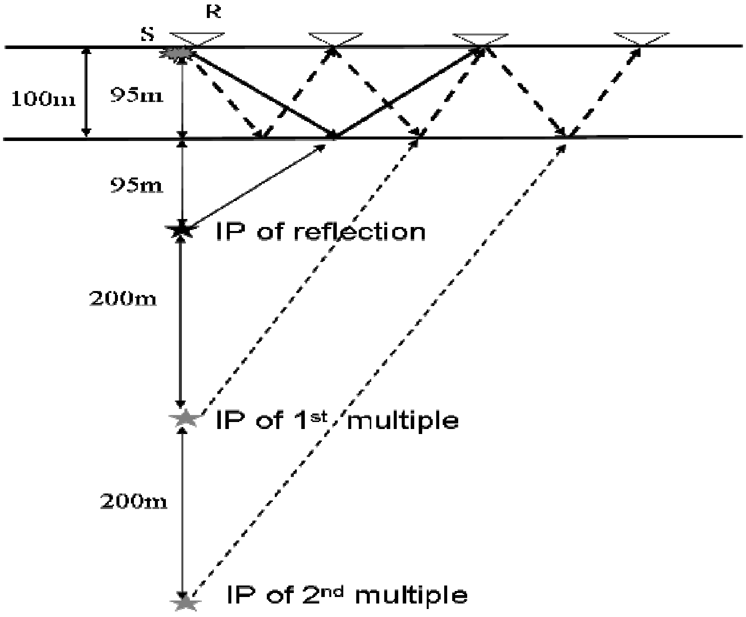

Fig 3-3 Schematic diagram of IP transform for reflection and multiples

If It’s possible to specify the wave in IP domain, It will be also possible to improve signal to noise ratio(S/N), extract and delete some wave in IP domain and reconstruct the waves by inverse IP transform. The example of inverse transform is shown in Fig 3-3 and it is done by inverse transform after extracting only the reflection wave in IP domain. As seen the result in Fig 3-4, direct wave and multiples are diminished in inverse transformed result (Fig 3-4(b)). The inverse transform of the first and the second multiples are shown in Fig 3-5. Some filters for example direct wave or multiple wave remove filter, can be considered in IP domain by these characteristics.

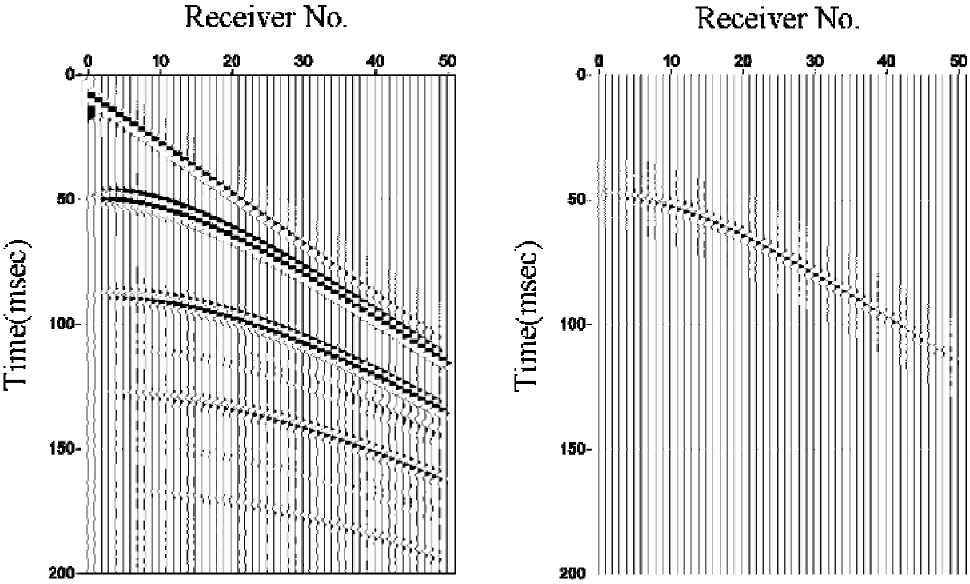

(a) Original wave (b) Inverse IP transform result

Fig 3-4 Result of inverse IP transform

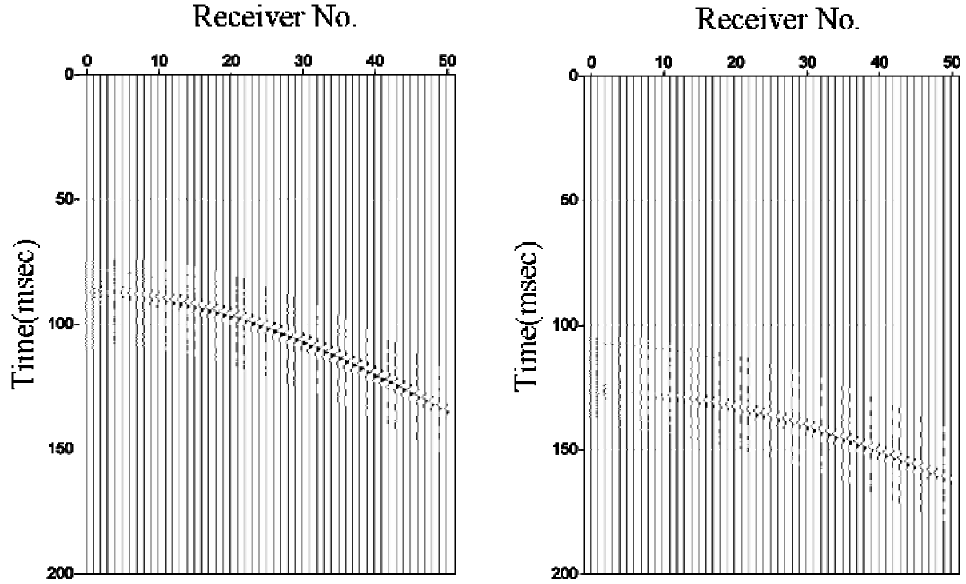

(a) 1st multiple (b) 2nd multiple

Fig 3-5 Result of inverse IP transform for multiples

Robust to the noise

In field survey, we frequently encounter the noise problems and some coherent noises are removed by the specific filters like the notch filter to remove the noise by power line, although some coherent noise masking the signal is hard to overcome. The noises which are difficult to remove are random ones, for example the noises by the traffics, construction area and human activity. In the recent researches, the survey using those noise sources are reported named passive seismic or seismic interferometry(Clauber, 1968; Wapannar, 2003; Shiraishi et al, 2007)

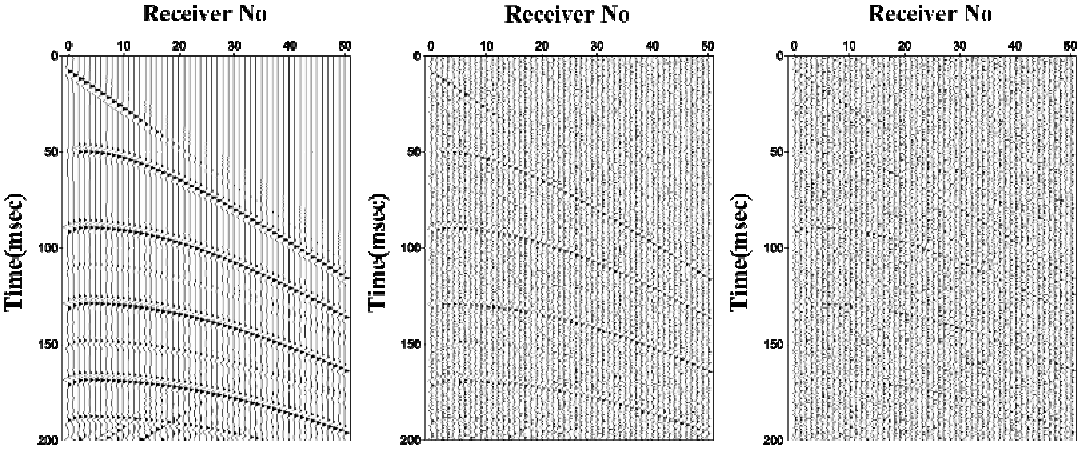

(a) Normalized wave (b) 50% noise (c) 100% noise

Fig 3-6 Waves with AGC and adding noise

To know the feature of the IP transform on noisy data, I apply the transform with the data illustrated in Fig 3-6 (b) and (c). Fig 3-6 (a) is the wave processed by auto gain control (AGC), which the window of gain is 100msec and free to noise. Fig 3-6 (b) and (c) are waves processed by AGC and random noise adding and the noise level are 50% (S/N ration is 2) and 100% (S/N ratio is 1) to the signal level respectively. Compared to the original wave (Fig 3-4(a)), the third multiple is much clearly seen and numerical noise are also enhanced in normalized wave (Fig 3-6(a)). The waves including noise are not clearer than the original wave and normalized wave although it is possible to distinguish the waves of reflection, direct and multiples.

The results of IP transform to the noise data is illustrated in Fig 3-7 and it can be addressed that the IP of reflection and multiples are well accumulated and enhanced. The reason why multiples are also enhanced by IP transform is that multiples have same features of the propagation. The numerical noises seen between the multiples and below the third multiples (Fig 3-6(a)), are also enhanced in IP domain illustrated in Fig

3-7, because these noises arise from the numerical boundaries and can be considered as the wave reflected in the boundaries.

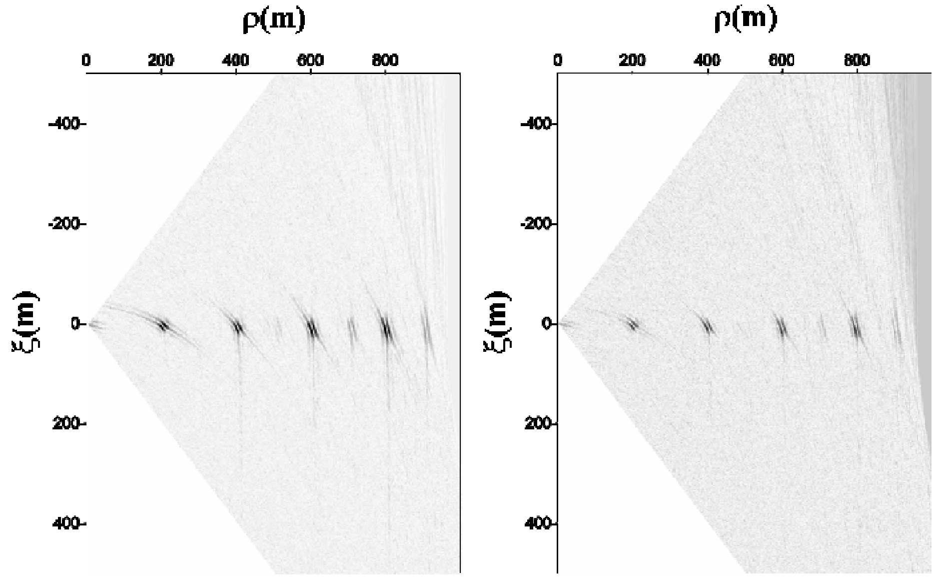

(a) S/N ratio 2 (b) S/N ratio 1

Fig 3-7 Result of inverse IP transform for multiples

Inverse IP transform results for the reflection wave and other waves are illustrated in Fig 3-8 and Fig 3-9. The process of inverse IP transform consists of two steps. First is to determine noise level in IP domain because noises are seen in IP domain although the reflections in IP domain (Fig3-6) are much more distinguishable than the reflection in Fig 3-7. Second, IP is separated to each wave like reflection, multiples and other waves, then inverse transform is applied to reconstruct the waves.

As seen in Fig 3-8 and 3-9, reflection and multiple are respectively separated and reconstructed. Compared to the result of S/N ratio 2(shown in Fig 3-8 and Fig 3-9 (a)) the inverse IP transform result of S/N ration 1(Fig 3-8 and Fig 3-9(b)) contains a little more noisy data but the reconstructed waves are more clearly seen than waves with noise illustrated in Fig 3-6 (b) and (c).

As explained in this section, if it is possible to determine the waves in IP domain, wave separation can be done by the inverse IP transform. It's also staged that IP transform are robust to the noisy data because of the nature of the IP transform, so the IP transform is useful tool to analyze and deal with the noisy data.

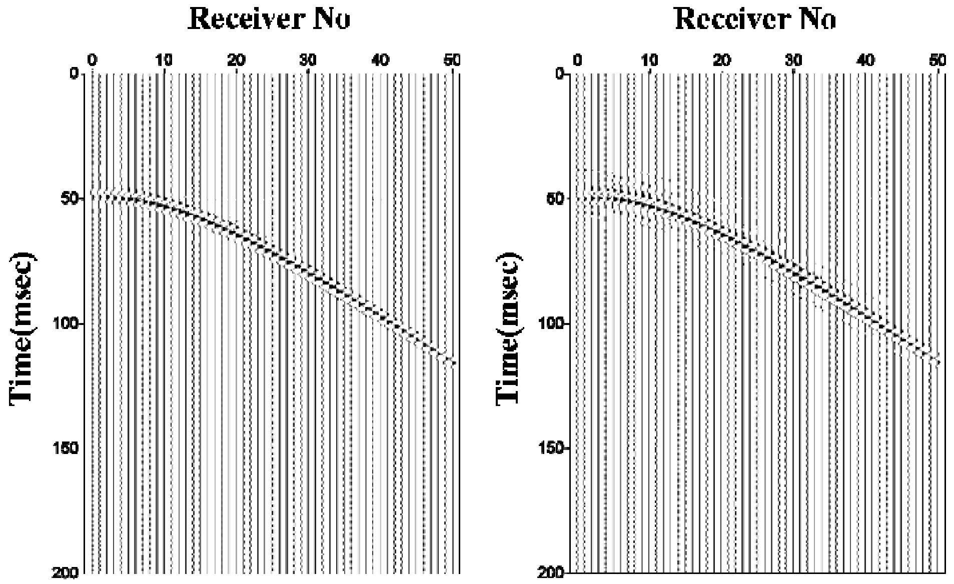

(a) S/N ratio 2 (b) S/N ratio 1

Fig 3-8 Inverse IP transform results of the reflection wave

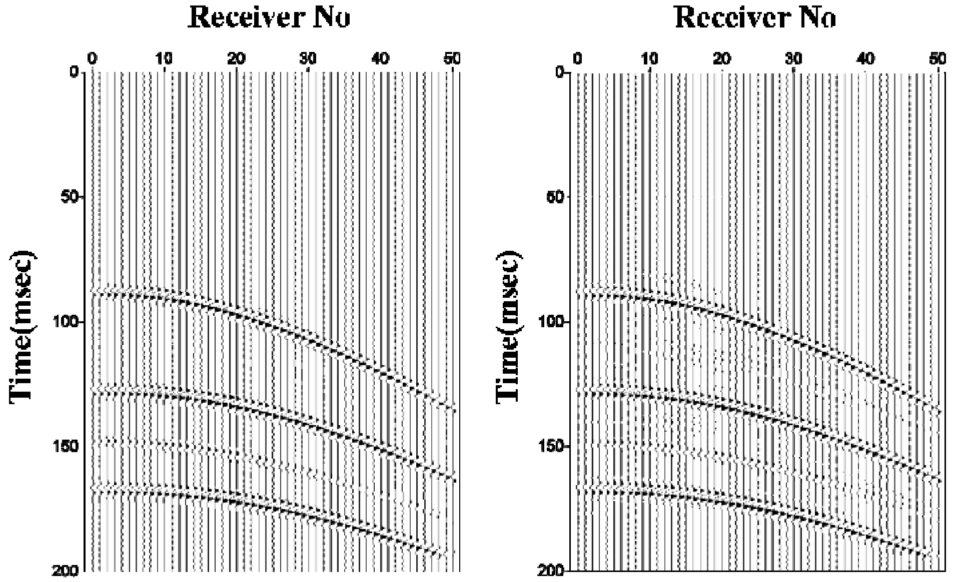

(a) S/N ratio 2 (b) S/N ratio 1

Fig 3-9 Inverse IP transform results of multiples

3.1.2. One reflector model

Numerical Modeling

To study applicability and characteristics of the IP transform, Numerical simulation for the 2D one reflector model is conducted. The dip angle of the reflector is 75° and the cross point with the surface is 200m (Fig 3-10). 100 receiver points are set on the surface and the interval of two receiver points are 10m. Other modeling parameter like source type, gird, sampling interval are same as those applied in the horizontal layer model explained in section 3.1.1. The velocity of background is set 5300m/sec and density change is added on reflector with 10grids. Numerical modeling is done for six sources depth, 50m, 100m, 200m, 300m, 400m and 500m.

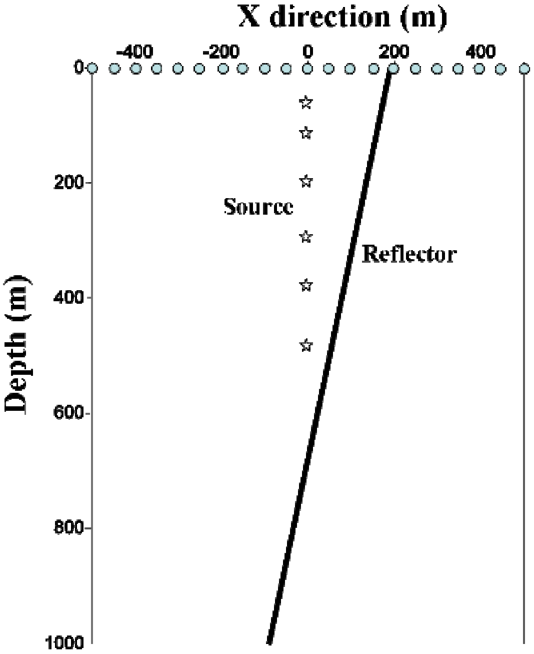

Fig 3-10 2D dipping reflector model

Modeling results are illustrated in Fig 3-11 and bold arrows represent direct waves while dot arrows represent reflection waves. Some waves started from left and right sides are numerical noises from the boundary. It is assumed that the geometry of sources and a reflector, the reflection wave is close to the direct wave as the sources go deeper. Because of this reason, the reflection wave of the shallow depth like 50m (Fig 3-11(a)) is similar to the straight line while that of deeper depth is hyperbola like drawn in Fig 3-11(e) and (f). This fact is also explained as the IP of each source, that is, the IP in case of source depth 50m is located close to surface while the IP of deeper source depth like 200m is deeper.

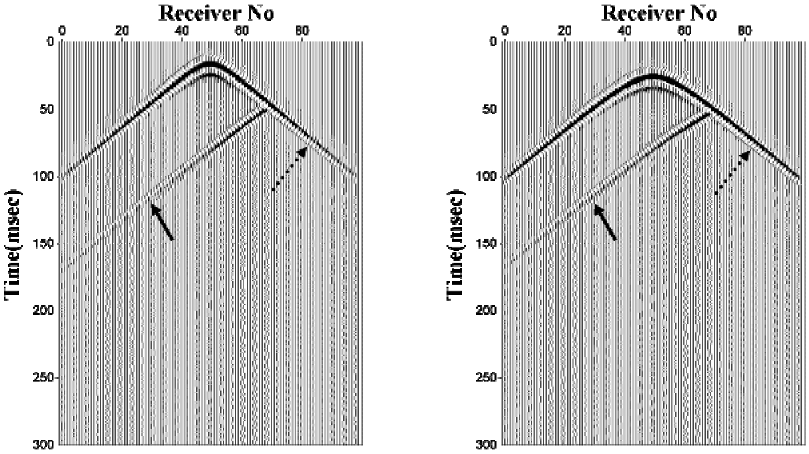

(a) source depth 50m (b) source depth 100m

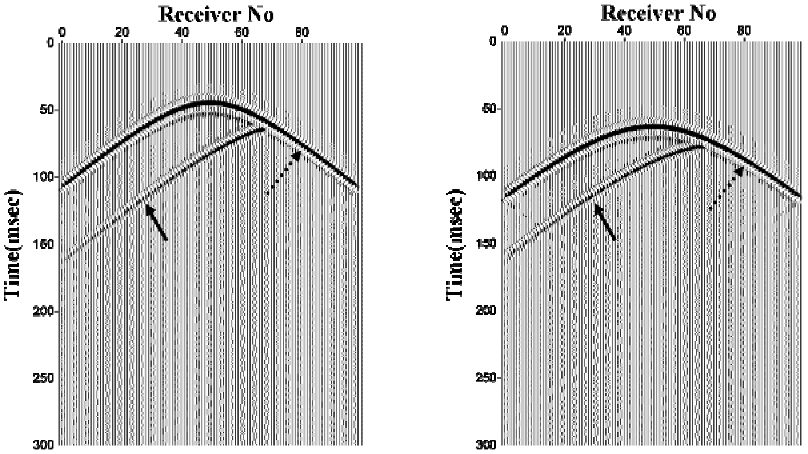

(c) source depth 200m (d) source depth 300m

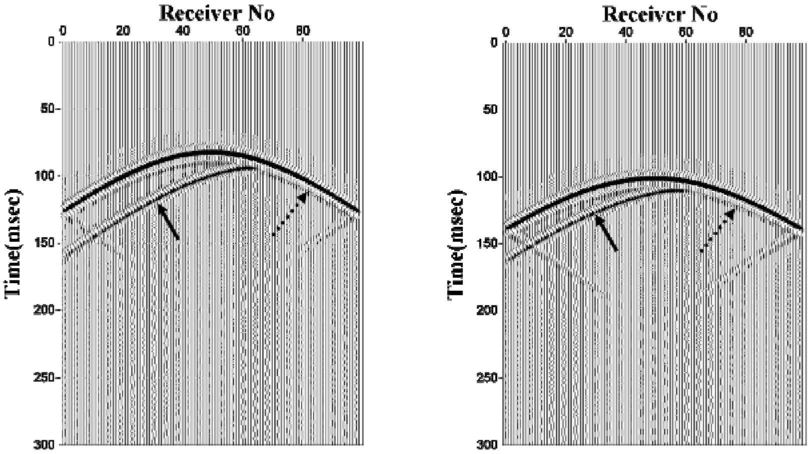

(e) source depth 400m (f) source depth 500m

Fig 3-11 Numerical simulation results of one dipping reflector model

IP transform

Fig 3-12 represents one example of the simulation result and its' IP transform result, when the source is located 200m at depth and 0m at x direction which is the center of the receiver line. In Fig 3-13, IP transform results of all six sources are presented. The line circles point the parts of the IP of reflection waves and dot-line circle those of the IP of direct waves.

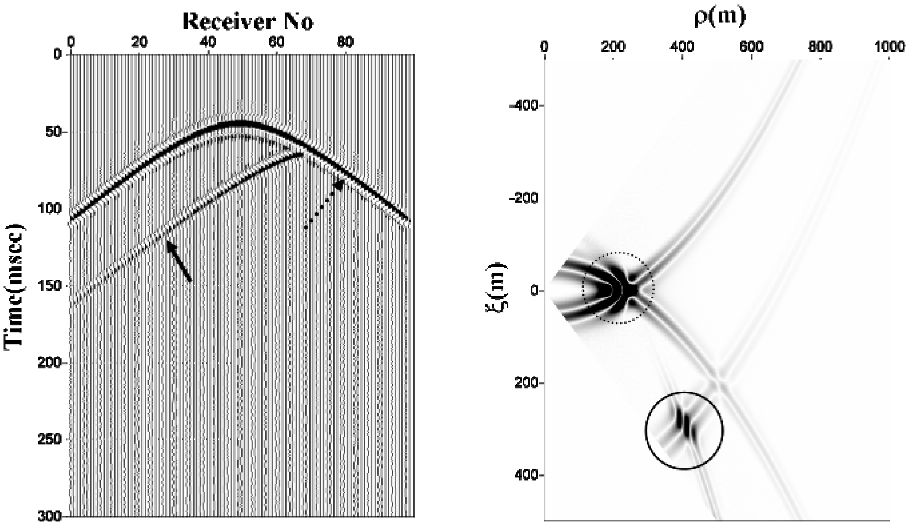

(a) Numerical Results (b) IP transform of data (a)

Fig 3-12 Example of numerical simulation and IP transform result for source depth 200m

The IPs of direct waves also increase in ρ and the parts of IP are wider, as the positions of the sources are deeper (Fig 3-13). The IPs of reflections change along the position both in ξ and ρ axis. The changes of the position in ξ axis indicate that the reflector is inclined and the dip angle of the reflector is concerned with changing rate of ξ in IP domain. If the reflector is horizontal like illustrated in Fig 3-1, the position of ξ axis of the reflections' IP will not change as the positions of sources' depth increase. There is no doubt that the ρ of reflections' IP decrease as the depth of sources increase in both cases dipping reflector model and horizontal reflector model.

It may be said that the decreasing rate of ρ in IP domain is also concerned with the dip of the reflector but it is impossible to know the direction of the reflector's dip with only the information of positions of ρ in IP domain.

While the information of position of x in IP domain complete the dip and direction of the reflector. These characteristics are discussed much more in next section.

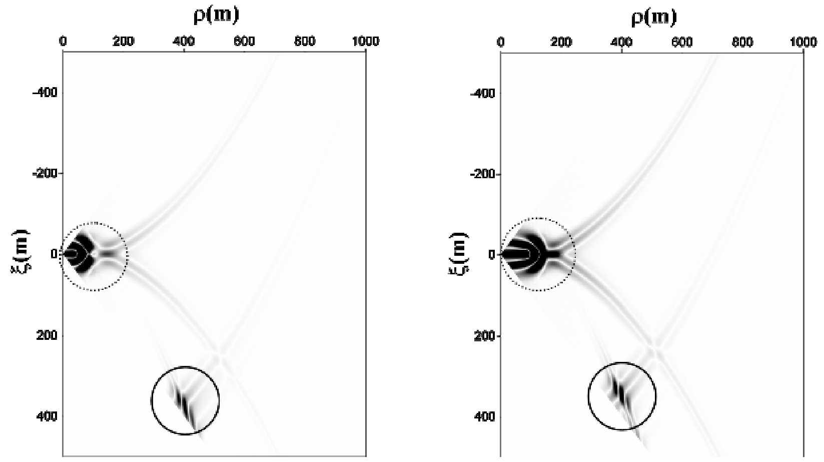

(a) source depth 50m (b) source depth 100m

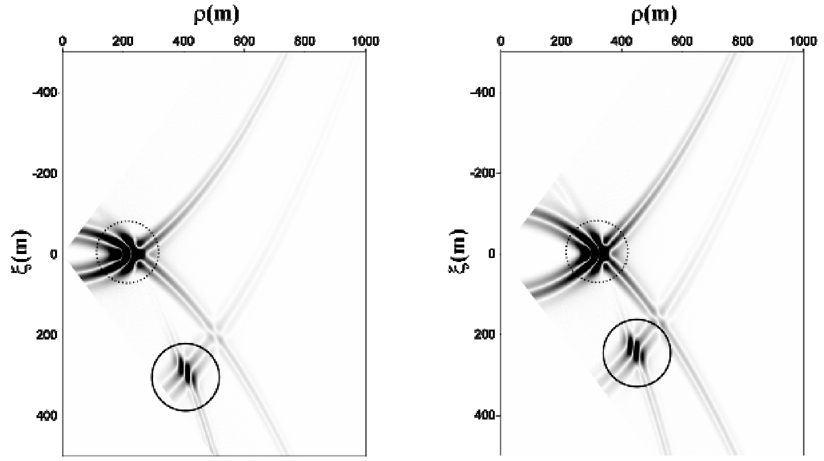

(c) source depth 200m (d) source depth 300m

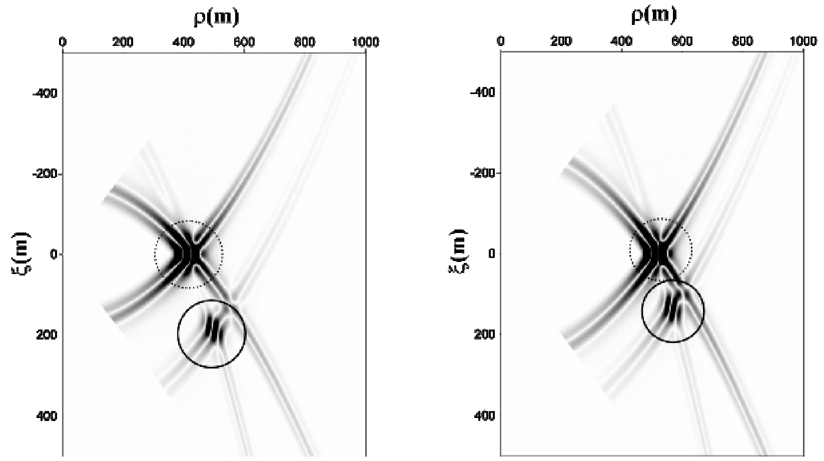

(e) source depth 400m (f) source depth 500m

Fig 3-13 IP transform results of one dipping reflector model

3.1.3. 2D two dipping reflectors model

Model

In previous section 3.1.2, the IP transform was applied to one dipping reflector model and its characteristics were discussed. In this section, a more complicated case is considered. That is a case with more than one reflector as illustrated in Fig 3-14. The simulation parameters of two dipping reflectors model are same to one dipping reflector model except for the additional reflector whose dip angle is 45°. As similar to the case of one reflector model, Reflector 1 and 2 intercept with the source depth direction at (0,746m).

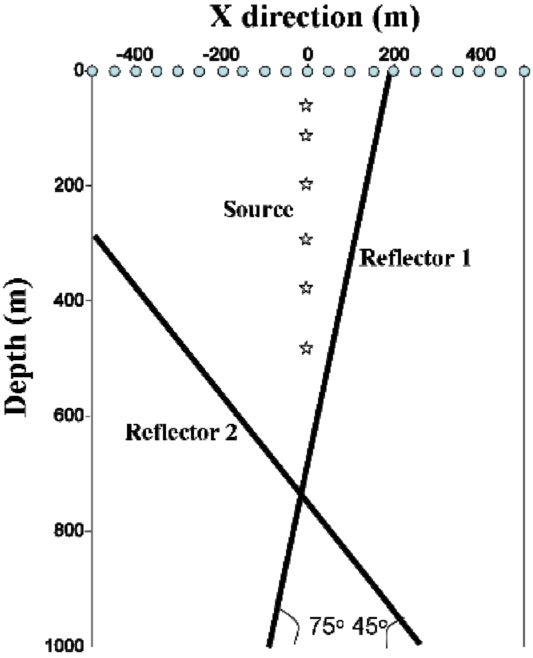

Fig 3-14 2-D two dipping reflectors model

Fig 3-15 represents the simulation results of six sources. Line arrows in Fig 3-15 point the reflection waves from Reflector1 and dot arrows point the reflection waves from Reflector2. Because of the direction of the dip of two reflectors, the refection from the Reflector 1 is inclined right to left and it is opposite for the Reflector 2.

Some waves shown under the reflection from the Reflector 2 are numerical noise and are caused by the numerical boundary and the numerical girds.

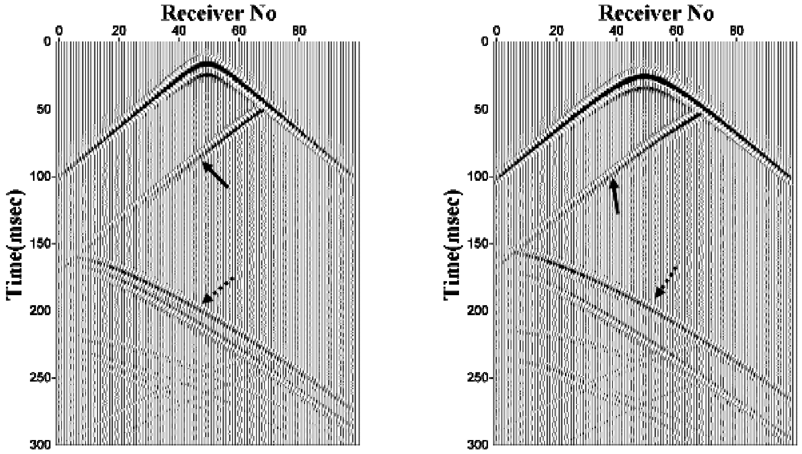

(a) source depth 50m (b) source depth 100m

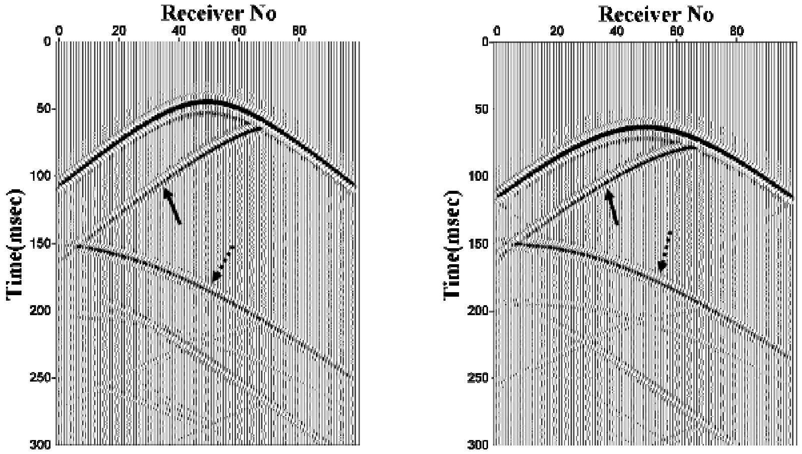

(c) source depth 200m (d) source depth 300m

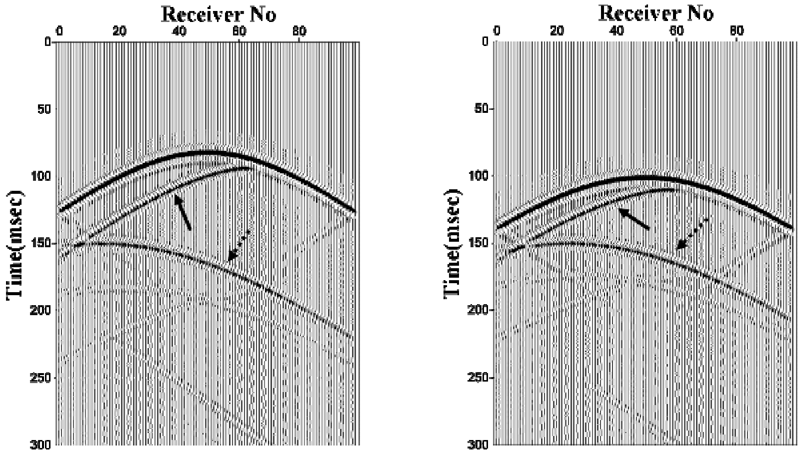

(e) source depth 400m (f) source depth 500m

Fig 3-15 Numerical simulation results of two dipping reflectors

IP transform

The IP transform results for six sources are illustrated in Fig 3-16.The bold circles are the parts of IP of the reflection from Reflector 1 and the dot circles are those from Reflector 2. Compared with the IP transform results of one dipping reflector (Fig 3-13), it's clear that the dot circle parts are the IP of Reflector 2.

As explained in one dipping reflector model, the IP of reflections go closer to the surface as the sources move deeper, because the distances between the reflectors and source are closer. Because this reason, the ρ -distance from the origin to the point- of IP of reflections are smaller as the sources move deeper in both Reflector 1 and 2.

The dipping direction is determined in IP domain by the relation of the ξ - the IP position in receiver axis. That is, the positions of ξ of Reflector 1are on the positive, whereas the ξs of Reflector 2 are on the negative side and the positions of ξ of both reflectors move toward 0 as the depth of sources go deeper. By this thing, It's can be derived that the dip of Reflector 1 is inclined form positive side to 0, that is right to left, and the dip of Reflector 2 is opposite.

Basically, the dip of a reflector can be defined with one source and its' IP. If the IP transform of source depth 50m (Fig 3-16) are only available, the dip angle of a reflector is calculated by the thing that the line of IP and a source is perpendicular to a reflector. The reflectors are not simple plane in much more and real cases, that is, the dip of reflector change just one reflectors, so it may cause misunderstanding in defining the dip of a reflector with only one source and its' IP. So, the relations of other source points and IPs of them are necessary.

The dip filter which limit or reject some range of angles on IP domain can be considered with this fact. The data with variable dip angles are difficult to deal with, so it is easy to deal with the separated data with the angle in some cases. If it is possible to limit the angle range with the help of other information by the logging data and geological survey, dipping filter are useful tool to deal with those data.

Mapping

To investigate the ability of the mapping method using the mid point of sources and IPs, the transformed data shown in Fig 3-16 are used. Imaging process consists of two steps. First, it is transform of the original data to IP domain and some filters like mute and dip filter to remove the direct and some numerical noises, are applied in IP domain. Secondly, after calculating the mid point of a source and IPs, then mapping the value of IPs on mid point.

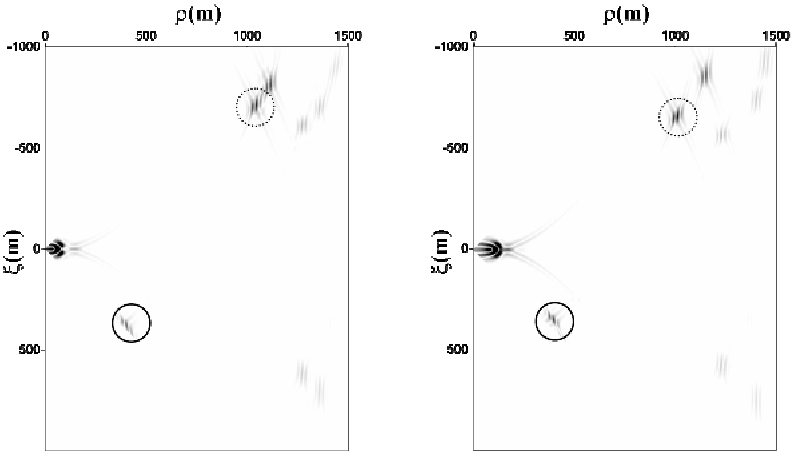

(a) source depth 50m (b) source depth 100m

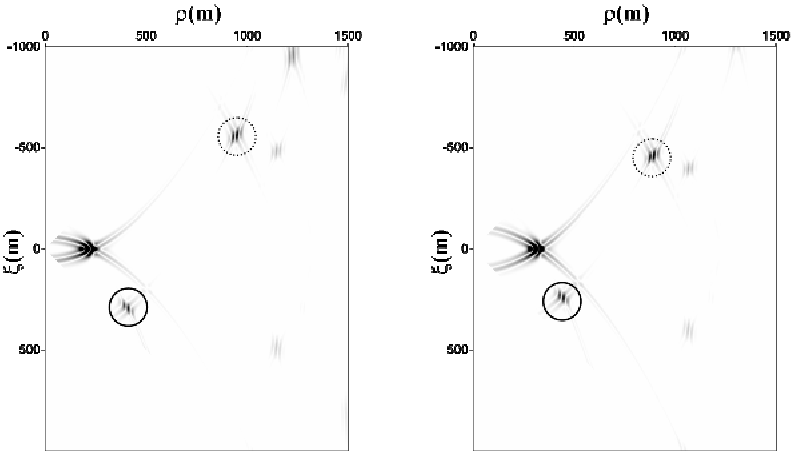

(c) source depth 200m (d) source depth 300m

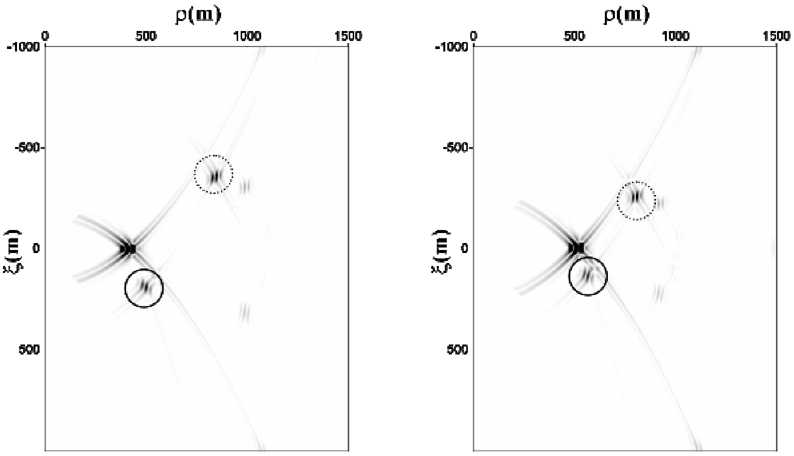

(e) source depth 400m (f) source depth 500m

Fig 3-16 IP transform results of two dipping reflector model

Fig 3-17 shows the results of mapping for 2D two dipping reflectors model presented in Fig 3-14. Fig 3-17(a) is the result with one source of 200m depth and Fig 3-14(b) is the result with all six sources. As it can be seen from the results, it is hard to define the dip angle of a reflector with one source result (Fig 3-17(a)), but if many other sources' data are available, it is possible to map and define the reflector (Fig 3-17(b)).

As explained in the Chapter 2, the concept of mid point mapping of the IP and the source is not to image directly the reflection points of a reflector. So, only one source image as illustrated in Fig 3-17 is concentrated in some parts, while the conventional VSP imaging like VSP-CDP transform and migration gives the image of a reflector in case of one sources. But, as illustrated in Fig 3-17 (b), the mid point mapping results also give agreeable result with the model.

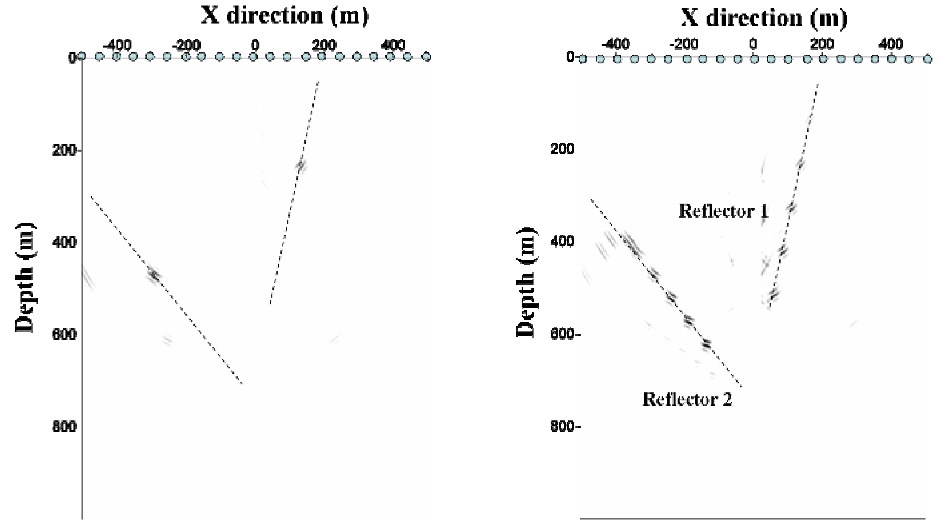

(a) mapping with one source(200m) (b) mapping with six sources

Fig 3-17 Mapping results of 2D one reflector model

3.1.4. 2D VSP model with six reflectors

Let's consider VSP model illustrated in Fig3-18. In previous section3.1.2 and 3.1.3, the characteristics of IP transform using reverse VSP (RVSP) geometry were studied. The geometry of VSP is that the sources are on the surface while the receivers are in the ground and RVSP is just opposite in the source-receiver geometry. So, the characteristics of IP transform in RVSP can be applied to VSP case by the source-receiver reciprocity (Aki and Richards, 1980; Mittet and Hokstad, 1995).

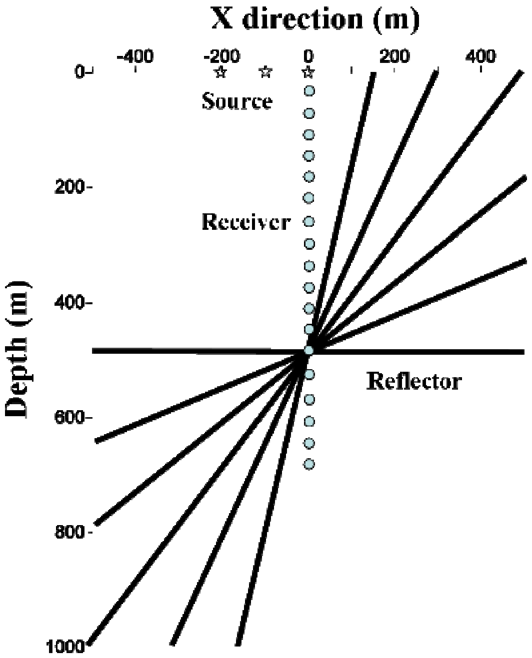

Fig 3-18 2D VSP model with six reflectors

Six dip reflectors of 0^0, 15^0, 30^0, 45^0, 60^0 and 75^0 are all reflectors intercept on the points (0, 500). Three sources are set on the surface which are offset 0, 100, 200m from the origin (0, 0) and the seventy receivers are set on the ground from 10m to 700m in 10m interval. Other simulation parameters are same to those of above section, except the velocity of P wave is 5000m/s.

The simulation results and those IP transform results for three sources are illustrated in Fig 3-19. The red arrow in simulation results and red circles in IP transform results represent the reflection from the 75^0 dip angle reflector and blue, green, light-blue and yellow colors are the reflections of 60^0, 45^0, 30^0 and 0^0 dips respectively. The parts illustrated with black color are the multiple reflections arise from the surface boundary not the numerical boundary.

The reflection from the reflector of 0^0 dip angle is not seen in both simulation and IP transform results, because its' reflection wave is too close to be distinguished from the reflection wave of the horizontal reflector. Generally, the resolution of the reflection seismic is concerned with the frequency of sources and propagation features in the ground and they are also related with many factors like velocity, density, attenuation factor, dispersion of wave and so on. By according to Yilmaz(1987), the vertical resolution is a quarter of a wave length and horizontal resolution is related with the Fresnel zone(Hilterman, 1982; Sheriff, 1984).

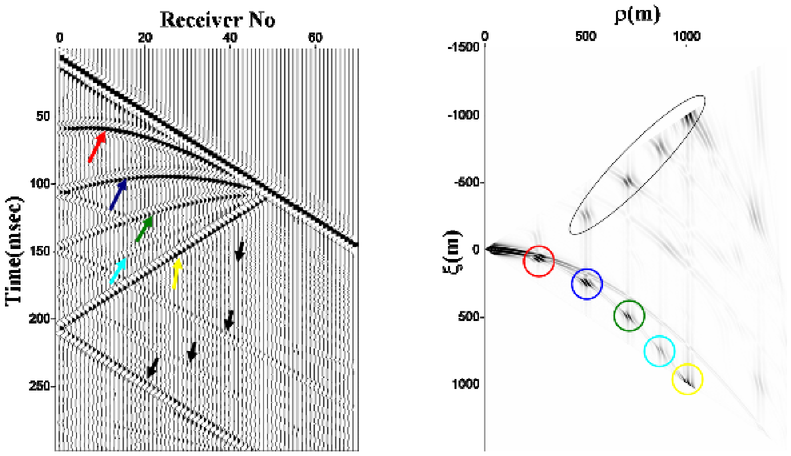

(a) offset 0m (b) IP transform of (a)

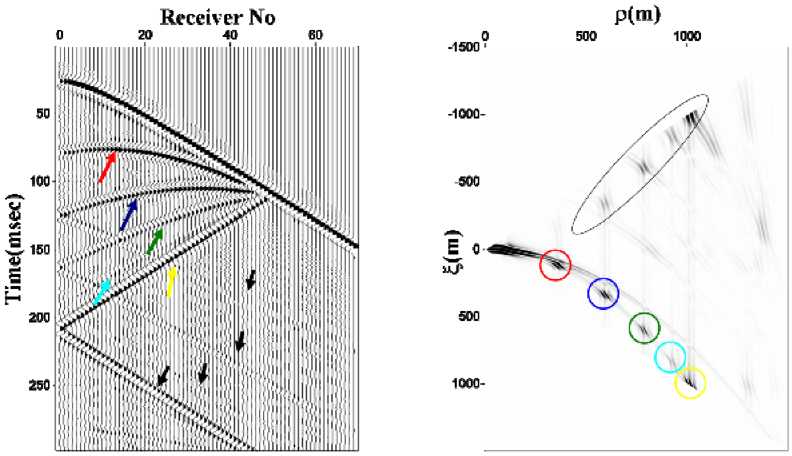

(c) offset 100m (d) IP transform of (c)

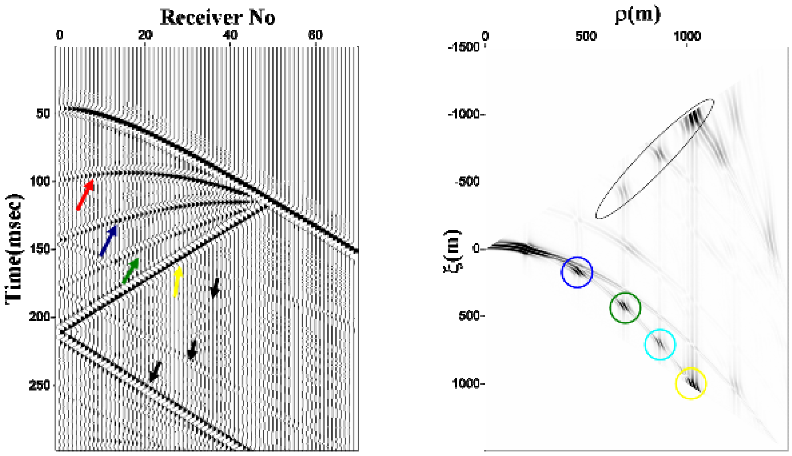

(e) offset 200m (f) IP transform of (d)

Fig 3-19 Numerical simulation and IP transform results

The travel time of direct wave is analytically calculated by dividing the distance from source to the receivers by velocity and resulted to linear line for zero offset case (Fig 3-20(a)). The travel time of reflection waves of variable dips are also calculated as in a same way by dividing the distance from the IPs of reflections to the receivers by velocity and theirs results are shown in Fig 3-20. The colors shown in Fig 3-20 represent same with those of the Fig 3-20, except the black lines are direct waves and gray dashed lines are the reflections of 15^0 dip reflector in Fig 3-20. The positions of IP of every six reflectors are analytically calculated and summarized in Table 3-2.

Table 3-2 Model parameters

IP of offset 0m(ρ,ξ)		IP of Offset 200m(ρ,ξ)	
Dip angle 0^0	(1000,1000)	Dip angle 0^0	(1020,1000)
Dip angle 15^0	(966,933)	Dip angle 15^0	(1035,1033)
Dip angle 30^0	(866,750)	Dip angle 30^0	(981,923)
Dip angle 45^0	(707,500)	Dip angle 45^0	(860,700)
Dip angle 60^0	(500,250)	Dip angle 60^0	(681,423)
Dip angle 75^0	(259,67)	Dip angle 75^0	(455,167)

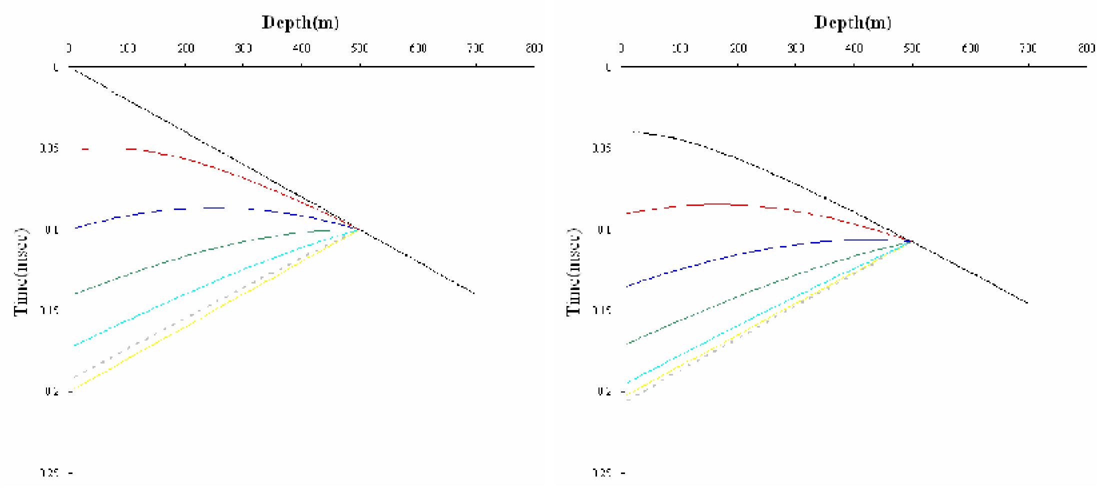

(a) Offset 0m (b) Offset 200m

Fig 3-20 Analytic travel time curve

The travel time of 15^0 dip reflector reflection of zero offset is distinguishable with other waves, especially with horizontal reflection wave even though they are close to each other. The same fact can be addressed for 30^0 dip reflector reflection of 200m offset, but they are hardly separated in IP domain and simulation data as shown in Fig 3-19.

According to the horizontal resolution of first Fresnel zone (Sheriff, 1984; Yilmaz, 1987), the threshold is approximately calculated by

$$r \approx (z\lambda/2)^{1/2} = (v/2)(t/f)^{1/2} \tag{11}$$

Here, r is the threshold of the horizontal resolution, z is the depth of the reflector, λ is wavelength, v is velocity, t is travel time of the reflection and the f is frequency of a wave. The threshold in this case is about 79m, if the travel time of reflection is 0.1 msec. Comparing this threshold with the positions of IP for all six reflectors listed in Table 3-2, they give acceptable results. That is the position of IP of 15^0 reflector of zero offset and that of 30^0 reflector of 200m offset is close to near reflectors within the threshold of the horizontal resolution, so it is hard to be distinguished from others.

3.2. 3-D two faults model

3.2.1. Synthetic data

In above section 3.1, the applicability and characteristics of IP transform and its' imaging are studied for several two-dimensional models, horizontal one layer, one dipping reflector, two dipping reflector and six reflector in VSP. In this section, I expand the study to the three dimension model to know much general case. The model is made to consider the two highly dipping faults model in RVSP. I set that there are two steep dipping faults in the homogenous medium, and the receiver arrays are six co-centered radial lines positioned on the surface (Fig 3-21). Two faults have 50^0 and 75^0 dip angle singed as Fault A and Fault B respectively. The strikes of two faults are perpendicular and two faults intercept on the surface at (200m, 320m). The 81 receivers of each line are set on the surface in every 10m. The receiver Line1 is parallel to the x direction and to the Fault A while Line4 is parallel to the y direction and to the Fault B. The angles between the neighbor lines are 30^0 and the angles between Line1 and other lines, that is rotation angle form x direction, are 30, 60, 90, 120 and 150^0 respectively.

In order to generate the synthetic RVSP data set, the staggered grid finite deference method with forth order finite difference scheme for space is adopted and this scheme is widely used as an accurate computation scheme (Levander, 1988). The information of numerical modeling parameters is summarized in Table 3-3.

Acoustic wave modeling is done for simplicity of discussion and density change is added on the faults. One source is set on the 216m depth and its' wavelet has Ricker wavelet with 100 Hz main frequency. Grid sized is determined on the basis of both prevention of numerical dispersion and required calculation time.

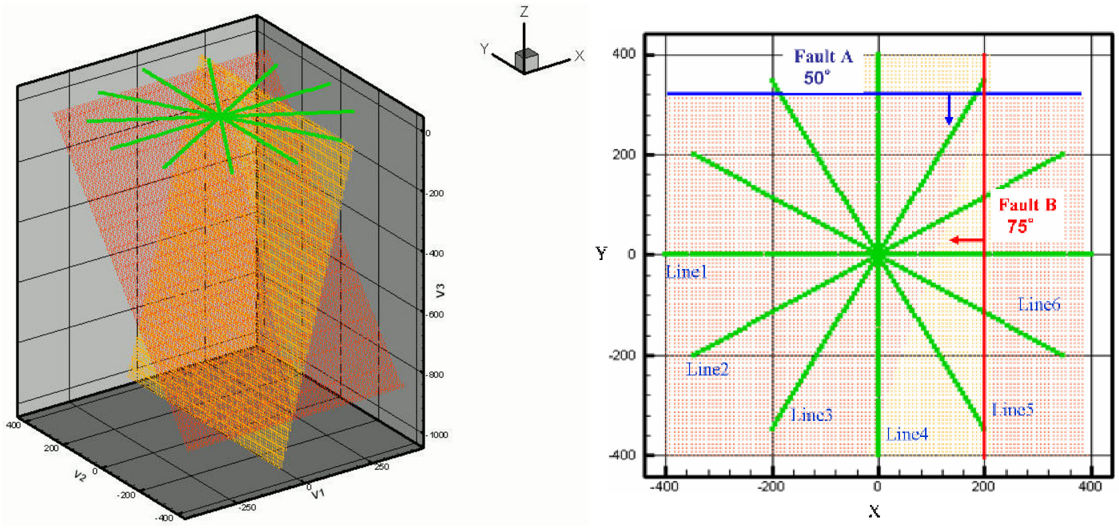

(a) 3D view (b) Plane view

Fig 3-21 3-D two faults model

Table 3-3 Model parameters of 3-D two faults model.

Model Size	800m*800m*1000m	Grid	2m*2m*2m
P wave velocity	5300m/sec	Calculation Time	300msec
Time sampling	0.15msec	Density of two reflectors	1.8g/cm^3
Density of background	2.5g/cm^3	Source wavelet	Peak:100Hz Ricker wavelet
Strike of Fault A	X direction	Dip of Fault A	50°
Strike of Fault B	Y direction	Dip of Fault B	75°
Width of reflectors	10m(5 Grids)	Depth of a source	216m
Receiver Line	6 Lines	Receiver interval	10m

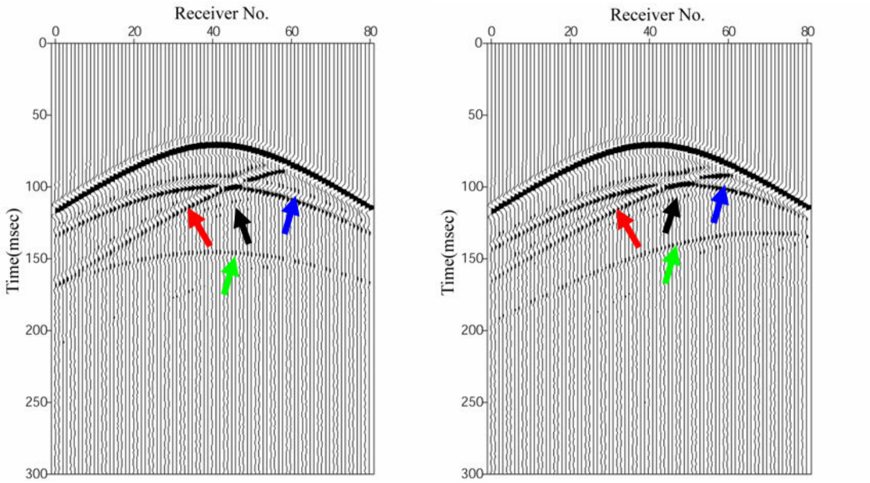

(a) Line 1 (b) Line 2

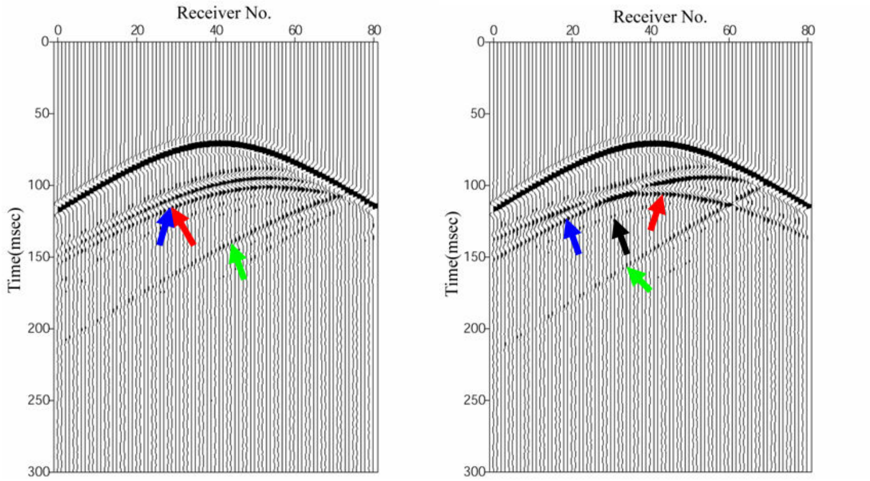

(c) Line 3 (d) Line 4

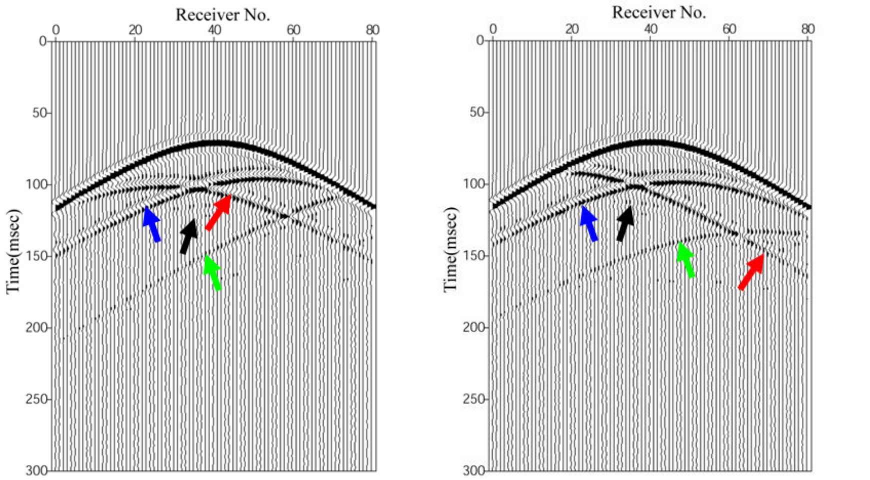

(e) Line 5 (f) Line 6

Fig 3-22 Numerical simulation results of 3-D two faults model

Simulation results are shown in Fig 3-22 and the blue arrows point the reflections from Fault A whereas the red ones point the reflections from Fault B. The black arrows in the figures are multi-reflection between two faults and green one are diffraction wave arise from the top the Fault B. The receiver numbers are assigned from the lower part of the receiver lines. In the result on Line 1 (Fig 3-22(a)), the reflection wave from Fault A shows the hyperbola because Fault A is parallel to receiver line, while the reflection from the Fault B show the inclined wave from right-top to left-down because Fault B is transverse and cross at the point 600m with Line 1. The opposite case is said For Line 4 because Fault A is transverse and Fault B is parallel to the receiver line Lin4. Expect for the result of Line3, the reflections from Fault A and Fault B, are easily distinguished in synthetic seismograms. However, in the case of Line 3, the reflections from the two faults are overlapped, and it is making them hard to be distinguished.

3.2.2. IP transform for 3-D fault model

IP transform using the synthetic data is illustrated in Fig 3-23 and the horizontal axis corresponds to ρ -the distance between the source and IP- and the vertical axis corresponds to ζ (the projection point on the receiver line of IP). In the Fig 3-23, the blue circles correspond to IP for Fault A and the red circles for Fault B. The IPs seen around 210m in ρ axis are due to direct waves. As it is investigated in 2-D model, the IPs of the reflection waves are accumulated on some. The IPs of two faults are separated and distinguishable on IP results except for the IP transform results for Line 3.

In the IP transform of Fault A for Line 1, the ξ is 0m because the Fault A is parallel to Line1. If the data of Line 1 is only available, it is impossible to know whether Fault A is inclined or horizontal plane. That is, the Fault A has the dip and the strike actually, but the IP results have the same feature of horizontal plane when the receiver line like Line 1 is parallel to the strike of the fault. The same statements are said for Fault B case with the IP transform result of Line 4.

If the IP transform results are more investigated, an interesting and important fact can be found; For example, let's concentrate on the position of IP of Fault A in Fig 3-23, the ξ of IP of Fault A reflection for each line varies according to the receiver lines but the ρ of IP of Fault A does not change in all receiver lines. The same facts can be perceived for the Fault B case. The reason why the ξ of IP of the reflection varies with the receiver lines and the ρ does not, is the IP of one reflector for one source is determined geometrically. The invariance of the ρ of IP of a reflector is easily seen by the definition of ρ of IP transform, that is, ρ is the distance between the origin to the IP.

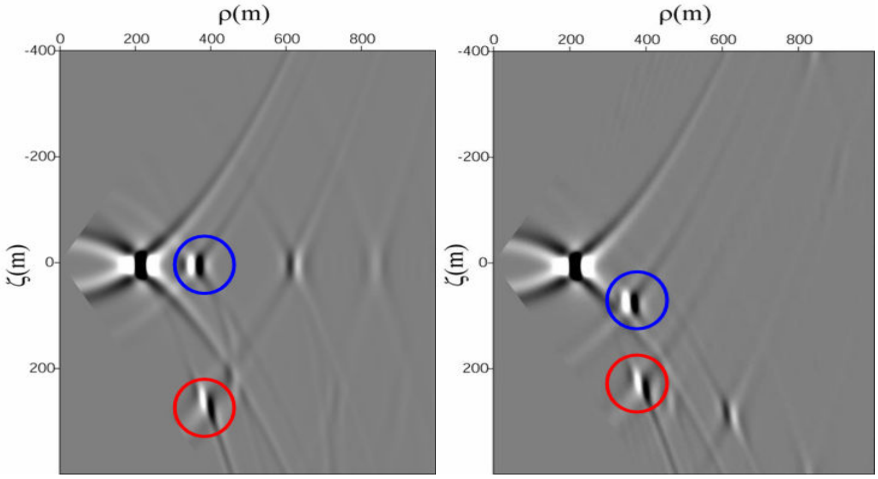

(a) Line 1 (b) Line 2

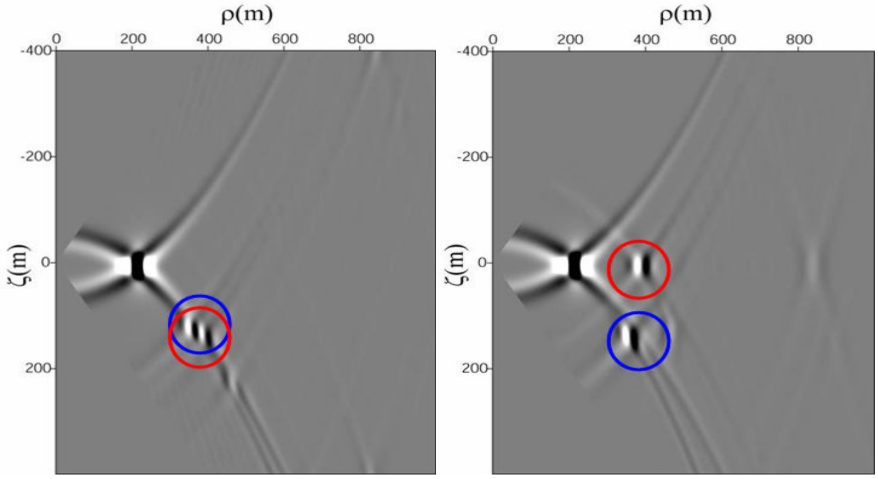

(c) Line 3 (d) Line 4

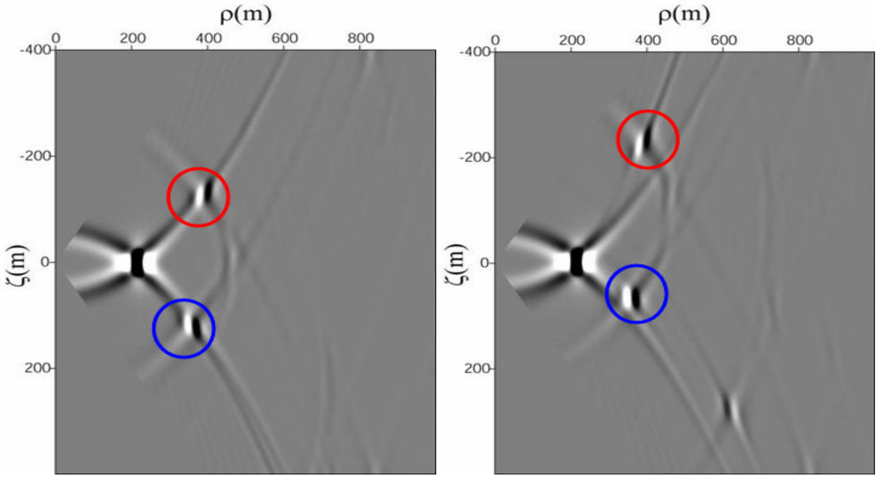

(e) Line 5 (f) Line 6

Fig 3-23 IP transform results for synthetic data shown in Fig 3-22

3.2.3. Generalized IP transform and inverse IP transform

Generalized IP transform

As mentioned in the previous section 3.2.2, the ρ of IP of one source and one reflector does not vary according the receiver lines but the ξ varies. I consider the plane view on the x-y plane (the surface) to survey this property shown in Fig 3-24. If Fault B is only considered, The IP of Fault B underlay in depth of Line 1 because Line 1 is vertical to the strike of Fault B. Assuming that the vertical projection of IP of Fault B to Line 1 is set ξ_1 and the distance from the origin to the IP is set ρ, then the point coincides with the projection point of IP to the surface. In a same way, ξ_2, ξ_3, ξ_4, ξ_5, and ξ_6 are uniquely determined as illustrated in Fig 3-24. If we consider the line connecting the two points which are the ξ1 and another one, the line is transverse to the receiver line of another projection point.

Let's change the view points, if we don't know the strike of a reflector but we know IP transform results of some receiver lines, it is possible to make the projection map of IP on surface of receiver lines and to determine the common point by searching the point of each line which is transverse to the each receiver line and the IP. The common point is same to the vertical projection of IP of a reflector on the surface.

Ideally, this process is done with at least two lines except those are perpendicular to each other. As seen in Fig 3-24, the vertical projection of IP from ξ_1 of Line 1 to Line 4 is uniquely determined as ξ_4 but the projection of IP from Line4 to Line 1 is not determined uniquely because those two lines are vertical to each others.

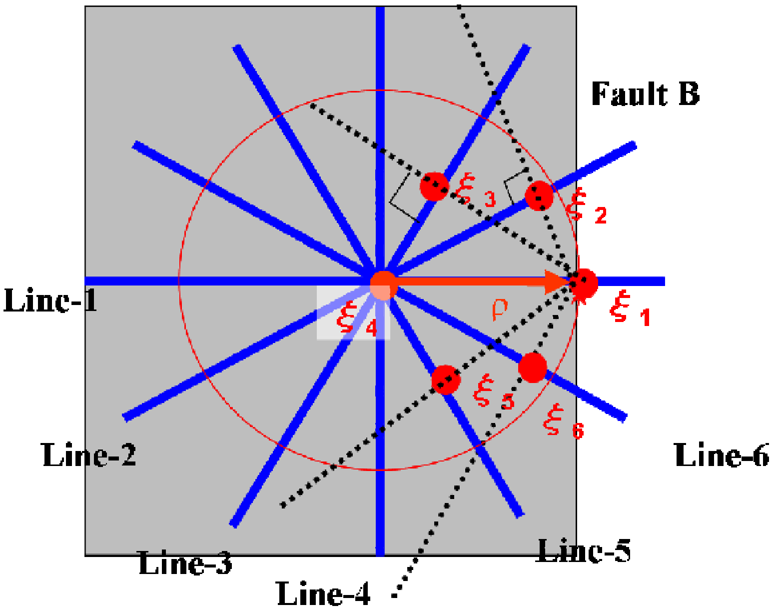

Fig 3-24 Schematic diagram of IP changes of Fault B according to the lines

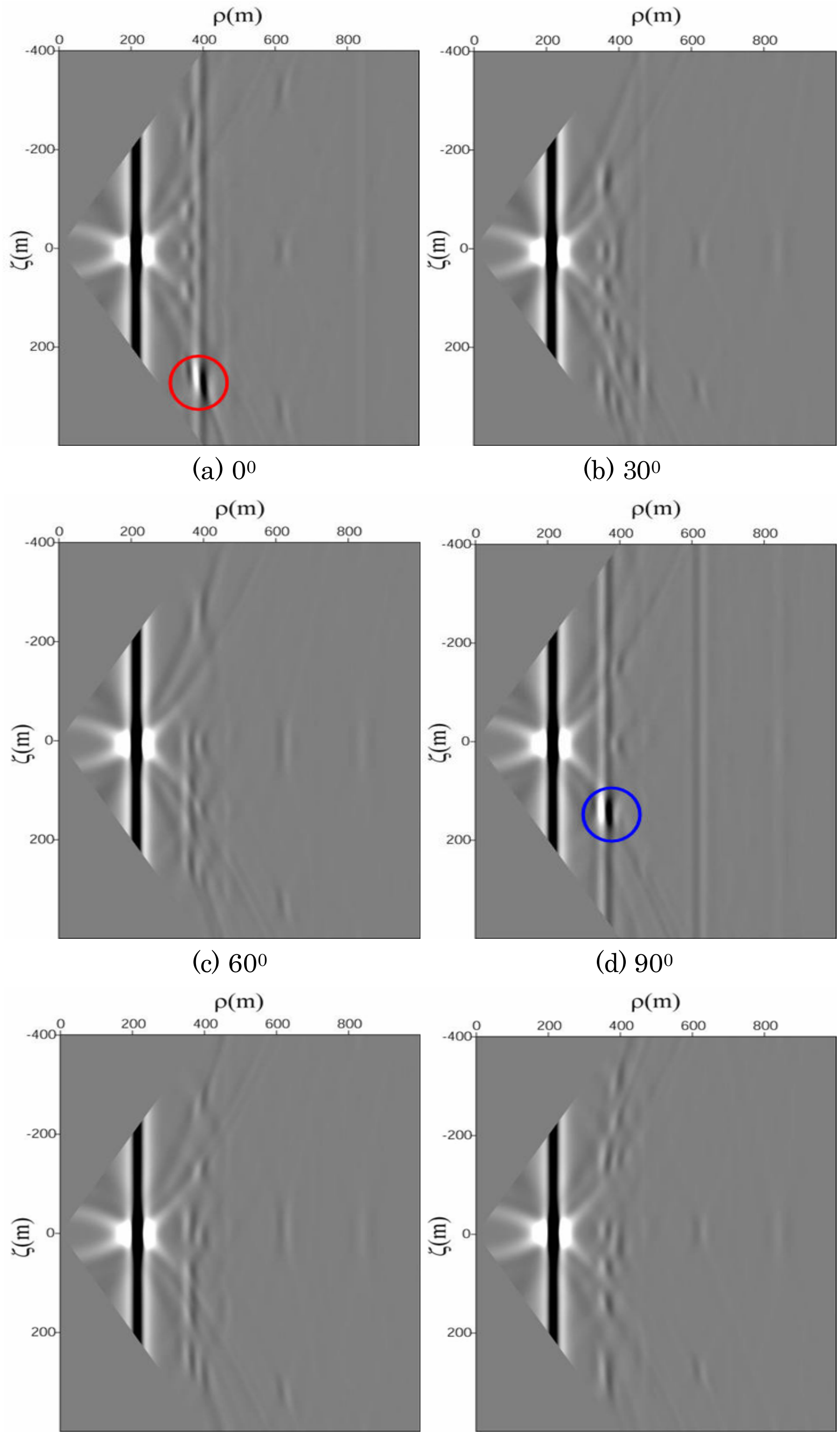

(a) 0^{0} (b) 30^{0}

(c) 60^{0} (d) 90^{0}

(e) 120^{0} (f) 150^{0}

Fig 3-25 Generalized IP transform results for synthetic data of all lines.

With this property, the new transform is considered name Generalized IP transform, that is, to convert the IP data of one line to that of another line. The examples of the generalized IP transform results are illustrated in Fig 3-25. The angles represent the transformed angle from the x direction, that is, Line 1 direction. As seen the results, the IP of Fault A is enhanced only in the result of angle 90^0(Fig 3-25(d)), which is vertical to the Fault A and the IP of Fault B is concentrated on angle 0^0(Fig 3-25(a)). Some noises along the ρ axis are seen in the Fig 3-25 (a) and (d) because all six lines data is used to the generalized IP transform which include the vertical line to the transformed axis. The results excluding the vertical line to the transformed axis, that is , the data of Line 1 incase of 90^0 transform and the data of Line 4 incase of 0^0, are shown in Fig 3-26. Compared with the results of Fig 3-25(a) and (d), the results of IP are clearly distinguishable in Fig 3-26.

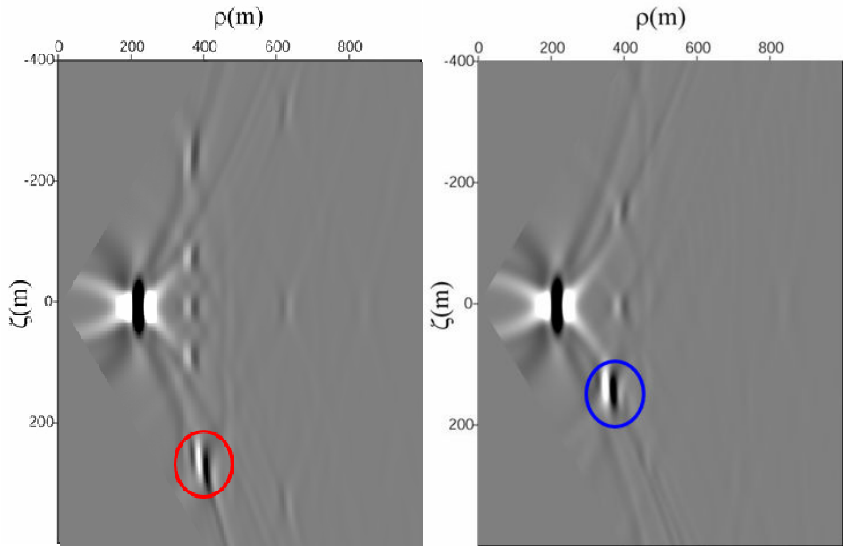

(a) 0^0 (b) 90^0

Fig 3-26 Generalized IP transform results for synthetic data excluding the data transverse to the transformed axis.

Generalized inverse IP transform

Using these two generalized IP data (Fig 3-26), the waves of the reflection are reconstructed by inverse transform and illustrated in Fig 3-27. The reconstruction of waves consists with inverse transform of each generalized IP data (Fig 3-27 (a) and (b)) separately and combination of them (Fig 3-27(c)). The generalized inverse transform results of all six receiver lines are shown in Fig 3-28. Compared with the synthetic data shown in Fig 3-22, the reflection wave of Fault A and Fault B are reconstructed although some noise around the intercept part with direct wave are seen. The pre-processing of mute to eliminate the IP of direct wave which are strong signal and other noises are done to get the results in Fig 3-25 and Fig 3-26.

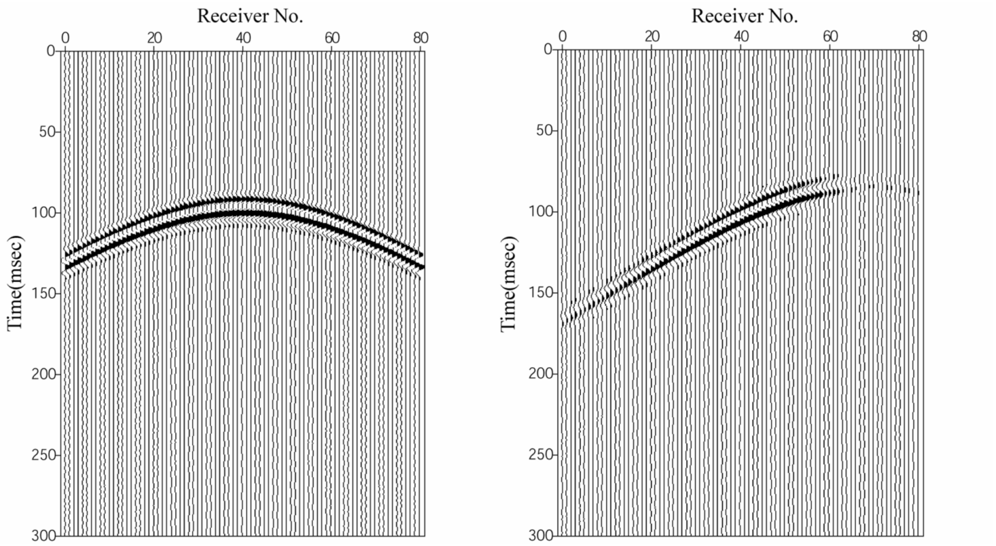

(a) Fault A of Line 1 (b) Fault B of Line1

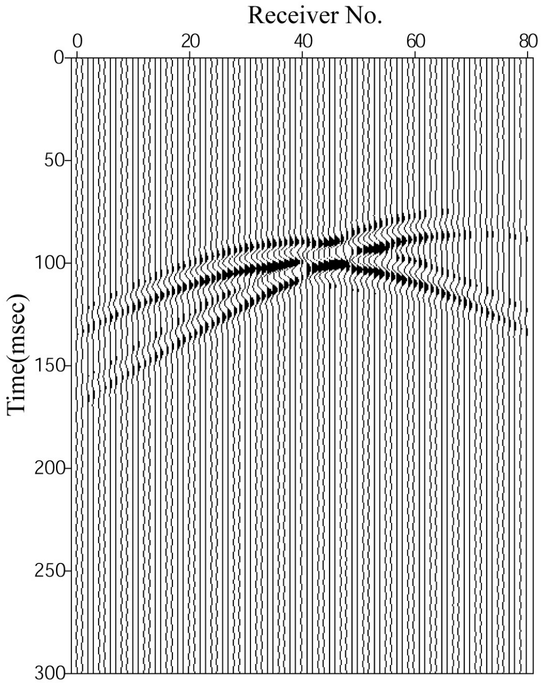

(c) combine (a) and (b)

Fig 3-27 Generalized inverse IP transform results for Line 1

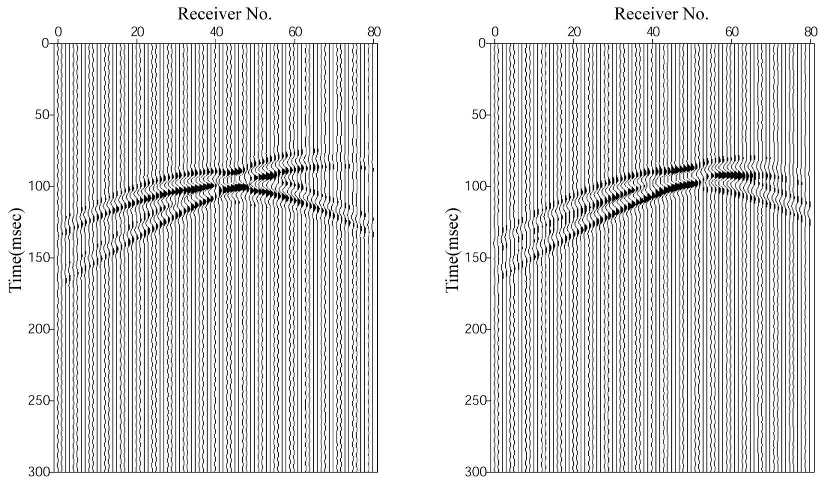

(a) Line 1 (b) Line 2

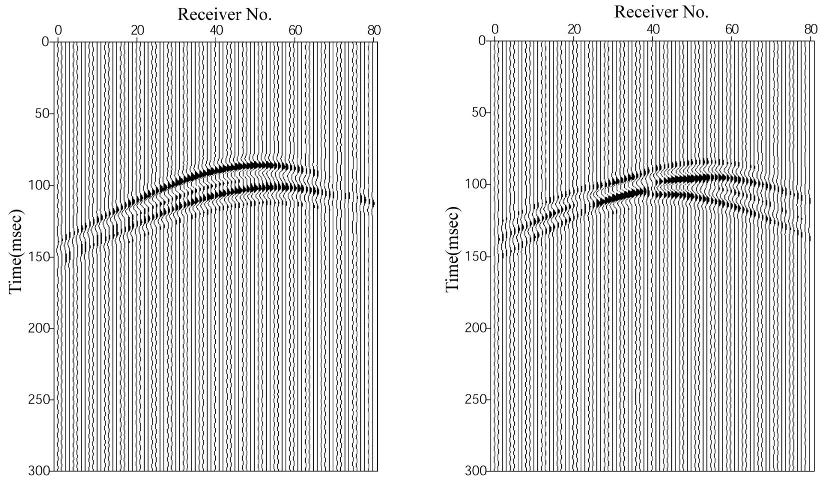

(c) Line 3 (d) Line 4

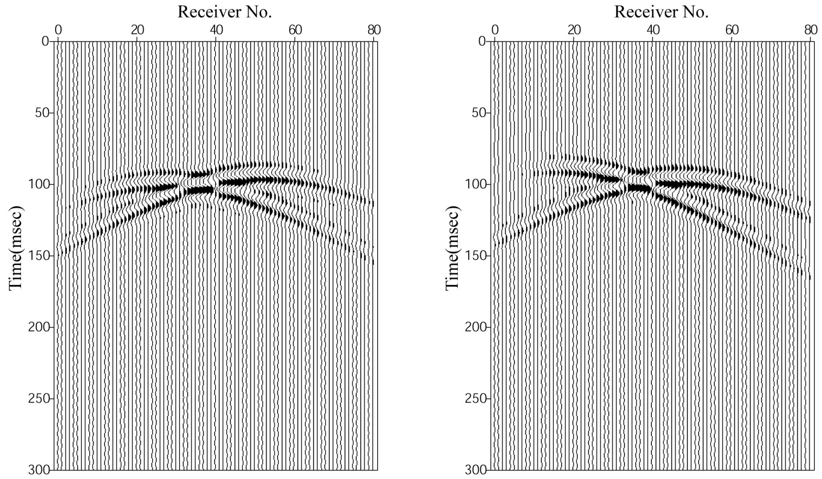

(e) Line 5 (f) Line 6

Fig 3-28 Inverse transform results of each line using data only Fig 3-26 (a) and (b)

3.2.4. Imaging

To get the final image of the faults, the mid-point mapping method in IP domain is applied. The mid-point mapping method uses the fact that a reflector includes the mid-point of IP of a reflector and a source.

Imaging process consists of two steps. First, it is generalized transform of the original data to IP domain and to decide the transverse direction of faults for IP transformed data. Secondly, the operator which calculates the mid-point between the IP data decided at first step and a source is applied.

The results of this imaging process to the IP data (Fig 3-26) are illustrated in Fig 3-29. The two reflector of Fault A and Fault B are well reconstructed. It may be hard to say that this mid-point processing is applied with a more complicated model with only one source but that can be overcome by applying the multi-source which are distributed in space.

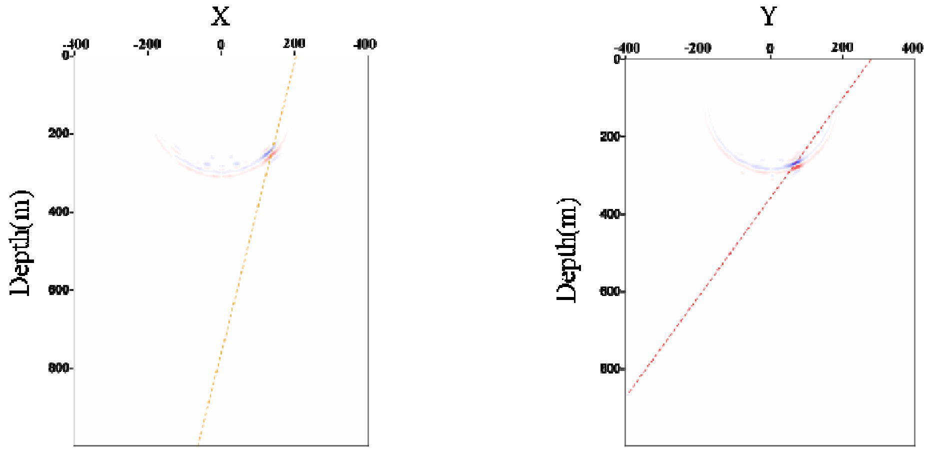

(a)Plane view(X-Z, Fault B) (b)Plane view(Y-Z , Fault A)

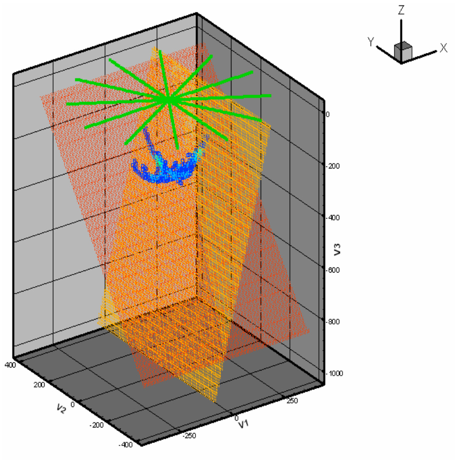

(c) 3D view

Fig 3-29 Mid-point imaging results

Chapter 4

Application to the Field Data

4.1. 3-D Reverse VSP Data

4.1.1. Site explanation of Mizunami

Mizunami is located central Japan in Gifu prefecture. In this city, two shafts and several level drifts are planed to excavate till to the one-thousand meter depth as the Mizunami Underground Laboratory Project (Sato et al, 2003). The laboratory will be used to research the property and the activity of the radio activity material in the deep location. As the first step of the construction, the surveys like basic geological, geo-environmental, geotechnical and geophysical research are done (Matsuoak et al, 2002, McCrank, 2002).

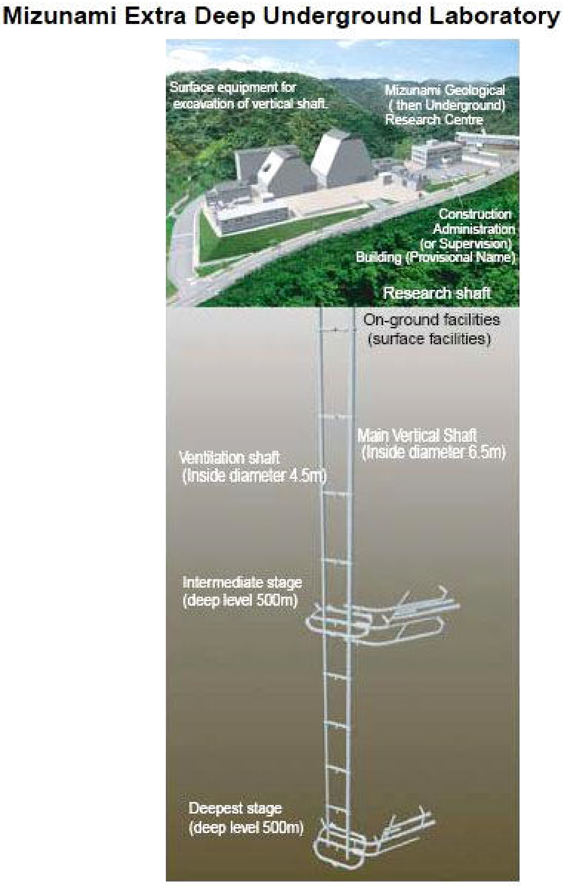

Fig 4-1 Schematic diagram of Mizunami Underground Laboratory project (presented by JAEA)

4.1.2. Data acquisition

One shaft will be used as a main and the other for the ventilation (Fig 4-1). Two shafts will be connected every 100m with horizontal tunnels and excavated about 1000m depth. The explosions of dynamite during the excavation are used as sources. The 144 Receivers are located around the main shaft (Fig 10). The dynamite shots are used as sources during the excavating. We have preformed and processed four shots till now and plan to acquire more data according to the excavation. I summarized the data acquisition in Table 4-1.

Table 4-1 Summary of the RVSP data acquisition

Receiver Line	Channel No.	Shot No.	Depth from the ground level
Line 1	1-22	Shot 1	-81m
Line 2	23-37	Shot 2	-106m
Line 3	38-64	Shot 3	-136m
Line 4	65-124	Shot 4	-152m
Line 5	125-144		
Line 6	145-174		

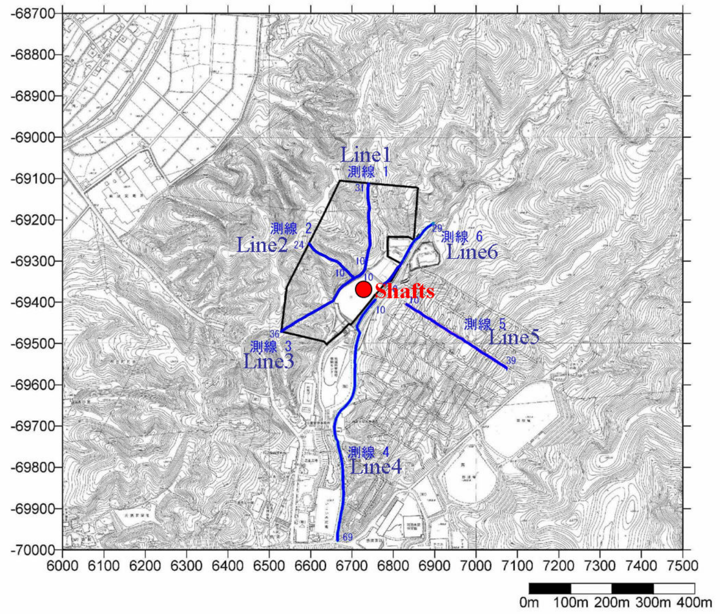

Fig 4-2 Geometry of RVSP survey

Six receiver lines are set around the shafts and as straight as possible as illustrated in Fig 4-2. Line 1 is near toward north direction from the shafts and Line 5 is set in the tunnel and toward south-east direction from the shafts. Original shot records are illustrated in Fig 4-4. Original wavelet is recorded with 40Hz-geophone and the sampling rate is 1msec. The geophone are planted underground by digging 1 or 2m hole (Fig4-3). 20,000 samples are recorded and the GPS time is used to check the exciting source time.

Fig 4-3 Photo of planting the geophones

Shot gather records are presented in Fig4-5 and these are results after pre-processing like band-pass filter, shot-time correction, elevation correction and AGC (Auto gain control).

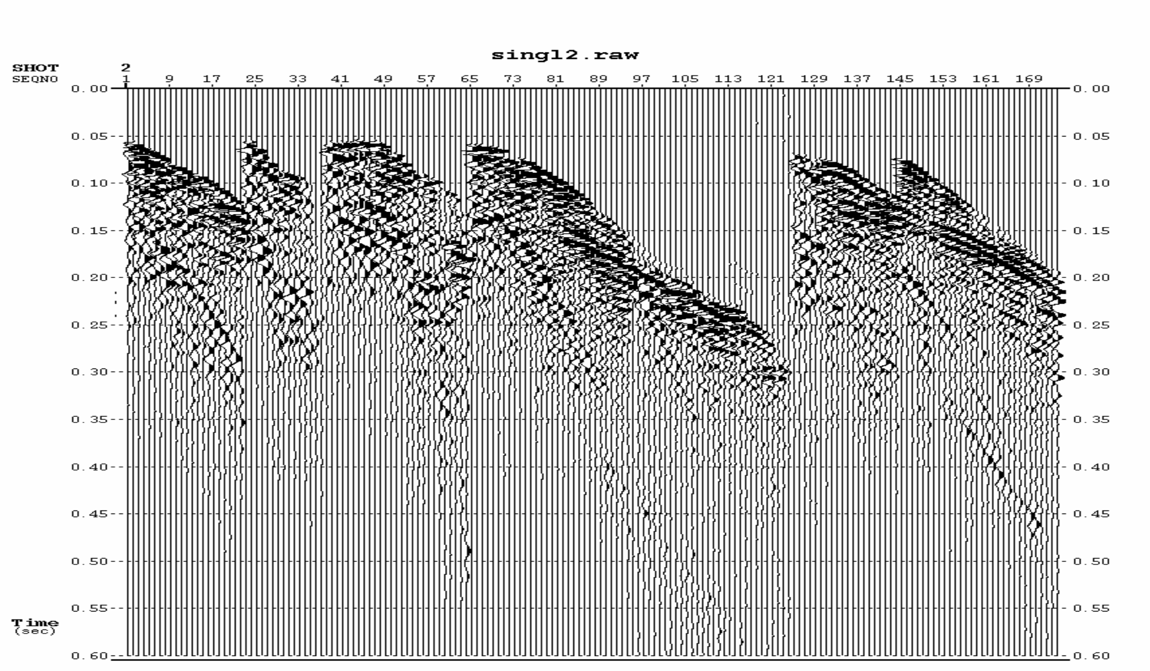

Fig 4-4 Original shot records for Shot 1

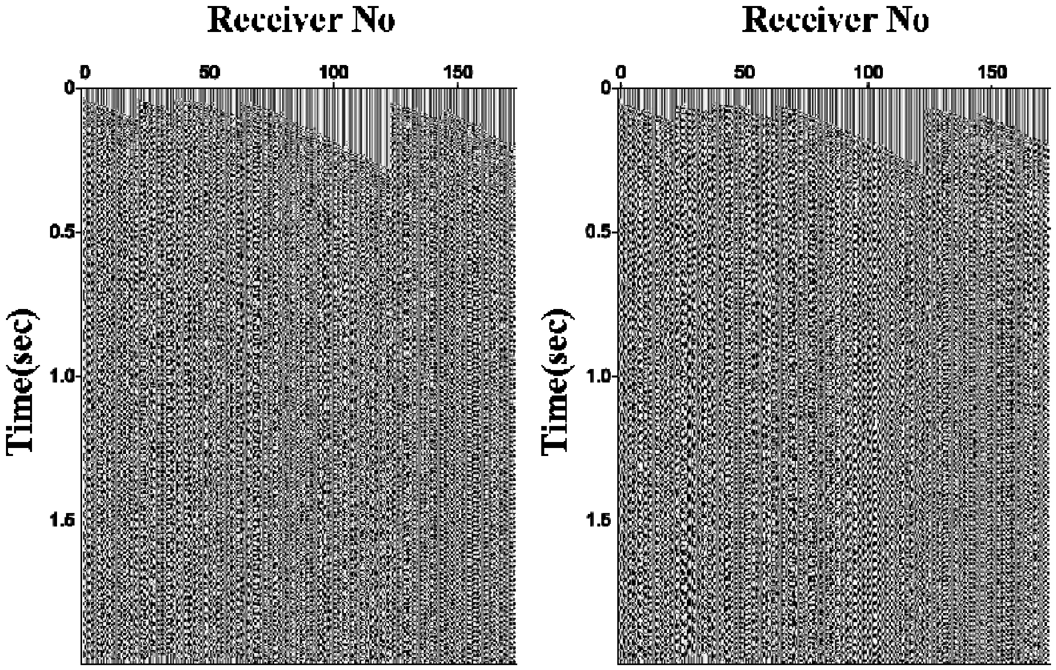

(a) Wavelet for Shot 1 (b) Wavelet for Shot 2

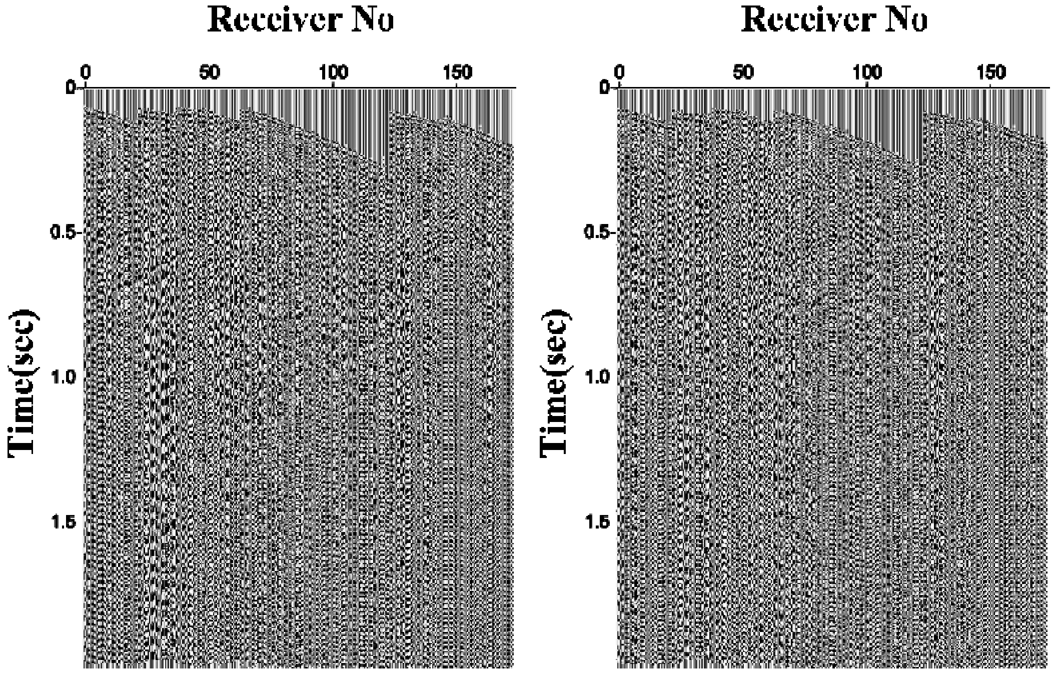

(c) Wavelet for Shot 3 (d) Wavelet for Shot 4

Fig 4-5 Common shot records after preprocessing

4.1.3. Generalized IP transform and inverse transform

In numerical test, I addressed that the image point of one reflector is enhanced to the IP domain whose direction is transverse to the reflector by generalized IP transform. In field survey, I try to set the receiver lines as radial and straightly as possible (Fig 4-2).

Some generalized IP transform results are shown in Fig 4-6, which is transformed result to the angle 8^0 for each shot. The angle of transformed line is defined as the angle from the East direction. Although some parts in which IP are enhanced, are seen, there are some difficulties to distinguish the transverse direction with only the IP transformed data as shown in Fig 4-7 and Fig 4-8. But the previous information from the surface survey data and borehole logging data helped to confine the transform ranges. The location map of faults predicted from the previous survey is shown in Fig 4-9 and the lines in red color are transverse to the strike of the faults. There exist much more faults but only detectable faults are presented by this RVSP survey.

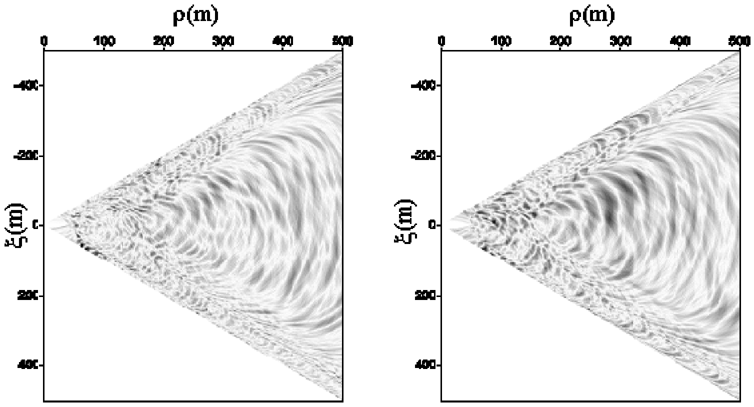

(a) Shot1 (b) Shot2

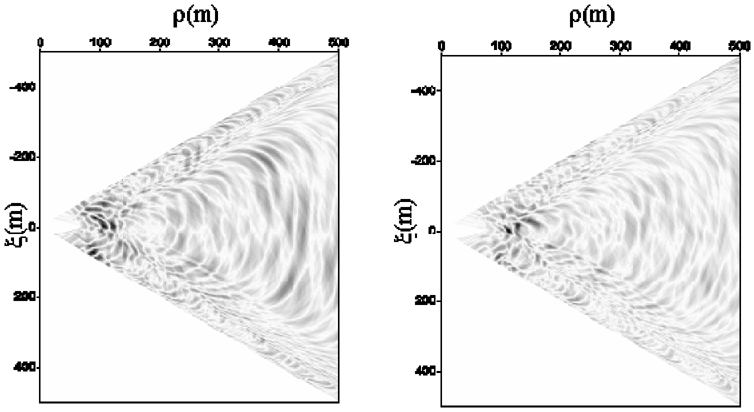

(c) Shot3 (d) Shot4

Fig 4-6 Generalized IP transform results for the angle 8^0 line

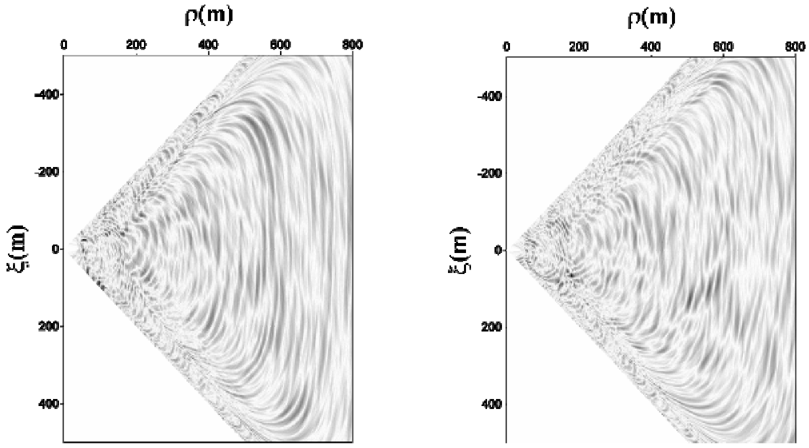

(a) 0^0 (b) 30^0

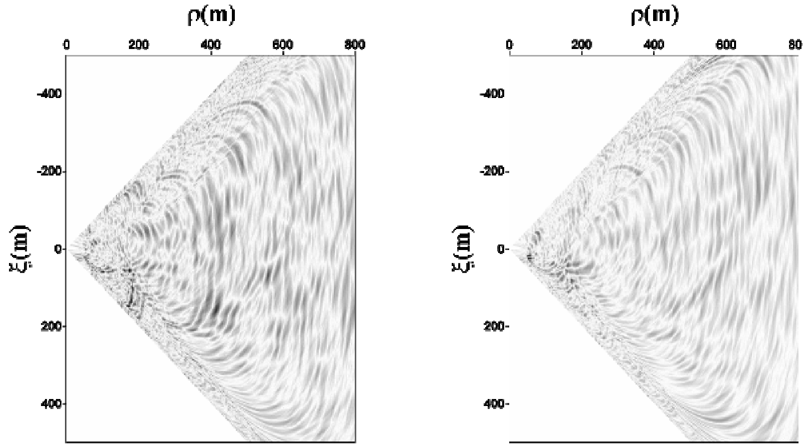

(c) 60^0 (d) 90^0

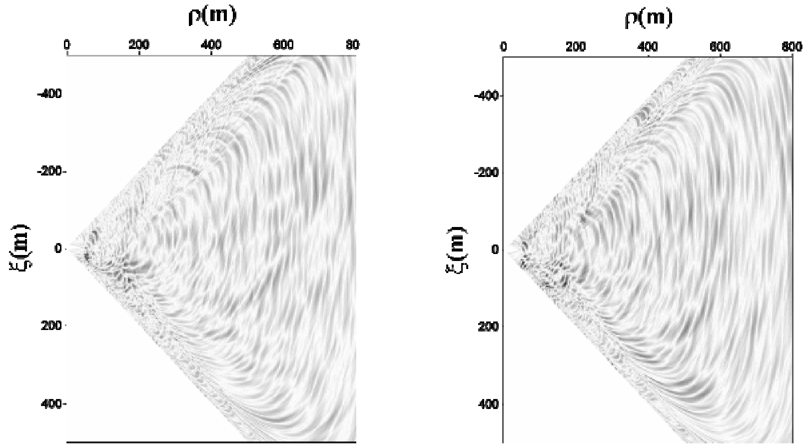

(e) 120^0 (f) 150^0

Fig 4-7 Generalized IP transform results of various angle for Shot 1

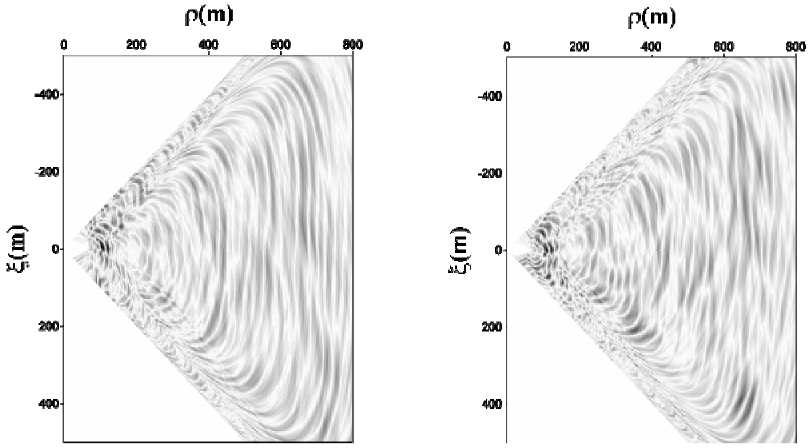

(a) 0^0 (b) 30^0

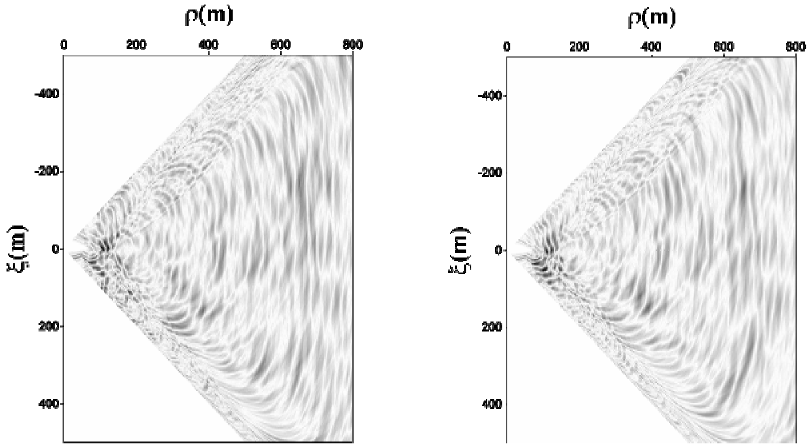

(c) 60^0 (d) 90^0

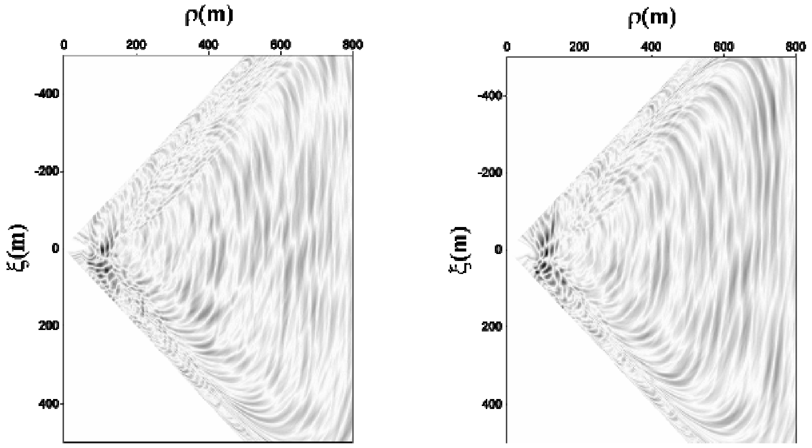

(e) 120^0 (f) 150^0

Fig 4-8 Generalized IP transform results of various angle for Shot 4

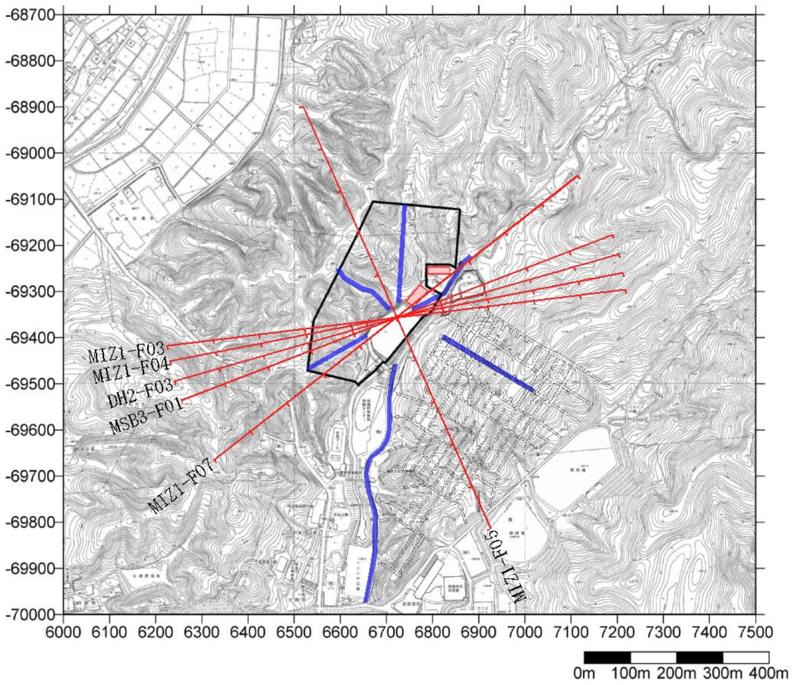

Fig 4-9 Map of transverse lines to the faults and RVSP receiver lines

As it is clear from the map of faults directions, the strikes of faults are tend to north-west direction because transverse lines illustrated by red color in Fig 4-9 are toward to north-east direction.

After applying some filter on the data in IP domain (Fig 4-6) like muting, localization of IP and clip under some value, generalized inverse IP transform is applied and the results are shown in Fig 4-10. Compared with the original records (Fig 4-5), the reconstructed waves are less noisy although some noises under 0.5sec are seen.

The faults known by the surface geology survey and the logging data have high dip angle around survey area. Hence, the reflection events of RVSP appear close to the direct waves. That is why it is difficulty to separate the reflection waves from other in highly dipping reflectors. The direct wave and some noises are somewhat removed in the reconstructed waves (Fig 4-10) but there still remain some and it is also seen that some signal are removed by the filter in IP domain.

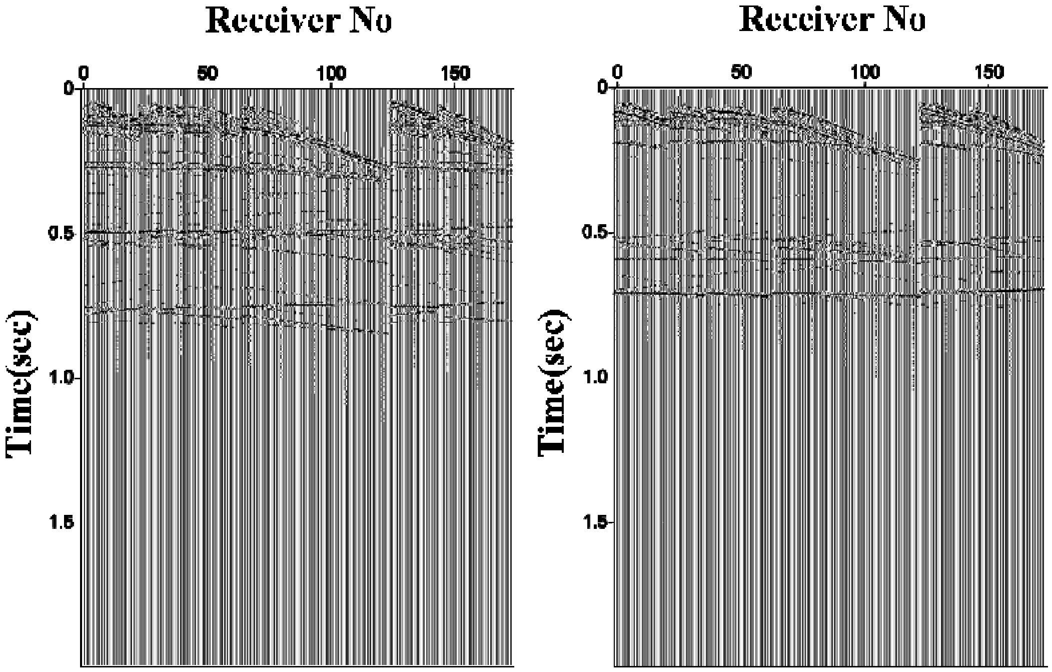

(a) Wavelet for Shot 1

(b) Wavelet for Shot 2

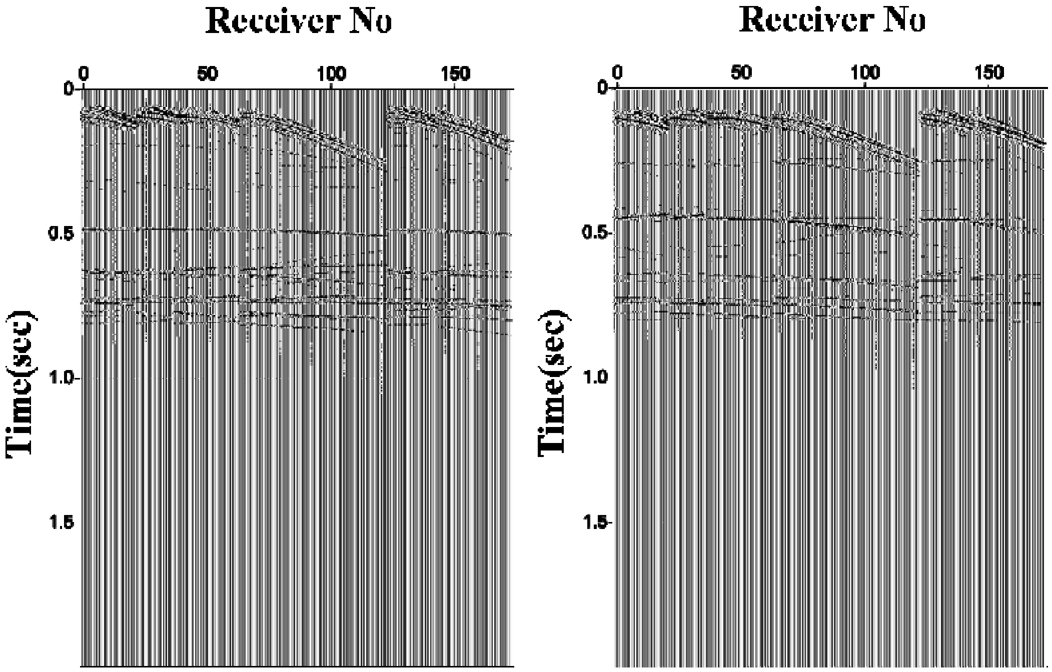

(c) Wavelet for Shot 3

(d) Wavelet for Shot 4

Fig 4-10 Reconstructed shot records by generalized inverse IP transform for the data shown in Fig 4-5

4.1.4. Imaging

Unfortunately, it is hard to confirm the transverse direction of faults by searching only the generalized transform IP results of each line data, which work well in the numerical data. However, I consider two more filters on the field data. One is the blanking under some value of IP and the other is the dip filter. I think the blanking is useful because the IP of reflection is enhanced in IP domain even if it is not clearly distinguishable. Dip filter is the limitation of dip angle of IP when imaging. The dips of faults are very high on this site and the apparent dip angle of IP is calculated easily as a following equation.

$$\theta = \cos^{-1}((\xi_{ip} - \xi_s)/(\rho_{ip} - \rho_s))$$

Where, (ρ_{ip}, ξ_{ip}) is the poison of the reflection and (ρ_s, ξ_s) is the poison of the source on IP domain.

The results of imaging on the transverse of MIZ-F03 fault, 8 degree from the East direction are shown in Fig 4-11. The left figure of Fig4-11 is given after only muting some parts in IP domain and blanking under some value and the right is given after dip filter with the data of Fig 4-11(a). Imaging results for the other faults are illustrated in Fig 4-12 and 3d imaging result are shown in Fig 4-13. The same filters of mute and dip filter are applied to get the results shown in Fig 4-12 and Fig 4-13

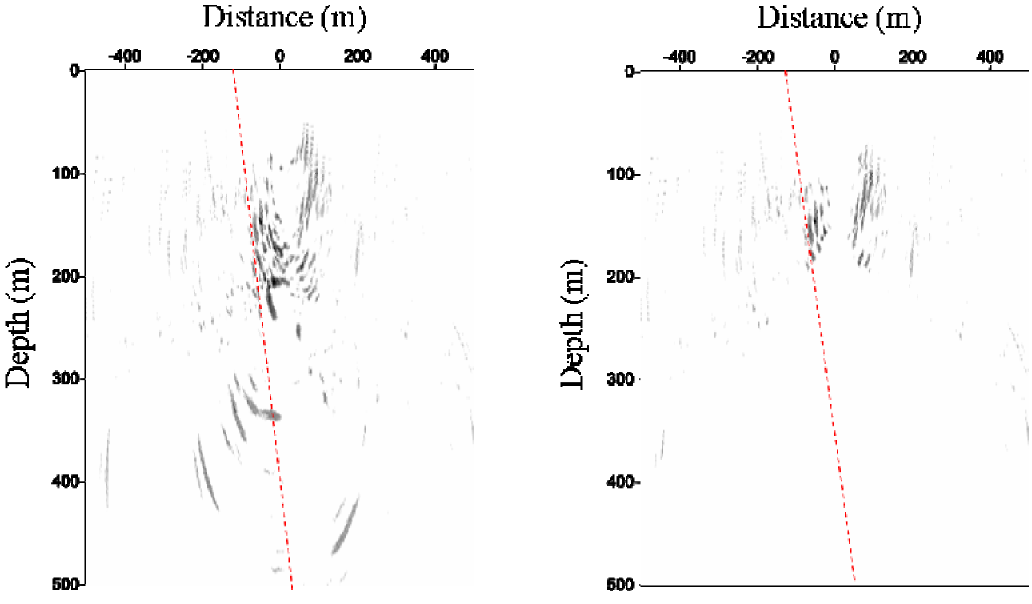

(a) Muting (b) Dip filter

Fig 4-11 2-D imaging results for MIZ-F03 transverse to angle 8 degree

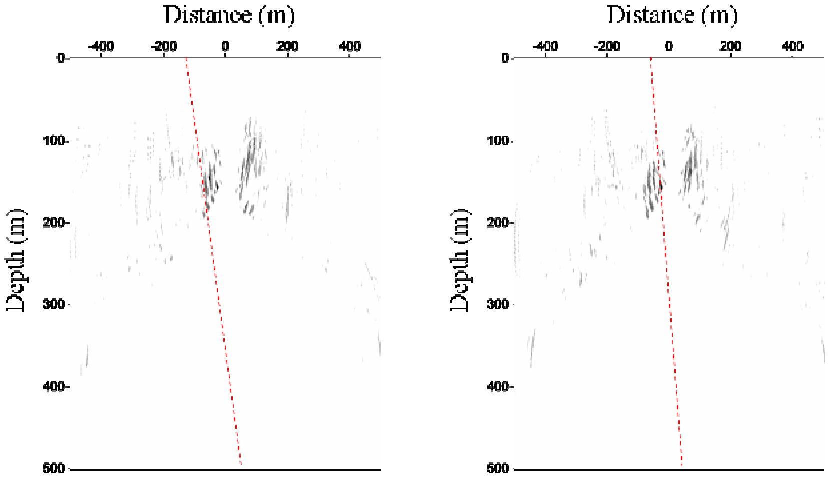

(a)MIZ-F03 (b)MIZ-F04

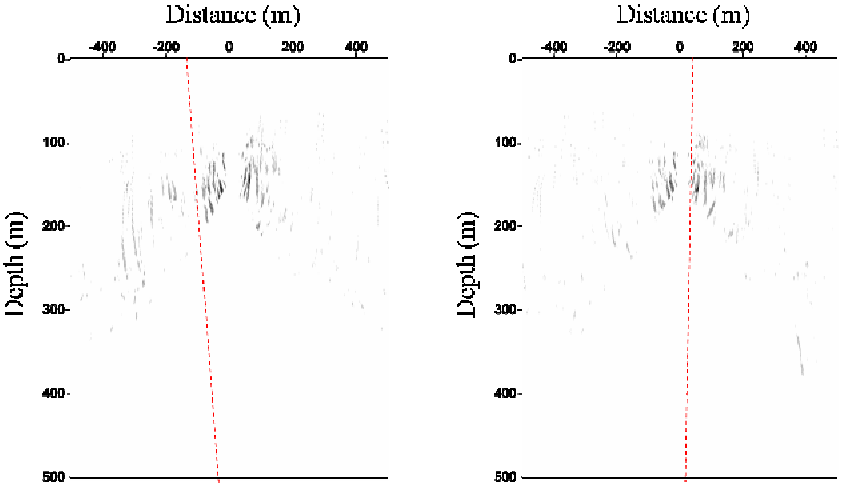

(c)DH2-F03 (d)MSB-F01

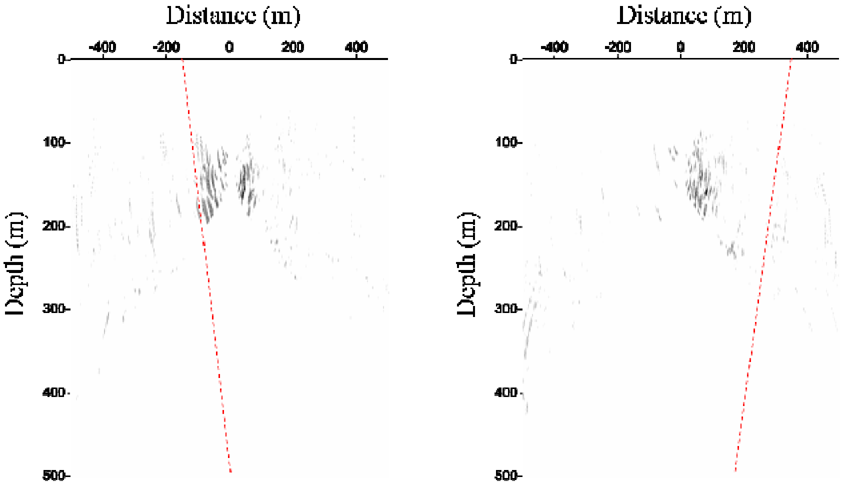

(e)MIZ-F07 (f)MIZ-F05

Fig 4-12 2D imaging result for each fault

The red dash lines of imaging results present faults derived the data of borehole and the surface geological survey. I can get 2D and 3D images which agree with the faults position except for MIZ-F05 fault. The reason can be explained by the fact that MIZ-F05 is located too far from the source, so its' power is too low to be detected. It is expected that I can obtain the data for the deep sources and clear that fact.

As explained, the strikes of faults are inclined to the north-west direction, that is, the transverse direction of the strikes are inclined to the north-east and the result of 3-D mapping of data are accumulated on those parts.

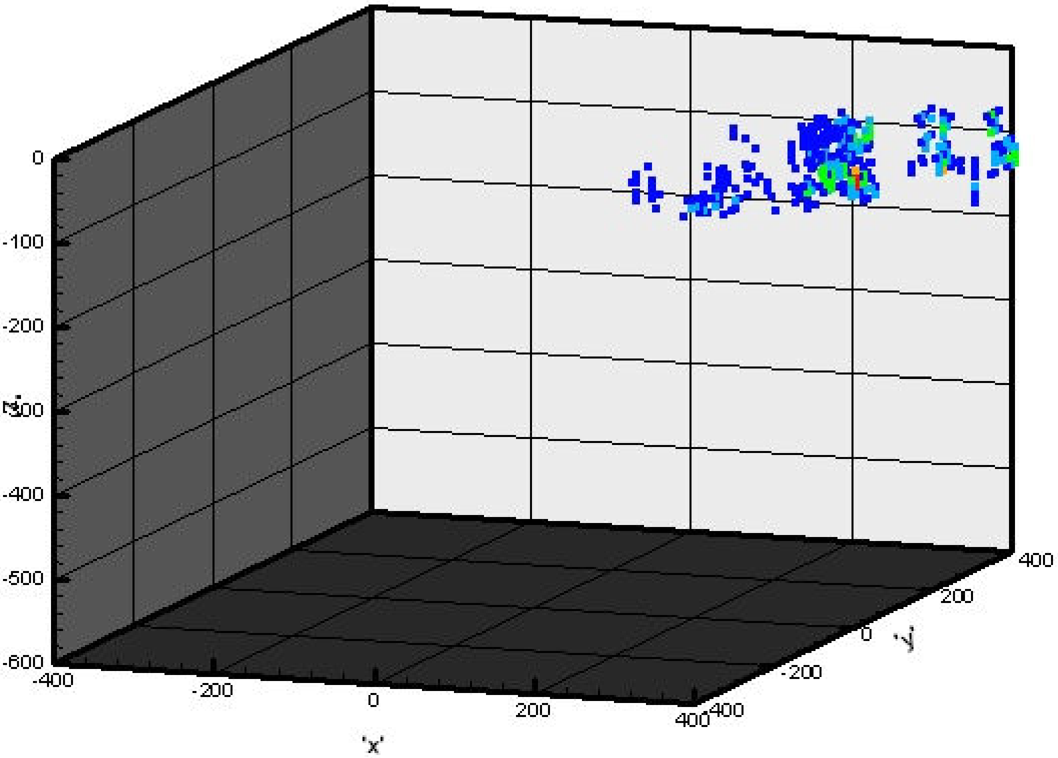

Fig 4-13 3D imaging result by IP mid-point mapping methods

4.1.5. Conclusion

In this section, I conduct GIP transform and IP mid-point mapping for 3D RVSP data to reconstruct the fracture image at MIU project area. GIP transform is more appropriate than conventional IP transform because receivers are planted on the surface as possible as straight lines but some lines are curved.

As I demonstrate and derived with the numerical data, the direction of the strike of a reflector is determined in IP domain by GIP transform. I try to follow the same processing but unfortunately, it is too hard to decide the direction of fault. But I could confine the six direction of the strike of reflectors with the help of the previous research such as surface geology survey, borehole logging, surface seismic and so on. The IP mid-point mapping with the GIP transform on the confined directions, give agreeable results of the position of faults except for one case. The one case is supposed to the signal decrease with long distance from the sources and the problem would be solved by getting more data on the deeper source depth.

4.2. Multi-offset VSP data

4.2.1. Field description

VSP survey is done to survey the geological structure like the fault, fracture and discontinuity in middle area of Korea, Daejeon. Two horizontal tunnels are excavated and they cross vertically at 165m from entrance of long tunnel (Fig 4-14). One borehole (DB-1) is drilled to 500m depth at the end of small tunnel. 8 sources are placed along the bottom of tunnels and the sources from SP1 to SP4 are set along short tunnel. The others are placed along long tunnel as illustrated in Fig 4-14. The SP1 is the nearest shot point of all to the vertical hole (DB-1) whose offset is 2.5m and the farthest shot point from DB-1 is SP8 located at the left end of long tunnel. The data acquisition are summarize in Table 4-2.

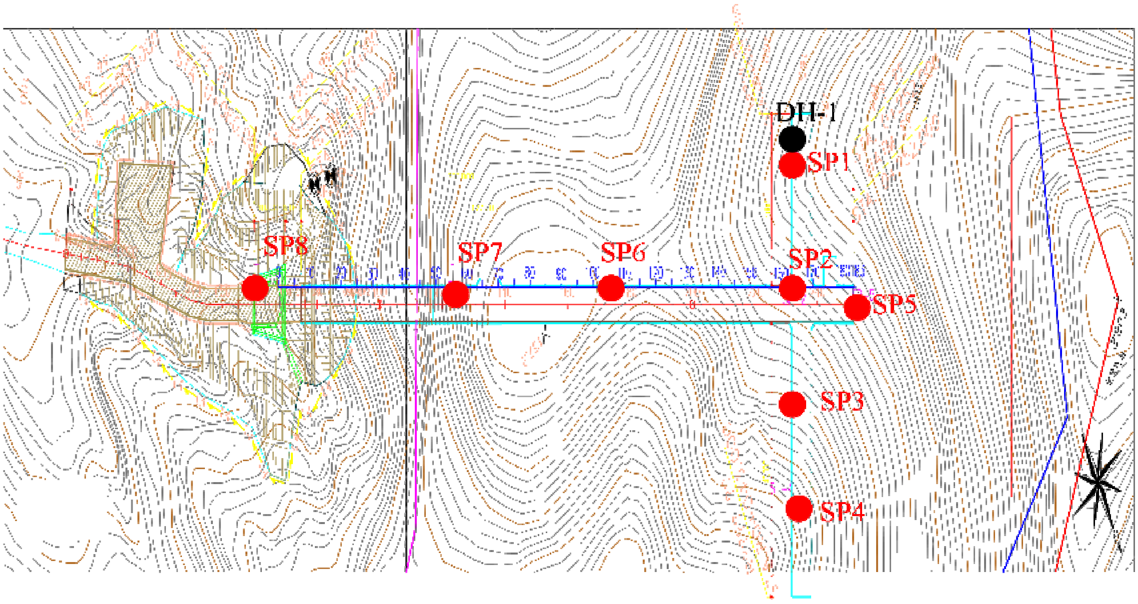

Fig 4-14 Geometry of VSP survey

Table 4-2 Summary of the VSP data acquisition

Receiver No.	61 channels	Receiver Type	40Hz Hydrophone
Receiver interval	5m	Recording Depth	0m-300m
Sampling rate	62.5μsec	Sample	8192 points
Pre-trigger	6.4msec	Shot point	8 points
Source type	Dynamite	Source depth	1-2m

4.2.2. Preprocessing

The original records for every 8 sources are shown in Fig 4-15 and the records are arranged from left, SP1 to right, SP8. The preprocessing is carried out by one of the most useful commercial tools to analyze the reflection seismic data, namely, ProMax software provided by Halliburton.

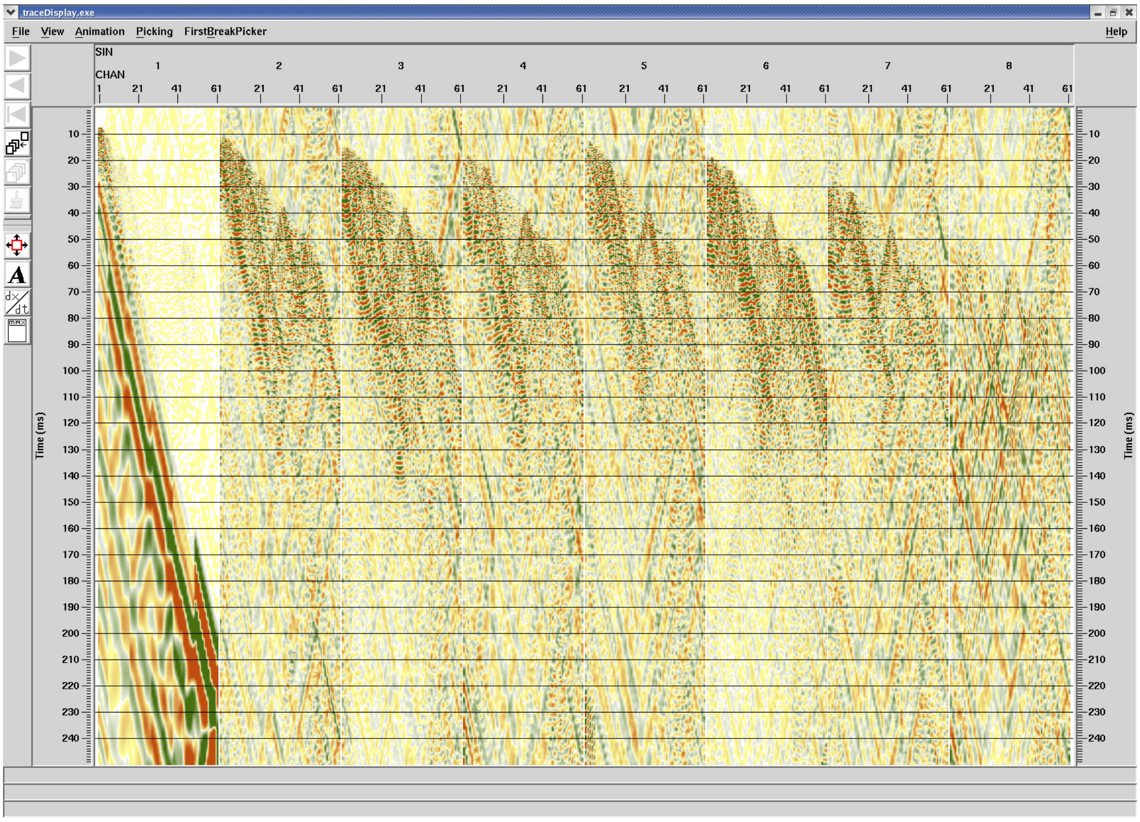

Fig 4-15 Original shot records

As seen in the shot records, the tube waves are notable regardless of the source points. Especially, the tube wave of SP1 is the most remarkable and it arises from the top of the borehole near the source and propagates along the borehole water. The record of SP8 is hardly seen the direct wave because the offset is far from the source and attenuation is happened during the propagation.

Spectrum analysis

To know the frequency band of the records, spectrum analysis is done and illustrated in Fig 4-16 and Fig 4-17 for all sources. As expected from original shot records, the spectrum of SP1 is remarkable at 20Hz – 40Hz range compared to others. However, the spectrum of other shot points also has the same peak except for SP6 and direct waves are much clearly seen in original records compared to other shot points.

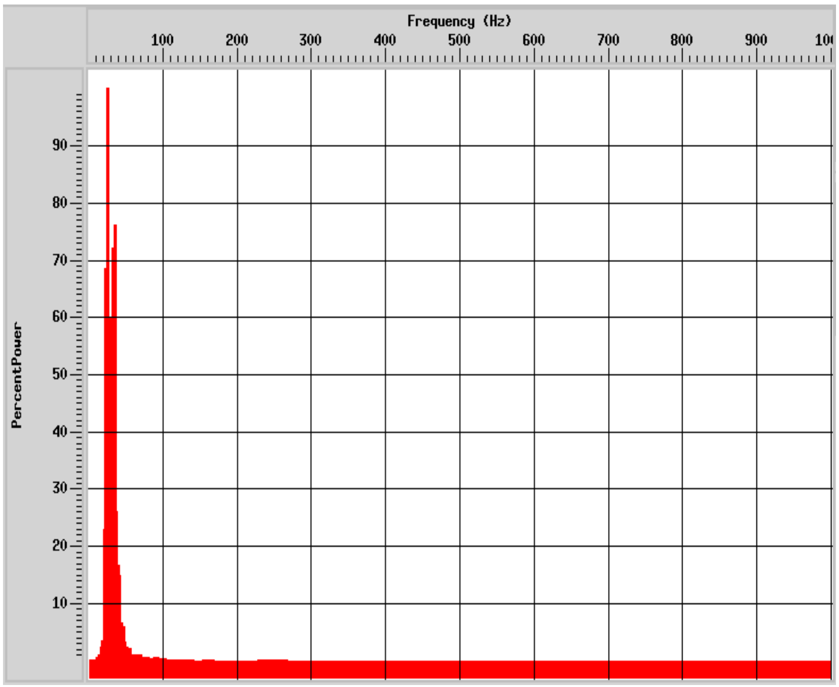

(a) Spectrum of SP1

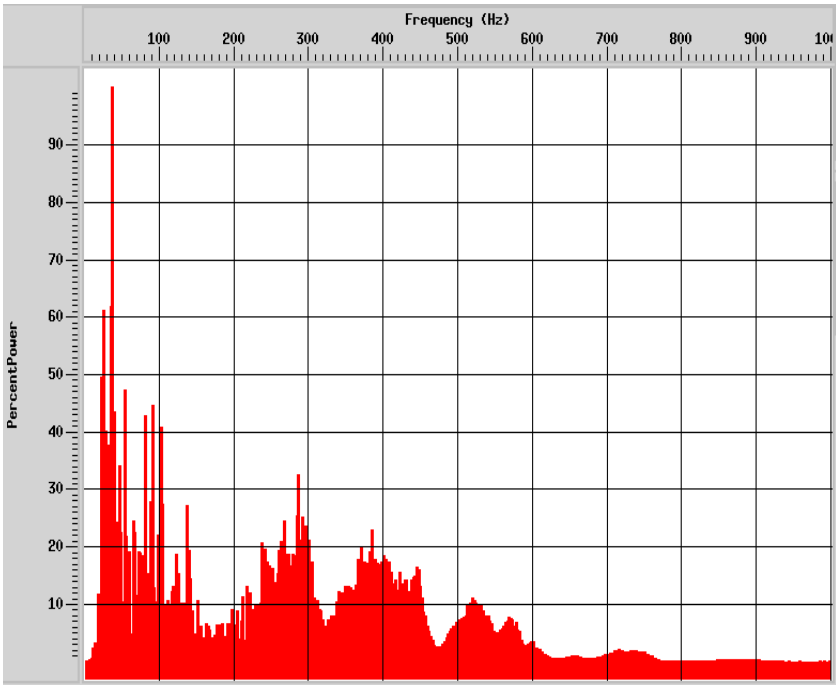

(b) Spectrum of SP2

Fig 4-16 Spectrum analysis of SP2 and SP2

The electrical noises are also seen periodically in the multiples of 60Hz. Compared to the long offset data such as SP8, near offset data such as SP 3 and SP6 have high frequency range because of the attenuation of high frequency.

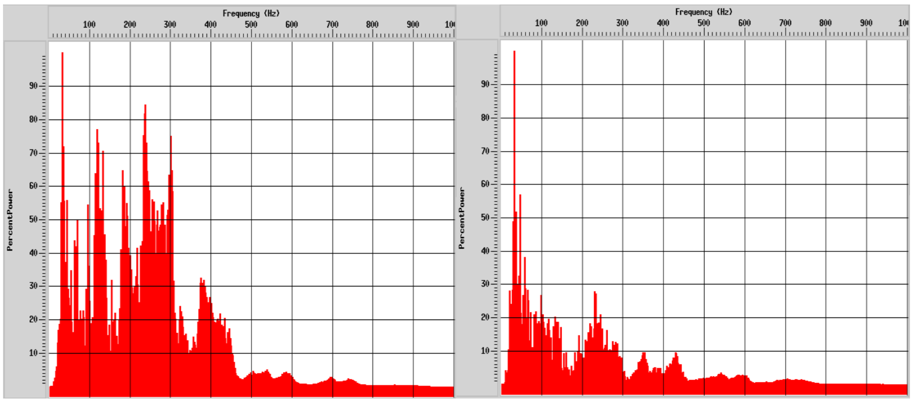

(a) Spectrum of SP3 (b) Spectrum of SP4

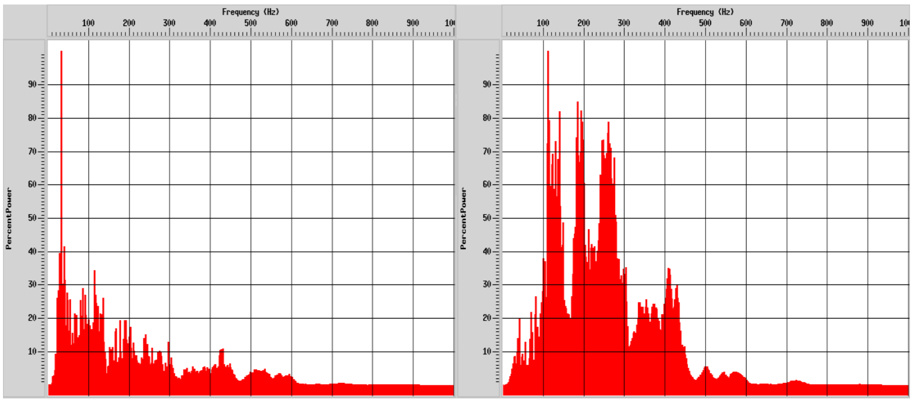

(c) Spectrum of SP5 (d) Spectrum of SP6

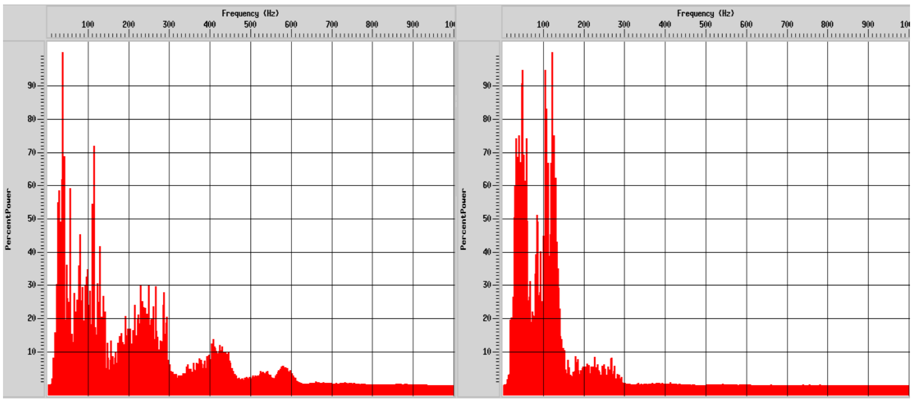

(e) Spectrum of SP7 (f) Spectrum of SP8

Fig 4-17 Spectrum analysis of other source points

4.2.3. Remove tube waves

The frequency range is determined as 80Hz – 900Hz by the spectrum analysis and the results of band pass filter are illustrated in Fig 4-18. The direct waves are enhanced and the tube waves from the top of the borehole are decreased but still seen and notable in SP1. Although S/N ratio is enhanced by band pass filter, there are still notable of tube wave between the recording depths. Three starting points of the tube waves are seen in the records except for that of top of the borehole. Tube wave happens at the top and bottom of the hole and also happens around the fracture zone. The velocity of the tube wave is same to water velocity, that is, about 1500m/sec and these tube waves mask the reflection waves. Therefore, the tube waves must be removed or minimized to enhance the reflection.

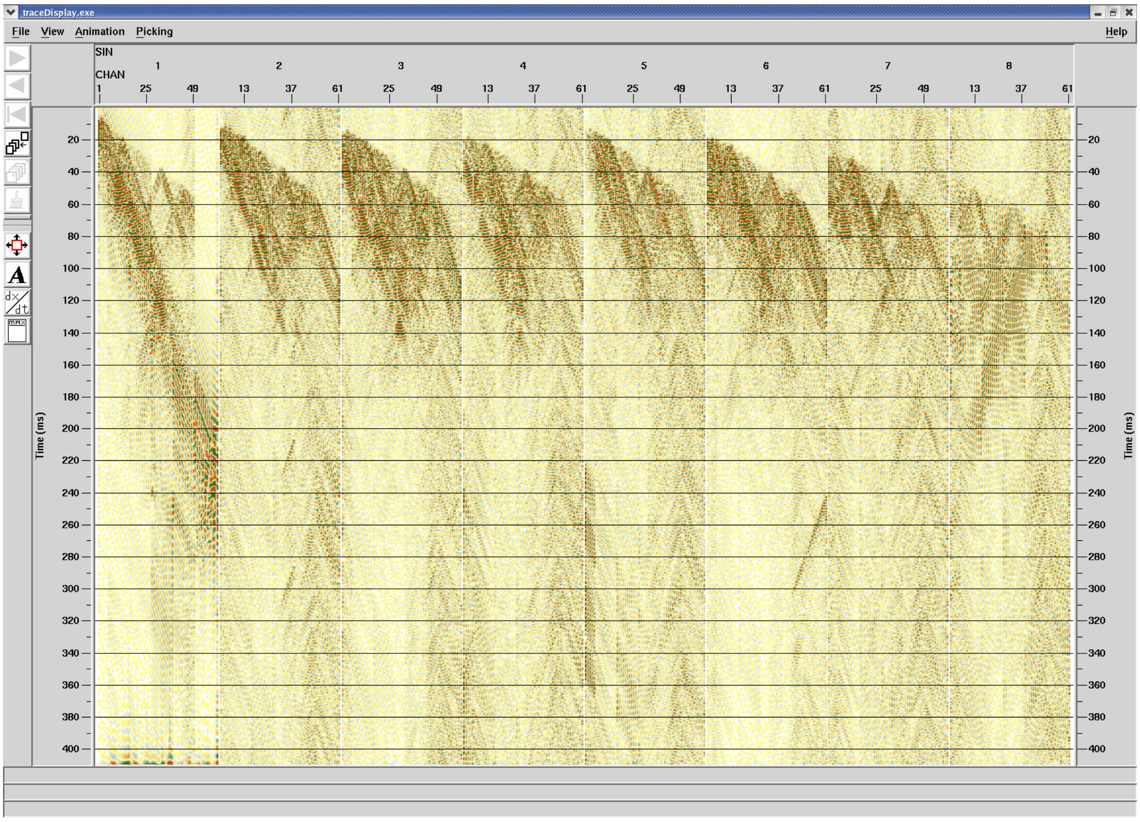

Fig 4-18 Band pass filter results of the original data shown in Fig 4-15

Generally, some filters such as velocity filter, median filter(Hardage,1981) and SVD (Hardage,1992) are available for removing a tube wave in VSP survey. The velocity filter named F-K filter is used to remove the wave which has specific velocity. Usually, F-K filter is used to remove the shear wave(S waver) or ground roll in the land reflection seismic because the velocities of those are slower than compression waves (P wave) and easily confined in F-K domain. As illustrated in Fig 4-18, the S wave and ground roll are not dominant in this survey but tube waves are.

The F-K spectrum result of SP7, for examples, is shown in Fig 4-19 and the others are depicted in Figs 4-20 and 4-21. Three tube wave pairs of up-going and down-going waves are well identified and three starting points of the tube waves are about 60m, 160m and 220m in depth, which are associated with the fracture zones. The zones of blue lines are considered as those affected by tube waves and needed to be removed. Because of the tube in SP1 of top of the borehole, tube waves of SP1 are not much clearer than those of the other source points, however velocity of tube waves can be identified in SP1(Fig 4-21(a)).

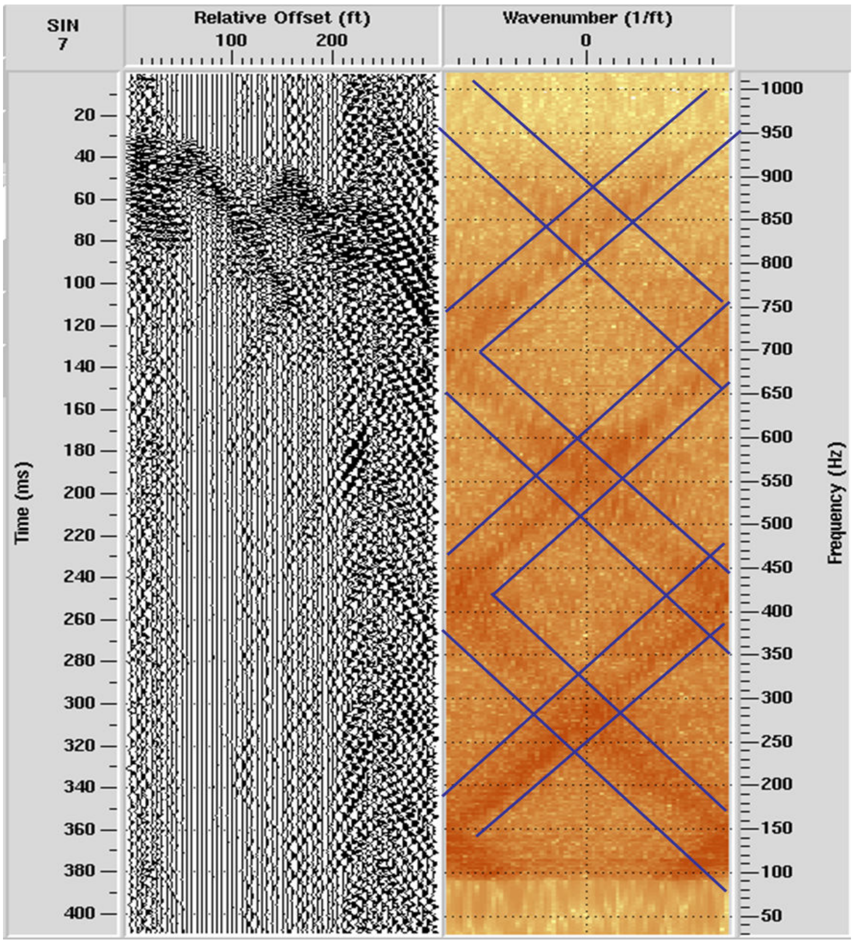

(a) (b)

Fig 4-19 Example of F-K analysis of SP7 and left figure (a) is wavelet and right one (b) is 2D Fourier transform.

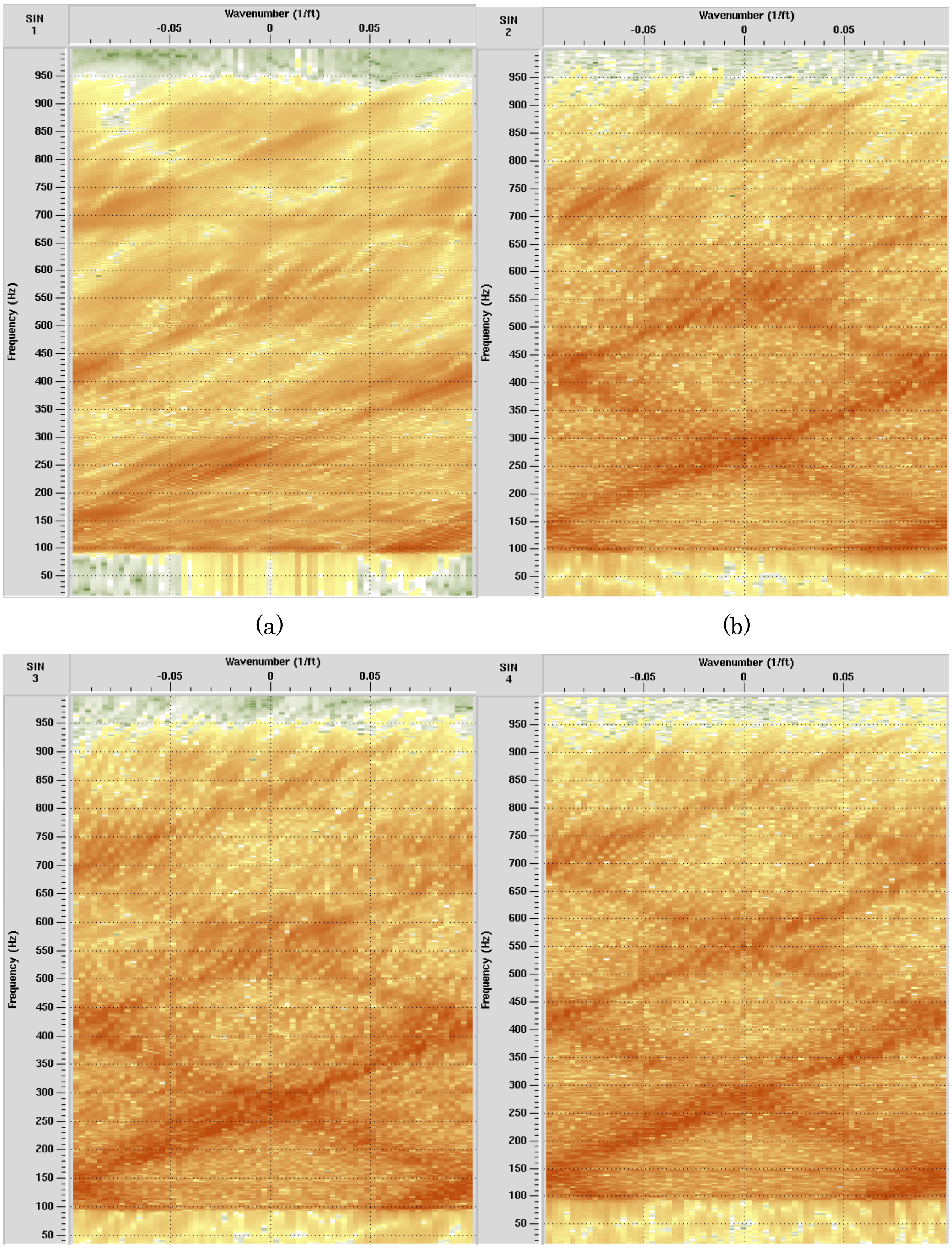

(a) (b)

(c) (d)

Fig 4-20 F-K analysis results for the SP1 (a), SP2(b), SP3(c) and SP4(d)

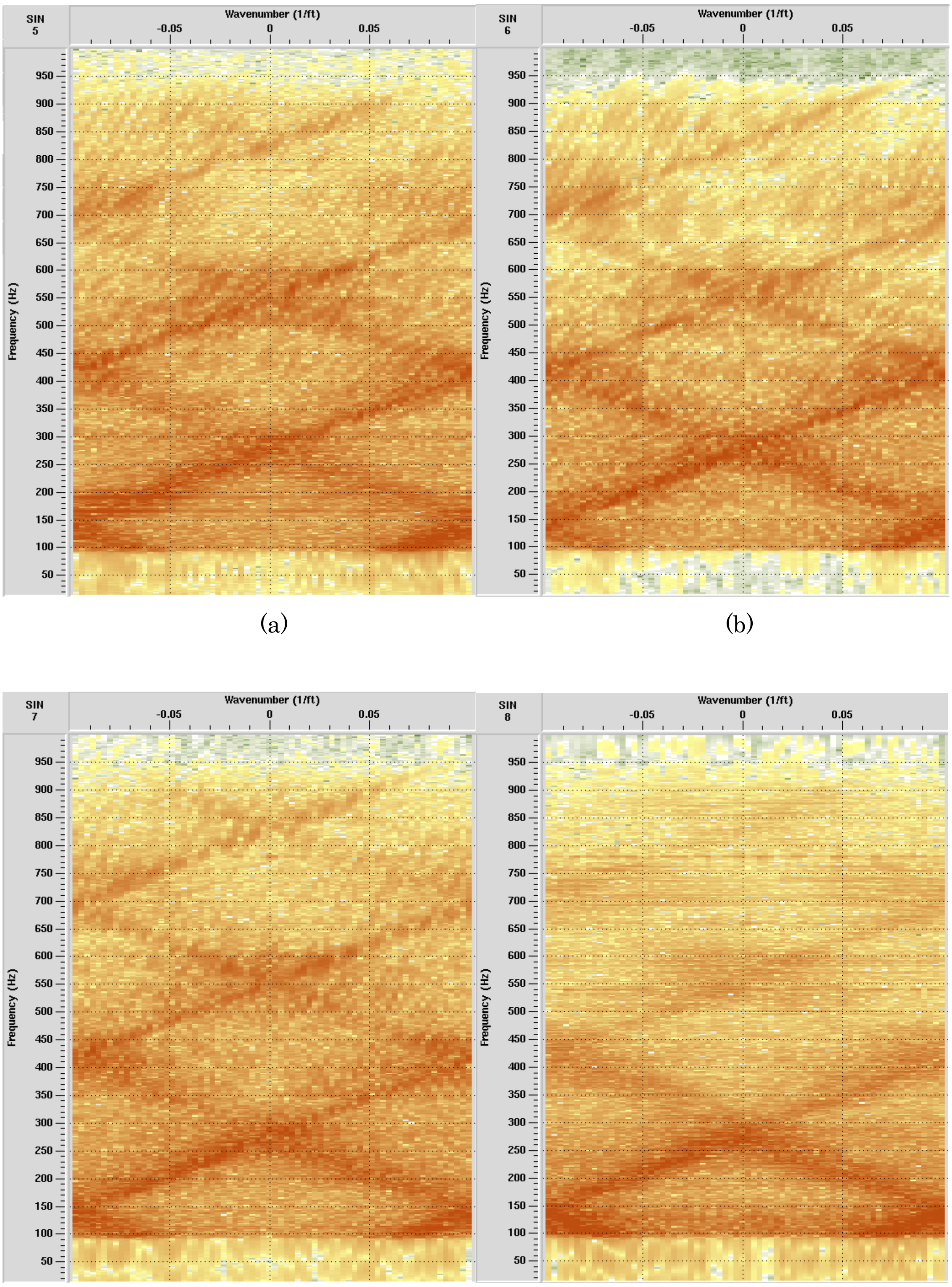

(a) (b)

(c) (d)

Fig 4-21 F-K analysis results for the SP5 (a), SP6(b), SP7(c) and SP8(d)

The results of velocity filter in F-K domain and muting the direct wave by the picking the first arrival, are illustrated in Fig 4-22. The almost tube wave are decreased or minimized and therefore waves considered as the reflection waves are revealed. For example, the up-going waves around 70msec in every source points can be seen and these do not have the velocity of water which is illustrated with red line in Fig 4-22.

Although the tube waves are decreased compared to those of the original data, the tube waves are still seen after applying velocity filter as illustrated in Fig 4-22. Especially, the tube wave of SP1 is dominant and is needed to be removed by muting.

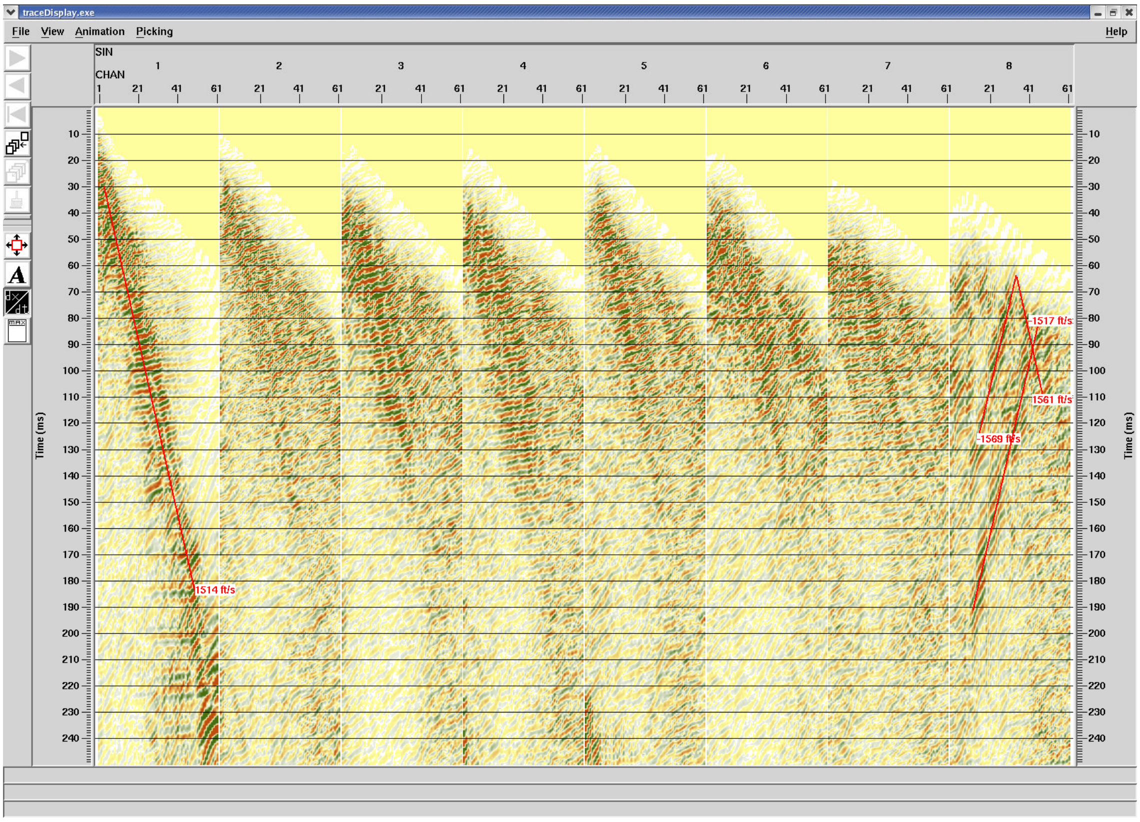

Fig 4-22 Results of velocity filter and mute of direct waves.

The Eigenvalue filter(Freire and Ulrych, 1988) is also usually applied to remove the tube wave and the results are shown in Fig 4-23. After Eingenvalue filter, muting of direct wave and remove of bottom of tube wave of SP1 seen in Fig 4-22 is applied to get the final results shown in Fig 4-23.

Compared the result of velocity filter, the tube wave removal by Eigenvalue filter is more completely done although some waves considered as the reflection are also decreased with the filter. But reflection waves are remained and less contaminated by the tube wave noise.

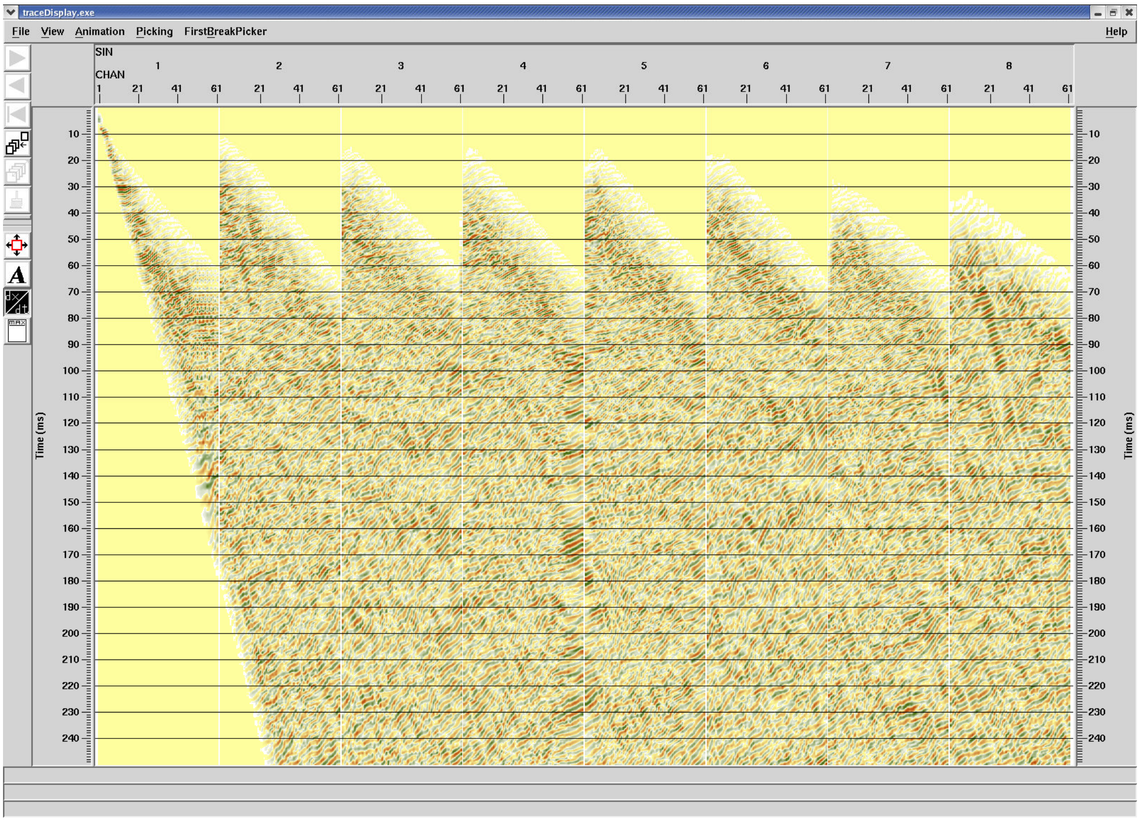

Fig 4-23 Tube wave remove by Eingenvalue filter and muting of direct and tube wave of SP1 for the original data.

4.2.4. IP transform of VSP data

The IP transform results for the band pass filter and muting above the first break are shown in Fig 4-24 and Fig 4-25. The results in Fig 4-24 are calculated when the velocity of the ground is 5400m/sce whereas those in Fig 4-25 are done when that is water velocity, that is, 1500m/sec. As seen from the band bass filtered data (Fig 4-18), the tube waves are dominant and then, it seem also hard to distinguish reflection waves from others in IP domain. The tube waves of this survey are supposed to be originated from the fracture zones near receiver borehole and to be propagated along the borehole water.

By the definition of IP transform, a line in IP domain whose slope is 1 and intercept point is 0 at ξ axis, are equal to the lower part from the top of the receiver borehole. Whereas a line a line in IP domain whose slope is -1 the upper part of the top of the receiver borehole. The line along ξ=0 in IP domain, means the surface line of the survey area.

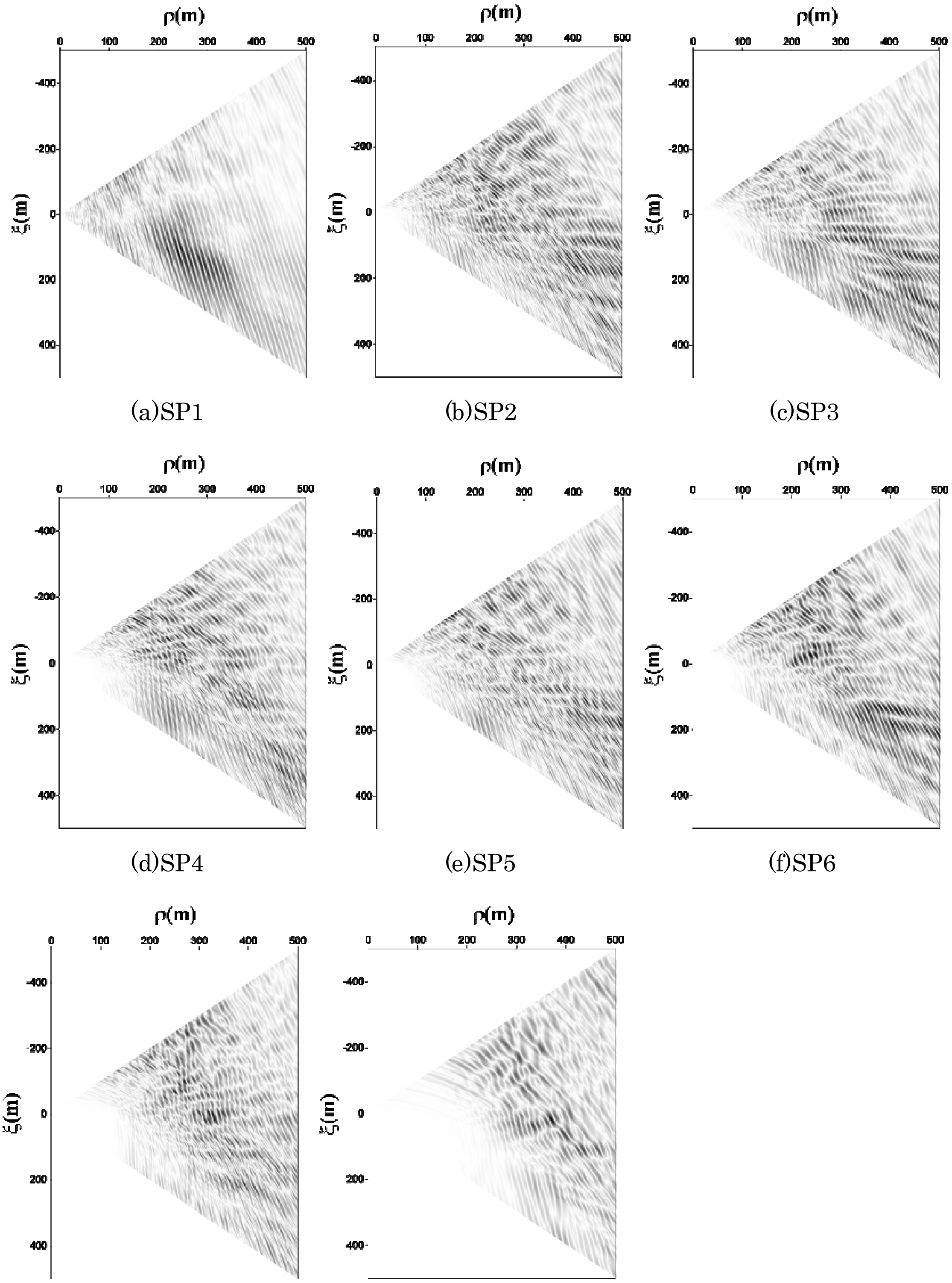

(a)SP1 (b)SP2 (c)SP3

(d)SP4 (e)SP5 (f)SP6

(g)SP7 (h)SP8

Fig 4-24 IP transform result for each source point (Velocity is assumed as 5400m/sec)

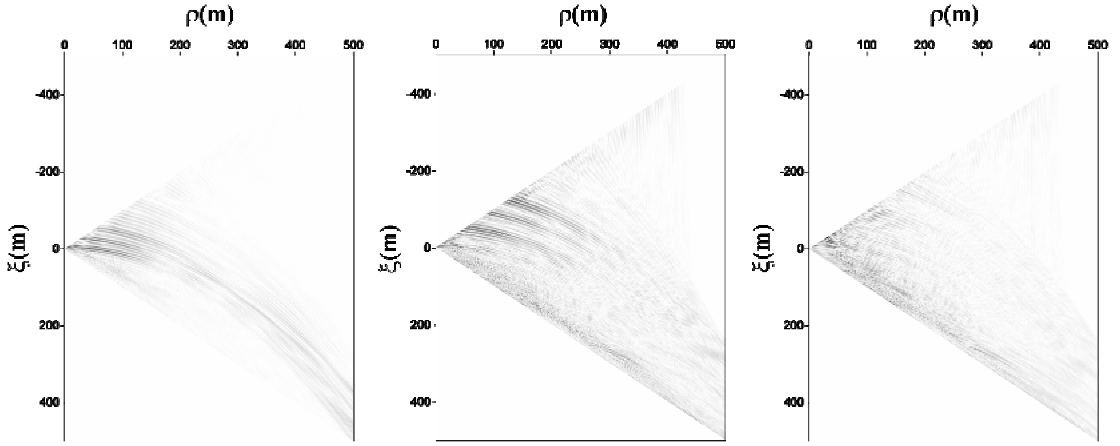

(a)SP1 (b)SP2 (c)SP3

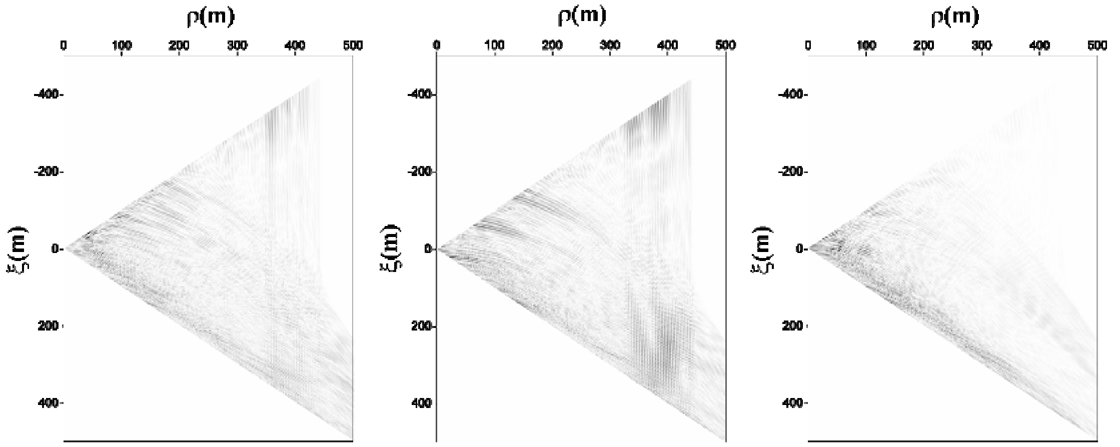

(d)SP4 (e)SP5 (f)SP6

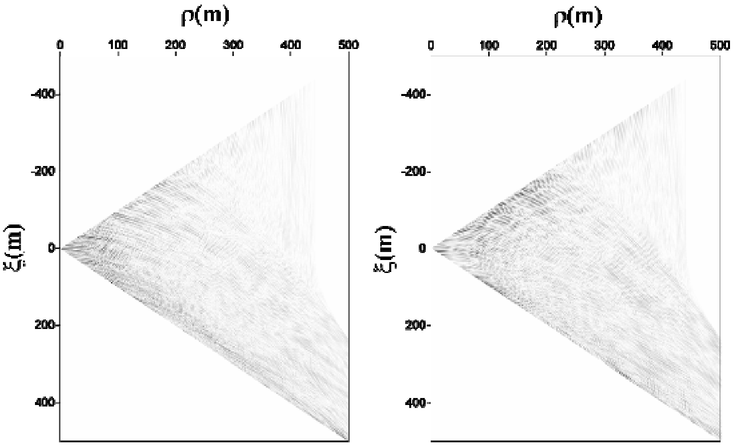

(g)SP7 (h)SP8

Fig 4-25 IP transform result for each source point (Velocity is assumed as 1500m/sec)

As seen from the results in Fig 4-24 and Fig 4-25, the accumulated IPs are located upper parts and these are thought as the tube wave which are first seen in records and multiples. If the positions of tube waves are considered, the IPs of tube waves is located on the line whose slope is 1. Compared with the results in Fig 4-24, it is clearly seen that tube waves are focused on the line of the slope 1 from those in Fig 4-25. It is also clearly seen in Fig 4-25 that the multiple are accumulated in upper parts of ξ because the velocity of the ground assumed in the IP transform coincides with that of the tube wave.

The inverse IP transform results for the data shown in Fig 4-25 are illustrated in Fig 4-26. Before the inverse transform, muting the upper parts of ξ and the area which is close to the line of slope 1 is conducted to remove the multiples and tube wavers. The tube waves are removed not completely but considerably in Fig 4-26 and the reconstructed waves in Fig 4-26 are similar to the velocity filtered waves in Fig 4-22.

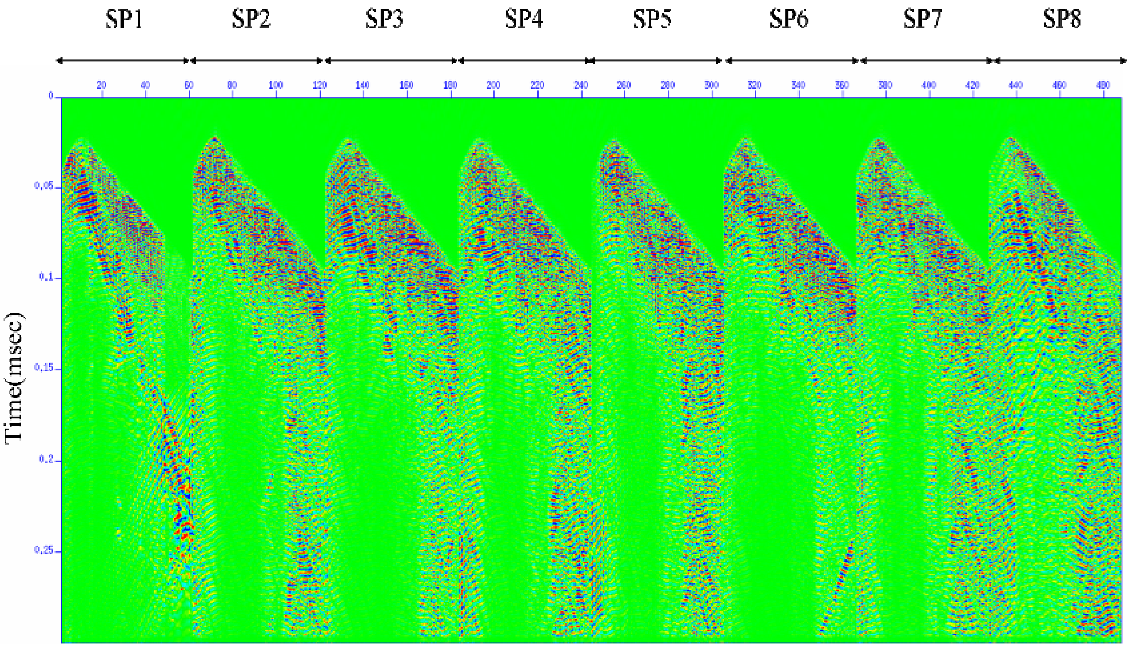

Fig 4-26 Inverse IP transform results for the data shown in Fig 4-25

The results shown in Fig 4-27 are reconstructed waves by inverse transform for the IP transformed data which is calculated for the waves in Fig 4-26 and similar muting processes done in Fig 4-26. Here, the velocity of the ground is assumed as the 5400m/sec which is reasonable and match with that calculated by direct waves. Compared to the results in Fig 4-22 and Fig 4-26, the tube waves are much more removed in Fig 4-27 and that is similar to the results in Fig 4-23 which are those of removal of tube wave by Eigenvalue filter.

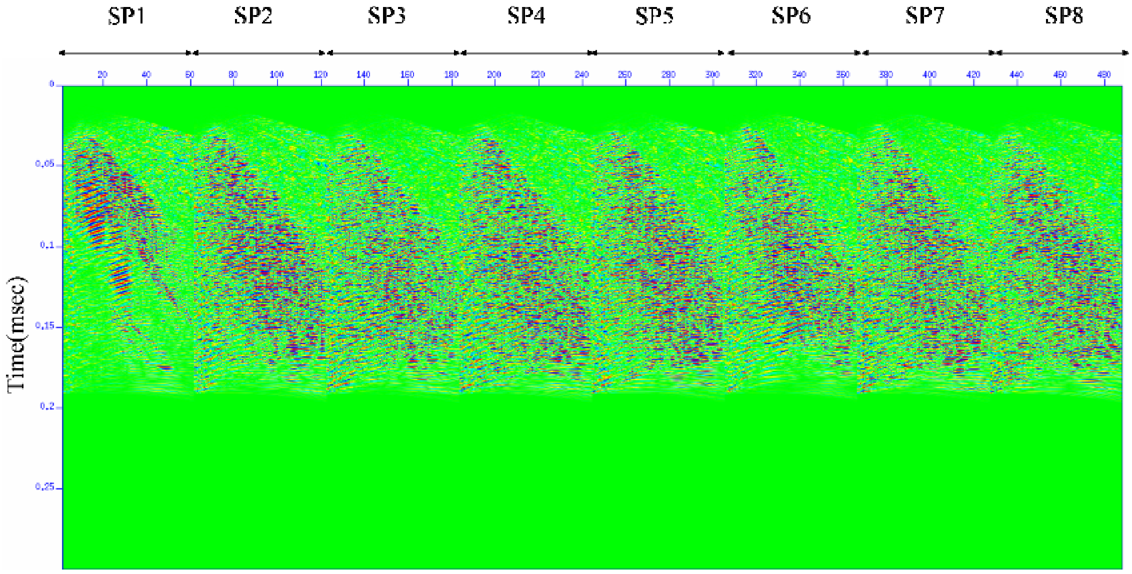

Fig 4-27 Inverse IP transform results for the data shown in Fig 4-25

4.2.5. Imaging and interpretation

In this section, two methods are applied to get final image of the ground and these are Kirchhoff migration scheme which is one of conventional reflection imaging method and the mid-point mapping between the sources and the IP. The velocity of the ground is assumed as the constant velocity, 5400m/sec, in the both of the migration and the mid-point mapping.

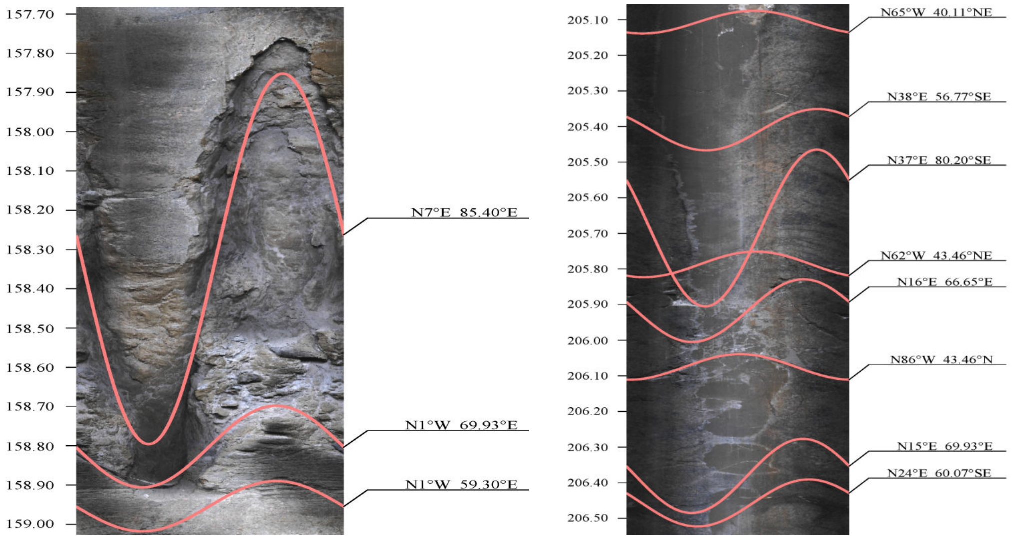

(a) Result around 158m (b) Result around 206m

Fig 4-28 Two examples of borehole camera results

Table 4-3 Summary of strike and dip of DB-1

Depth	Strike	Dip	Aperture	Type	Closed
119.42	N84E	30NW	62.31	Aplitic zone	
124.66	N80W	30NE	32.89	Aplitic zone	
137.93	N66W	45NE	12.73	Joint	Min Fil
138.74	N64W	38NE	7.85	Joint	Min Fil
139.71	N18E	79NW	1.59	Joint	Semi open
140.40	N82W	52NE	3.72	Joint	Min Fil
144.00	N88W	58NE	2.14	Joint	Semi open
145.79	N64E	53NW	2.42	Joint	Semi open
145.83	N66E	77NW	1.81	Joint	Semi open
147.67	N10E	50NW	3.82	Joint	Min Fil
151.69	N10W	75NE	1.59	Joint	Semi open
156.50	N16W	82NE	2.60	Joint	Semi open
156.77	N26W	32SW	206.31	Fault	
157.00	N3 E	82NW	3.92	Joint	Semi open
157.35	N43W	9 SW	3.95	Joint	Semi open
158.32	N7 E	85SE	15.41	Joint	Open
158.80	N2 W	70NE	2.06	Joint	Semi open
161.29	N10E	73SE	3.46	Joint	Semi open
163.11	N38W	72NE	1.90	Joint	Semi open
163.18	N30E	71SE	2.61	Joint	Semi open
168.31	N3 E	71SE	1.93	Joint	Semi open
168.77	N10E	74SE	1.64	Joint	Semi open
177.87	N66E	34NW	52.82	Aplitic zone	
180.13	N20E	61NW	45.86	Aplitic zone	
205.11	N65W	40NE	0	Joint	Closed
205.41	N38E	57SE	0	Joint	Closed
205.69	N37E	80SE	0	Joint	Closed
205.92	N16E	67SE	0	Joint	Closed
206.08	N87W	43NE	0	Joint	Closed
206.38	N15E	70SE	0	Joint	Closed

Borehole camera is conducted in the receiver borehole, DB-1 to investigate the dips and the strikes of fractures around the borehole. The results are shown in Fig 4-28 and those are parts of the full 300m depth and the information of the strikes and the dips considered as important are summarized at Table 4-3. The dips of fractures of the borehole are considerably high as seen in Fig 4-28. Fractures are concentrated around two depths, 158m and 206m, where the tube waves happen as seen in Fig 4-18. This fact is also derived from the velocity and the density logging results for the borehole as illustrated in Fig 4-29.

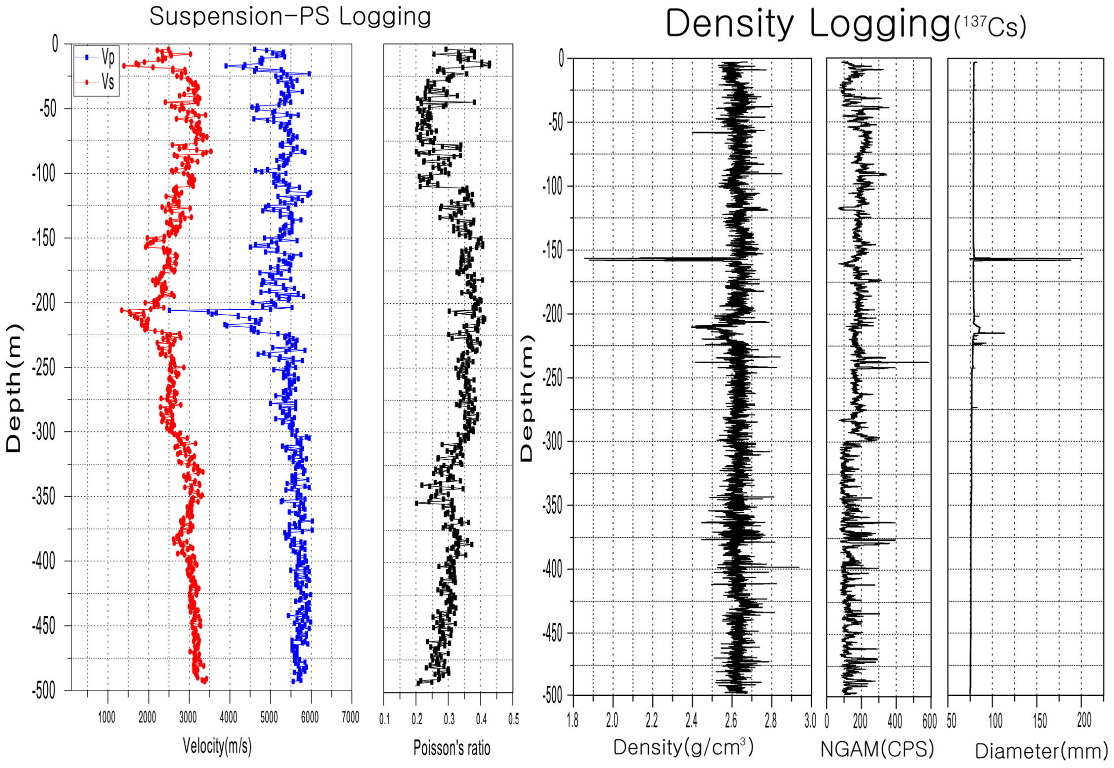

(a) Velocity logging (b) Density logging

Fig 4-29 Velocity and density logging results of the borehole DB-1

Migration

Eikonal equation is applied to calculate the travel time in migration(Gray and May, 1994; Moser, 1994) which is more efficient and faster than the full wave equation. The data shown in Fig 4-23 are used in the Kirchhoff migration and the results of the imaging are illustrated in Fig 4-30 and Fig 4-31. The migration is done for the wide range (Fig 4-30) and the small range (Fig 4-31) and the reflection angle is limited over than 45 degree because the high dip fractures are dominant, however, the low dip ones exist as well. Zero position of horizontal direction coincides with the top of the borehole.

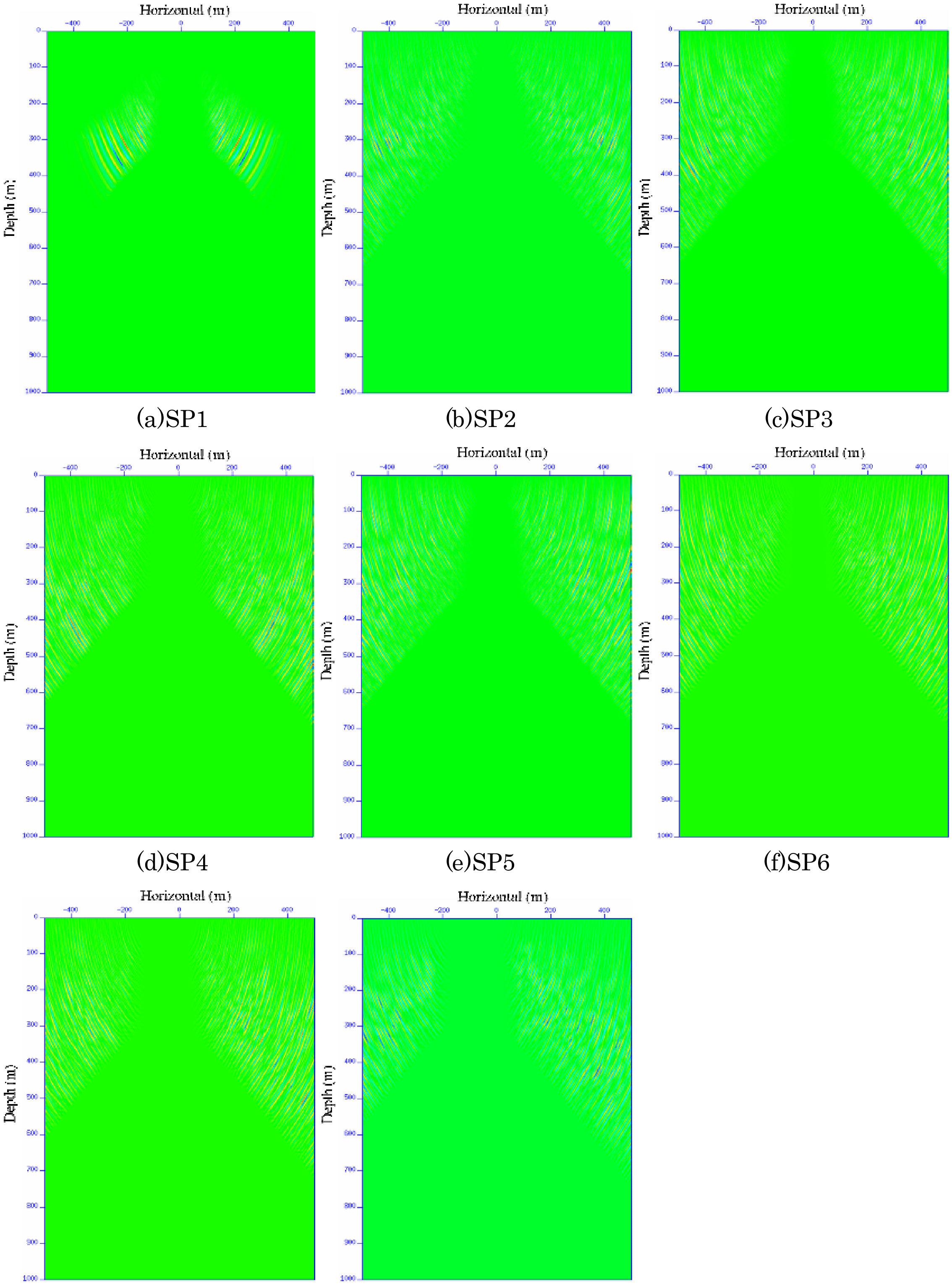

(a)SP1 (b)SP2 (c)SP3

(d)SP4 (e)SP5 (f)SP6

(g)SP7 (h)SP8

Fig 4-30 Migration of each source point for the wide mapping range(1000m x 1000m) and the high reflection angle （$> 45^0$）

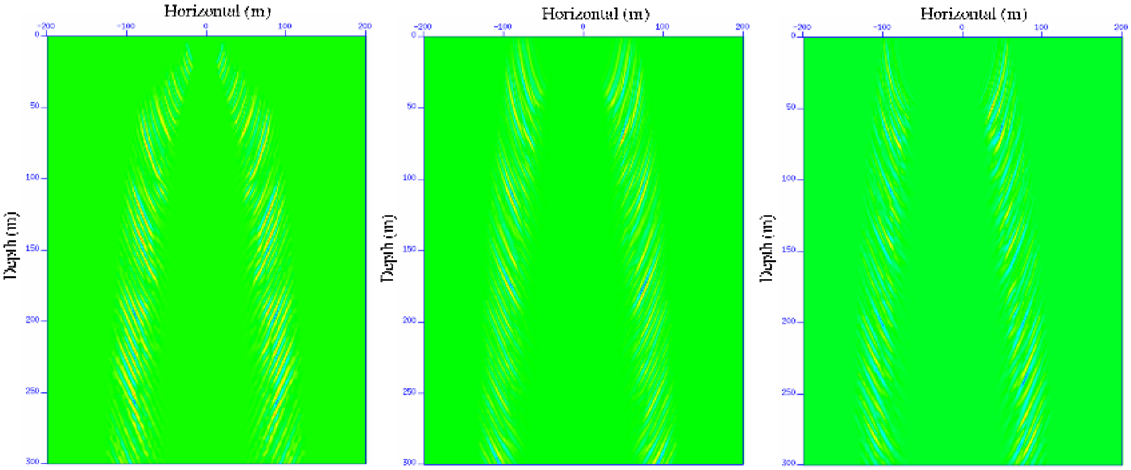

(a)SP1 (b)SP2 (c)SP3

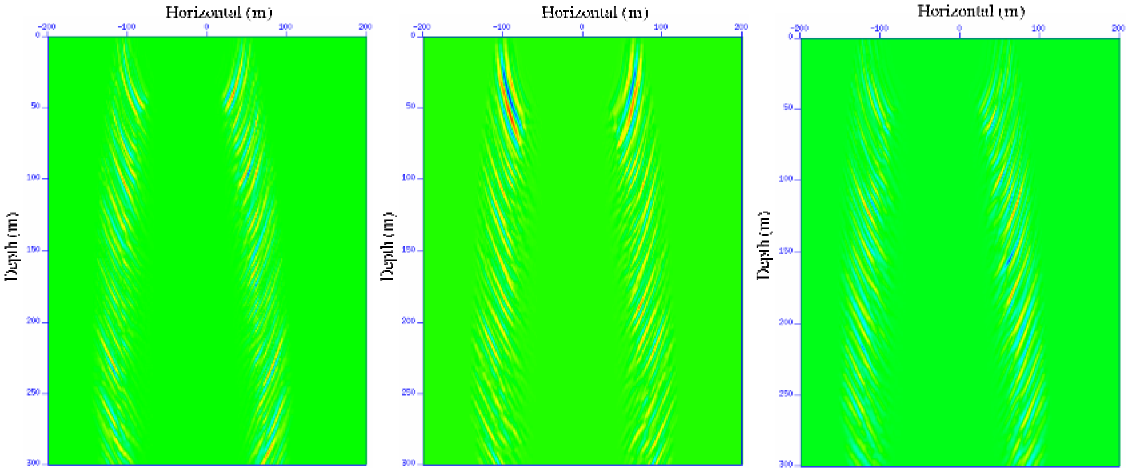

(d)SP4 (e)SP5 (f)SP6

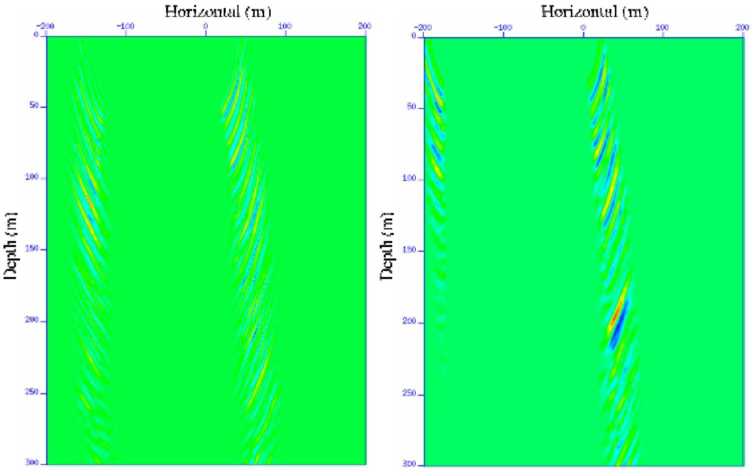

(g)SP7 (h)SP8

Fig 4-31 Migration of each source point for the small mapping range (400m x 300m) and the high reflection angle (> 45^0)

As we know the geometry of sources and receivers illustrated in Fig 4-14, one receiver hole, DB-1 and the sources from SP1 to SP4 are located on almost straight line along the short tunnel. Because of this fact, the results from SP1 and SP4 can be stacked and are illustrated in Fig 4-32.

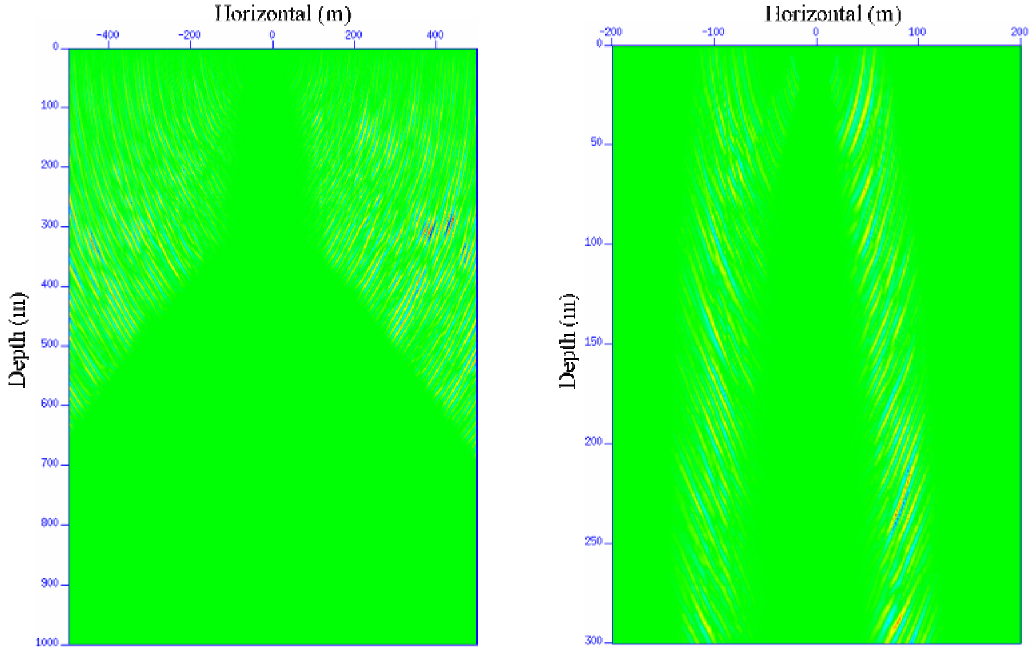

(a) Wide Range (1000m x 1000m) (b) Middle range (400m x 300m)

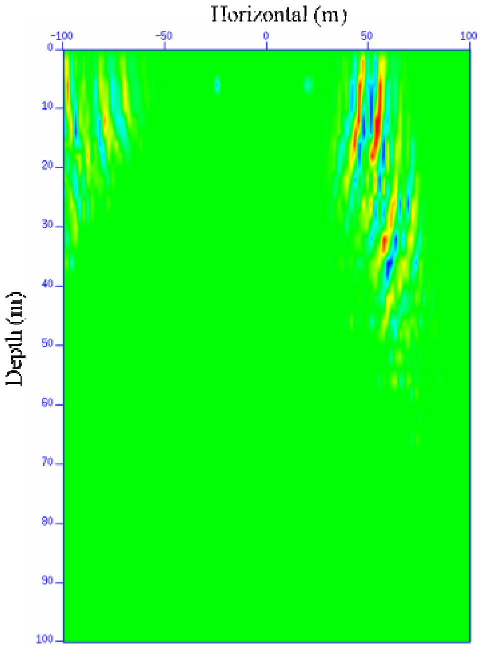

(c) Narrow range (200m x 100m)

Fig 4-32 Stacked results of the data of SP1, SP2, SP3 and SP4 illustrated in Fig 3-30 and Fig 30-31

In wide range case (Fig 3-32 (a)), some enhanced reflection images are seen around 350m depth and these have about 55^0 ~ 65^0 range of dip angles. The dips of images in middle and narrow ranges (Fig 3-32(b) and (c)) are showing similar to those of wide range. The kirchhoff migration scheme for delta function in homogeneous medium show the circular image and therefore, the migration result for one source shows the symmetric feature according to the geometry of receivers and the source and this fact is seen from the results in Fig 4-30 and Fig 4-31. The symmetry are collapsed by stacking the data as illustrated in Fig 4-32 , that is, the parts concerned with the reflection is enhanced while the other is decreases by staking.

Fig 4-33 shows the fracture distribution maps for the over 60^0 dip angle on the vertical section with the line along the short tunnel where the source point form SP1 to SP4 and the borehole lay. The fracture distribution maps are derived from the borehole camera and they are assumed to be extended to the surface. The green lines in Fig 4-33 represent the mineral filling fractures, the blue ones represent the closed fractures and the red ones do the closed fractures. The left figure (Fig 4-33(a)) is the map using the full depth data while the right one (Fig 4-33(b)) is the map using the limited data from 140m to 250m depth. As seen from the maps of both, the dips of fractures tend to be inclined from right-top to the left-down. The reason why the low dip angle is seen in the figures although only over 60^0 dips are used to make the maps, is because the dips of the figures are not true dips but only apparent ones, that is, the dips vary along the view points.

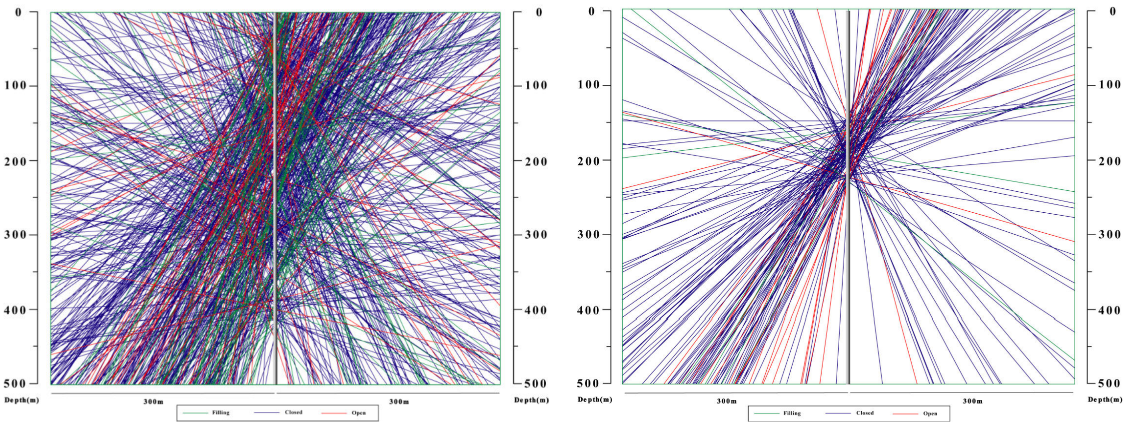

(a) Data with full depth (b) Data with 140m-250m

Fig 4-33 Fracture distribution map on the vertical section of the short tunnel

As seen in Fig 4-33, the apparent dip angles are distributed widely but dominant ones are high and calculated as about 55 ~ 65 degree for the left inclined fractures and

45 ~ 70 degree for the right inclined ones. The apparent dips from the results illustrated in Fig 4-32 (b) and (c) gives acceptable results with the fracture distribution map.

The migration for the low reflection angle, that is under 5 degree, is also applied to the data of SP1 to SP4 and its' results after stacking are drawn in Fig 4-34. Left figure (Fig 4-34(a) is the color image of wide area and right one (Fig 4-34 (b)) is the wiggle trace image of the narrow area which is illustrated with the red dashed box in Fig 4-34(a). Some strong events are seen in the images around 500m, 600m and 800m. These events could not be identified with the borehole logging data illustrated in Fig 4-28 and Fig 4-29, because of the limitation of logging depth, but are supposed to be concerned with fractures. However, the shallow parts of the figure are well matched with the logging results.

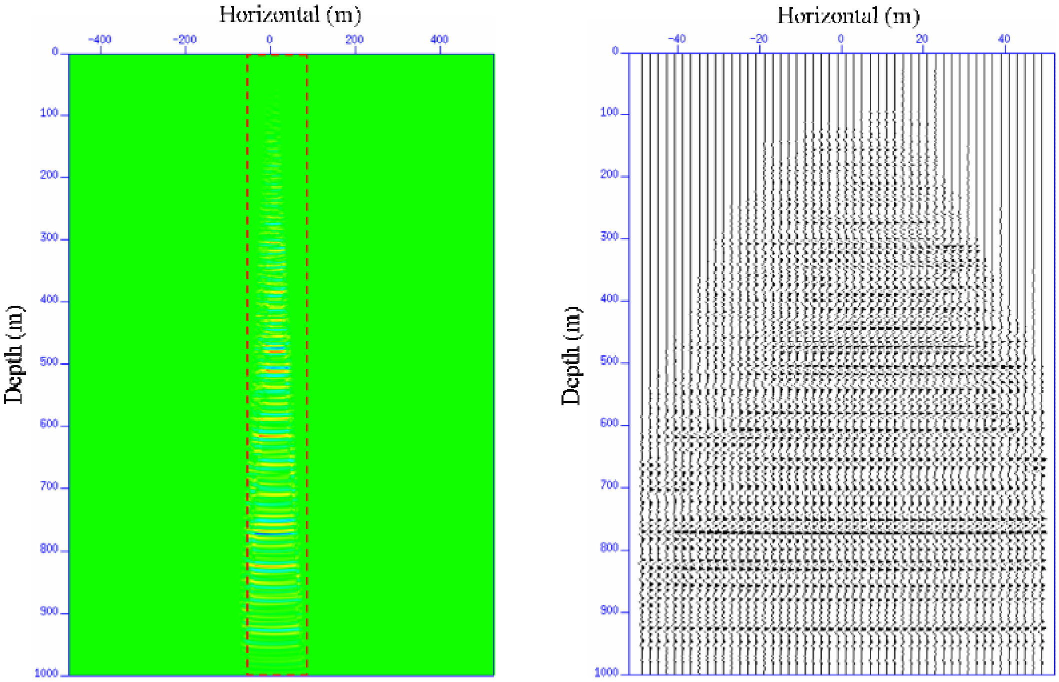

(a) Color image (b) Wiggle image in narrow range

Fig 4-34 Imaging results for the low dip angles under 5 degree by the data of source points from SP1 to SP4

Mid-point mapping with IP domain data

The imaging scheme with mid-point mapping between the IP data and the sources are applied to the data shown in the Fig 4-35. The data are achieved by muting of the top of the first arrival and the below of the special time of SP1 to the wavelet shown in Fig 4-27.

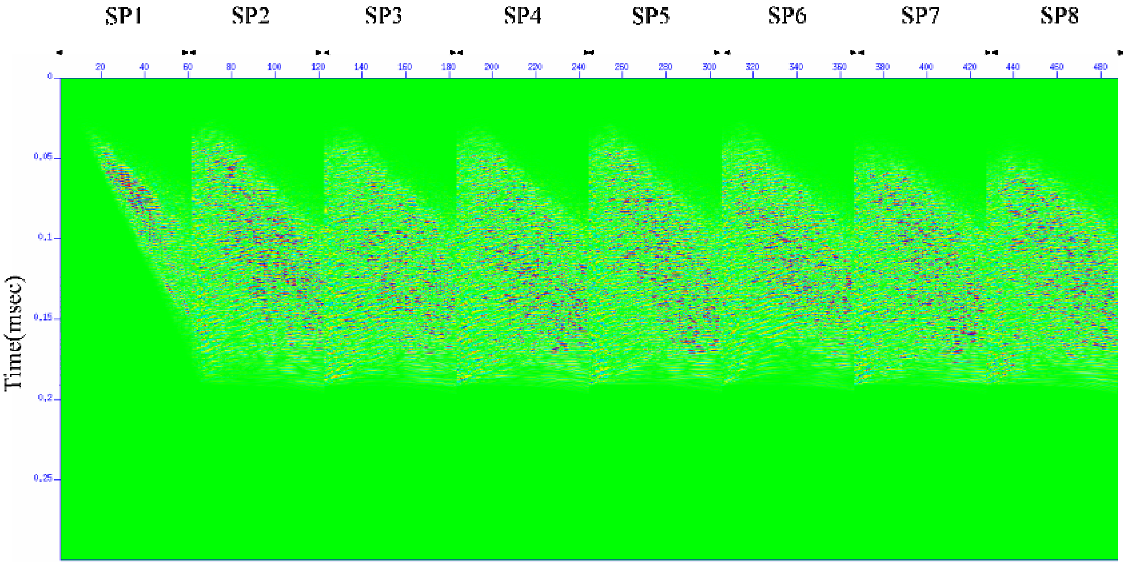

Fig 4-35 Wavelet used to mid-point mapping process

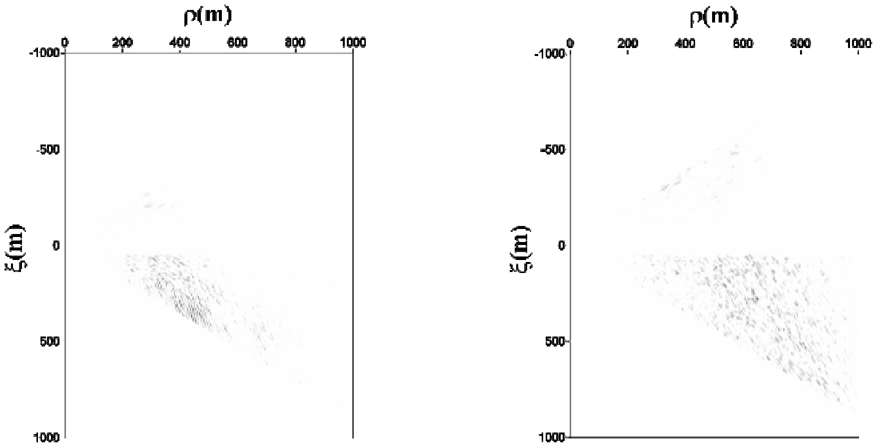

(a) SP1 (b) SP2

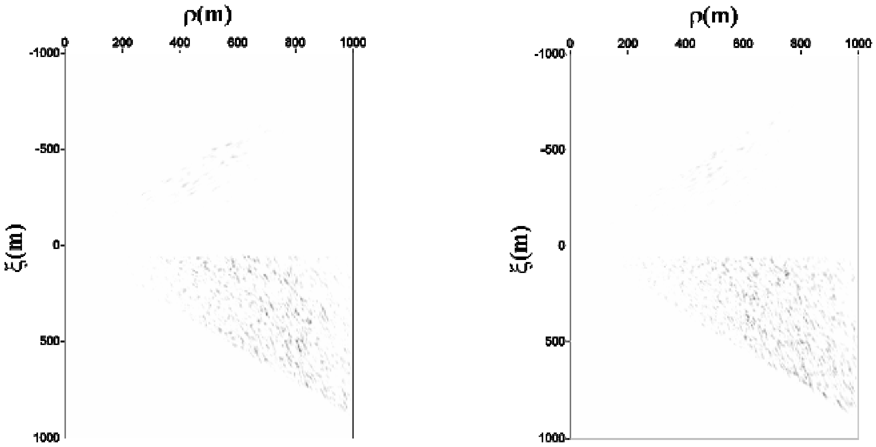

(c) SP3 (d) SP4

Fig 4-36 IP transform result of the data shown in Fig 4-35

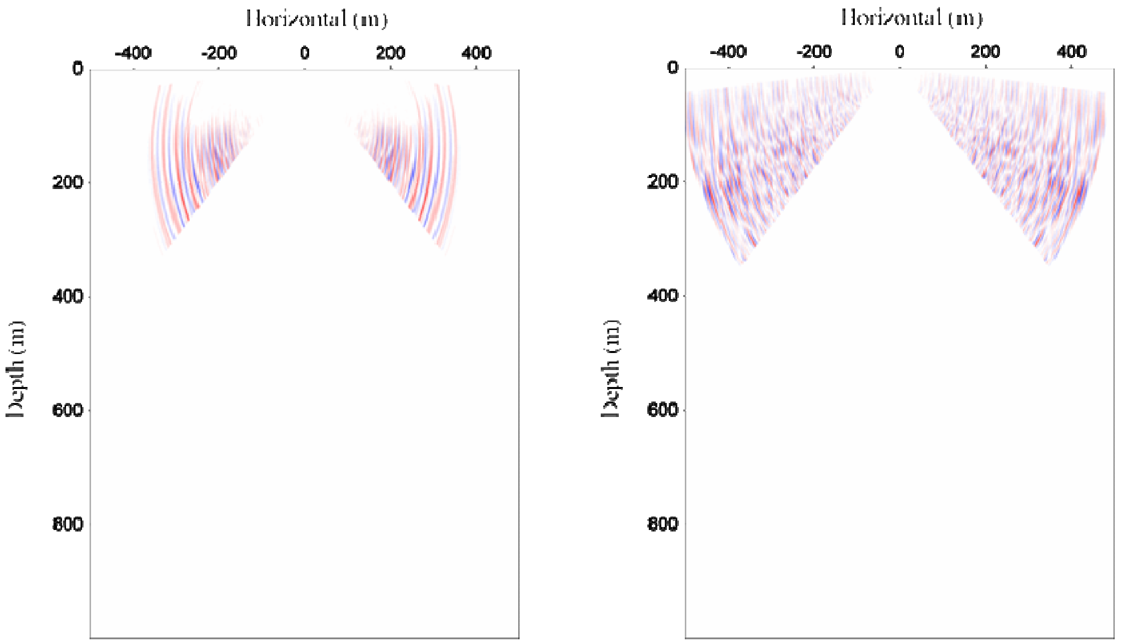

(a) SP1 (b) SP2

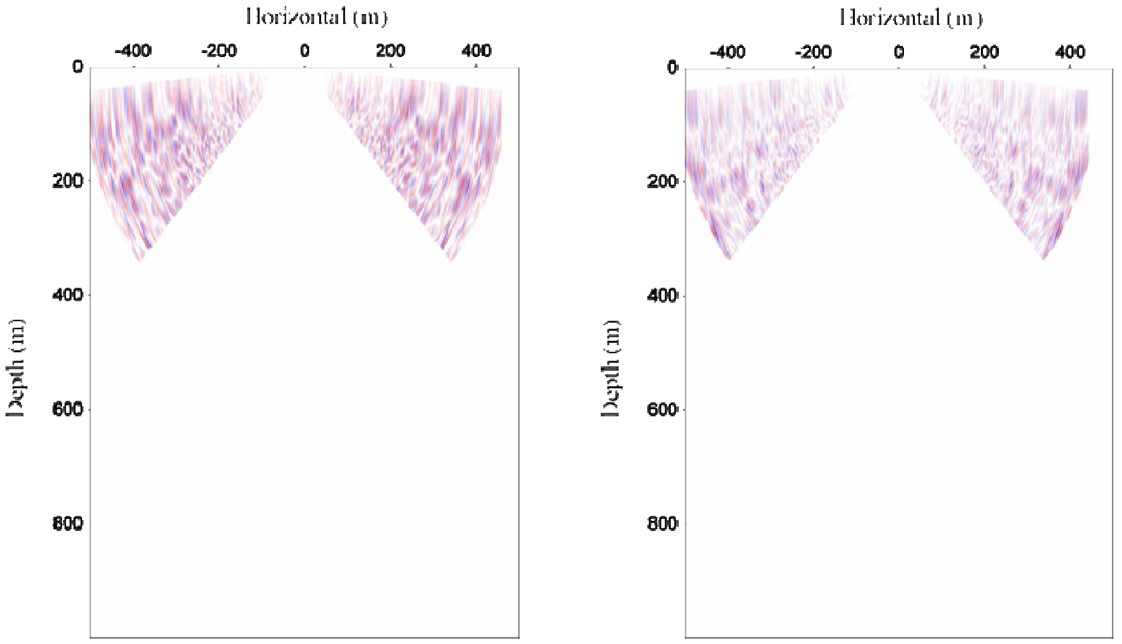

(c) SP3 (d) SP4

Fig 4-37 Mid-point mapping results for the data shown in Fig 4-36

The IP transform results for the data illustrated in Fig 4-35 are shown in Fig 4-36. The tube wave and the upper parts of ξ are removed, which are seen in the IP results of the original data illustrated in Fig 4-24.

The results of mid-point mapping for the data in Fig 4-36 are shown in Fig 4-37 and the dip filter which is limited reflection angle of over than 45 degree is applied to the final results. The imaging results are more localized rather than the results of Kirchhoff migration (Fig 4-30), because of the characteristics of IP transform, that is, concentrating points of the reflection in time domain to one point in IP domain.

The stacking result of 4 sources data (Fig 4-37) are illustrated in Fig 4-38(a) and the Fig 4-38(b) are Kirchhoff migration results and the same figures shown in Fig 4-32(a). The three lines shown in Fig 4-38 are derived by imaging results and the fracture distribution. The red dash lines are the reflection lines derived by the results of mid-point mapping. The imaged points by mid-point scheme (Fig 4-38(a)) are seemed to up-shift along the line compared to those by Kirchhoff migration (Fig 4-38(b)) because the mid-point mapping scheme images the mid point between the IP of a reflection plane and a source not the reflection point. The dip angles calculated by the result of the mid-point mapping are considerably high about 60 ~ 70 degrees and this fact shows agreeable result with the fracture distribution map(Fig 4-33).

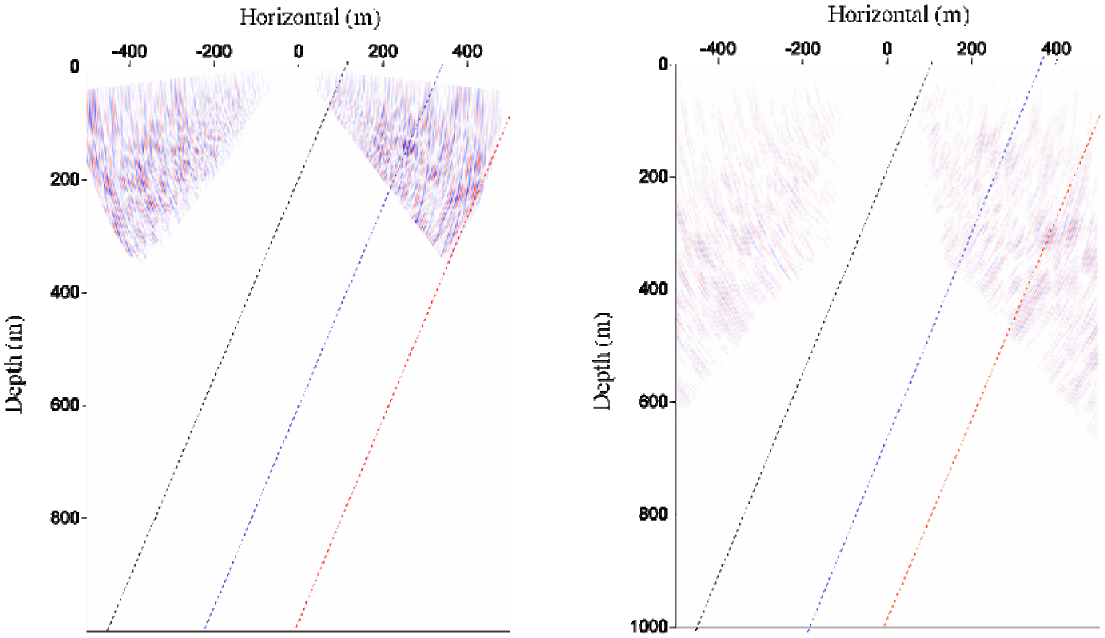

(a) (b)

Fig 4-38 Imaging results by mid-point mapping (a) and Kirchhoff migration (b)

4.2.6. Conclusion

To investigate the ability of IP transform as a filter to remove noisy events and enhance the signal of the reflection events, I compare the results by conventional processing with those by IP domain.

The original recording data of multi-offset VSP survey show a strong tube wave event whose velocity is water and which are originated from the fracture zone of a receiver well, therefore the tube waves make difficult to discriminate between the reflection events and others and are need to be removed.

The tube waves in VSP scheme is positioned along the receiver hole and those are located along straight line whose slope is equal to 1 in IP domain. In addition, the multiples by the ground surface are located in upper side and they are easily removed in IP domain. The effect of filter in IP domain is compared with that by conventional filters of velocity filter and Eigenvalue filter and those results give considerably enhanced data however they have some difference in detail.

I also search the imaging results by IP mid-point mapping and Kirchhoff migration and could conclude that they give an agreement of results, but difference in the exact mapping points which are caused by the intrinsic feature of two imaging schemes. The mapping processing is occurred in the points of the reflection in Kirchhoff migration, while IP mid-point mapping scheme projects the data in the points of the reflector not the reflection.

4.3. Crosswell data

4.3.1. Field description and data acquisition

The field of crosswell data is same to Mizunami where is explained in the previous section 4.1. The crosswell survey is conducted between two holes which are located inside the main shaft and sub shaft respectively (Fig 4-39). As illustrated in Fig 4.1 and Fig 4-39, two shafts are planed to be connected by horizontal tunnel in every 100 m. The crosswell survey is done in two vertical holes drilled from the bottom of the second connecting tunnel located in 200m depth from the ground.

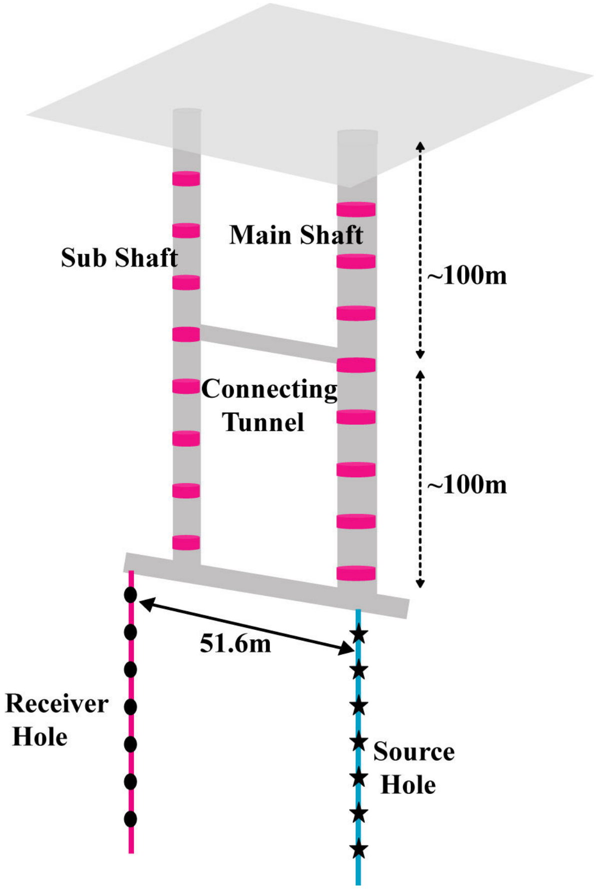

Fig 4-39 Schematic figure of the crosswell survey in Miznami

Sources are excited in the hole of the main shaft side and the waves are recorded at the hole of the other side. Mechanical source of OWS (OYO Wappa Source) is applied in every 4m and totally 30 times to 120m depth. Geophone receivers are adhered to the hole and placed in every 2m. The filed observation is summarized in Table 4-4.

Table 4-4 Summary of the Crosswell data acquisition

Receiver No.	60 channels	Receiver Type	Geophone
Receiver interval	2m	Recording Depth	2m-120m
Source Type	OWS	Source No.	30 points.
Source interval	4m	Source depth	4m-120m
Source Hole	Main shaft side	Receiver Hole	Ventilation side
Sampling rate	62.5μsec	Sampling No.	16000 points

4.3.2. Pre processing of the crosswell data

The original records are illustrated in Fig 4-40. At a glance, waves like the reflection waves are seen under direct waves, for example, the wave around 55miliseconds in source number 2. The wave in source number 2 is moved up according to the source numbers, that is, the depth of sources. The similar waves are also seen 90miliseconds in source number 2 and are moved up as sources are deeper.

If the view point is changed from the source gather (Fig 4-40) to the receiver gather illustrated in Fig 4-41, the waves are undoubtedly tube waves.

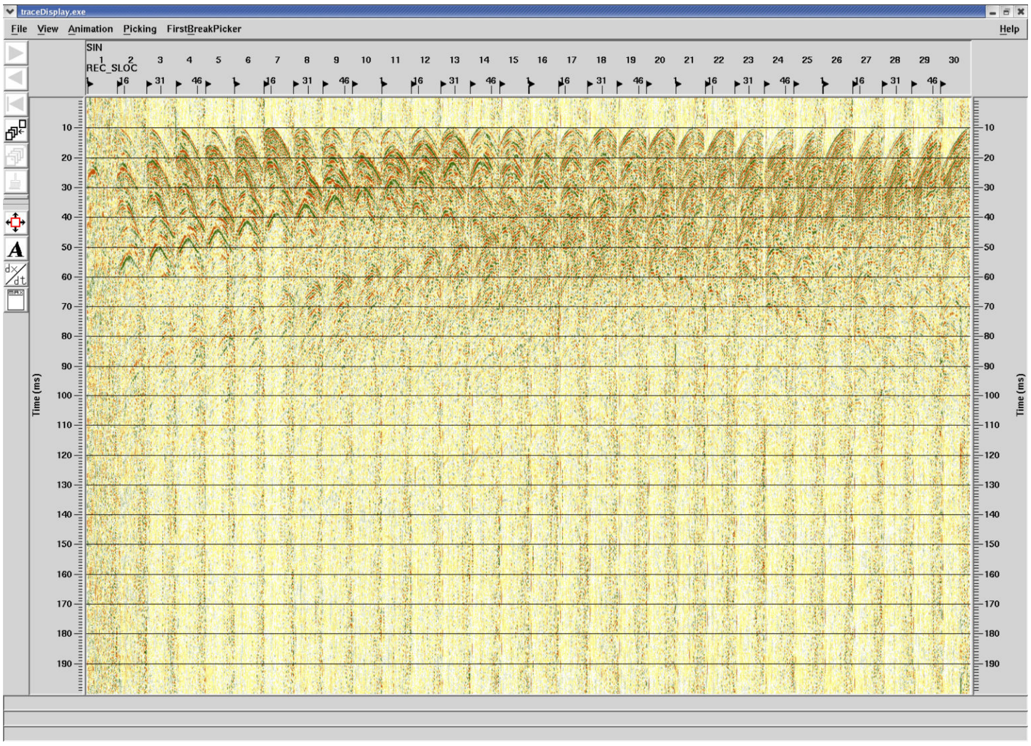

Fig 4-40 Original common source records of the crosswell survey

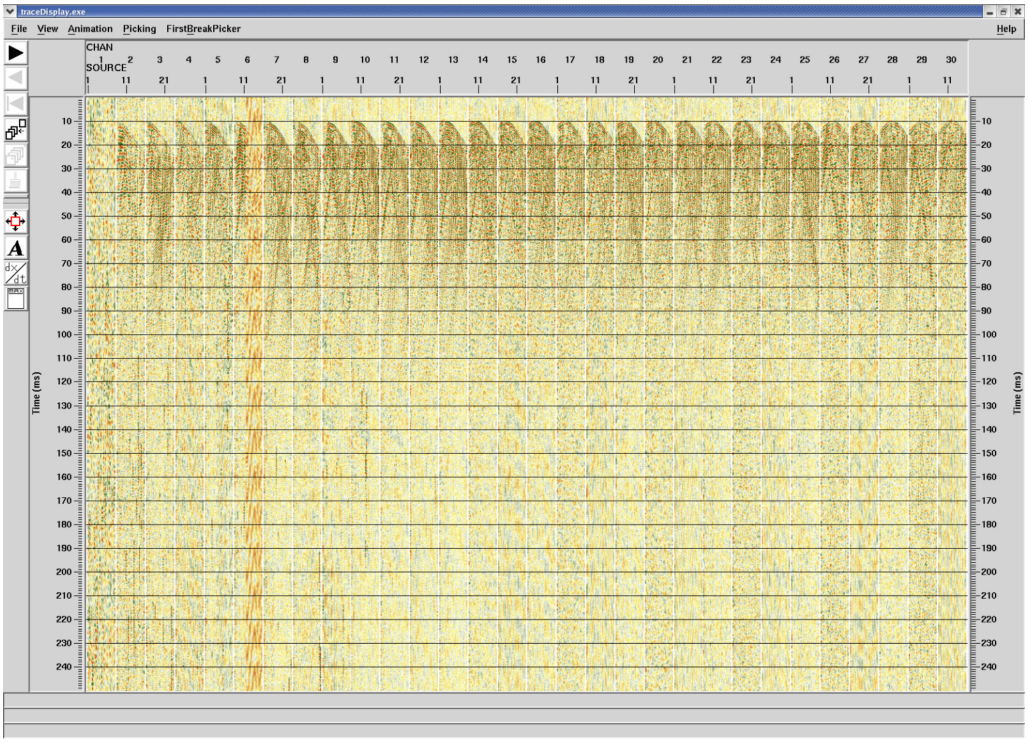

(a) Common receiver gather (receiver no. 1-30)

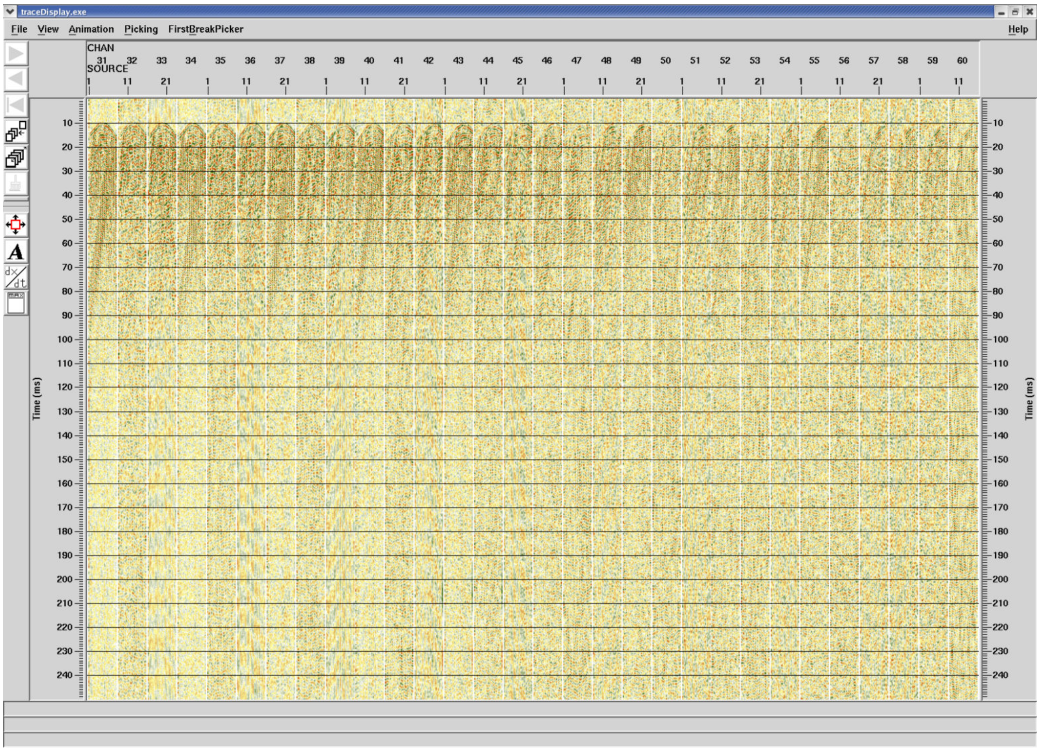

(b) Common receiver gather (receiver no. 31-60)

Fig 4-41 Original common receiver gather of the crosswell survey

The common receiver gathers at the receiver number 10 and 40 are shown in Fig 4-42. These waves have the velocity of water illustrated as blue dash lines in the figure and arise in the source hole. These are also considered to be caused by the fracture in the source hole.

If direct wave tomography is considered, these tube waves do not matter because the tube waves appear in later time than the direct waves. However, if the diffraction tomography or the reflection wave is exploited, the tube waves should be removed because these mask the other waves.

By the reciprocity theory of source-receiver, the results from the source gather data is equivalent to those from the receiver gather data. The processes are conducted with the receiver gather data not the source gather data, because the tube wave removal is easier in the receiver gather than in the source gather.

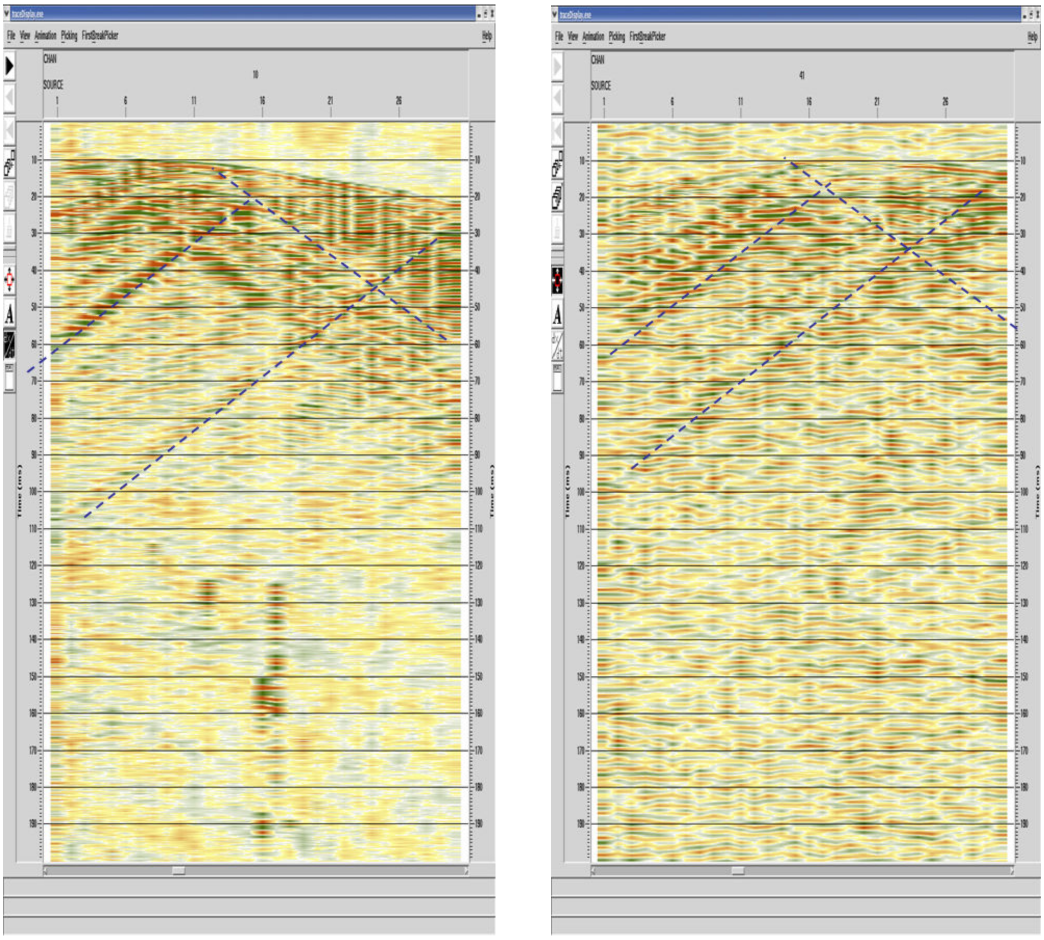

(a) Receiver no. 10 (b) Receiver no. 41

Fig 4-42 Examples of two common receiver gathers

Like the VSP case explained in the previous section, Spectrum analysis is applied and the examples of those are shown in Fig 4-43. The 60 Hz electrical noise are dominantly seen in case of the source number 10 (Fig 4-43(a)) and the low frequency noise caused by the construction and the small power supply for the crosswell survey are also seen around the frequency of 20Hz. Except for these noises, the signals are distributed from 100Hz to 550Hz and the dominant frequency of the receiver number 41 (Fig 4-43) is located about 420Hz.

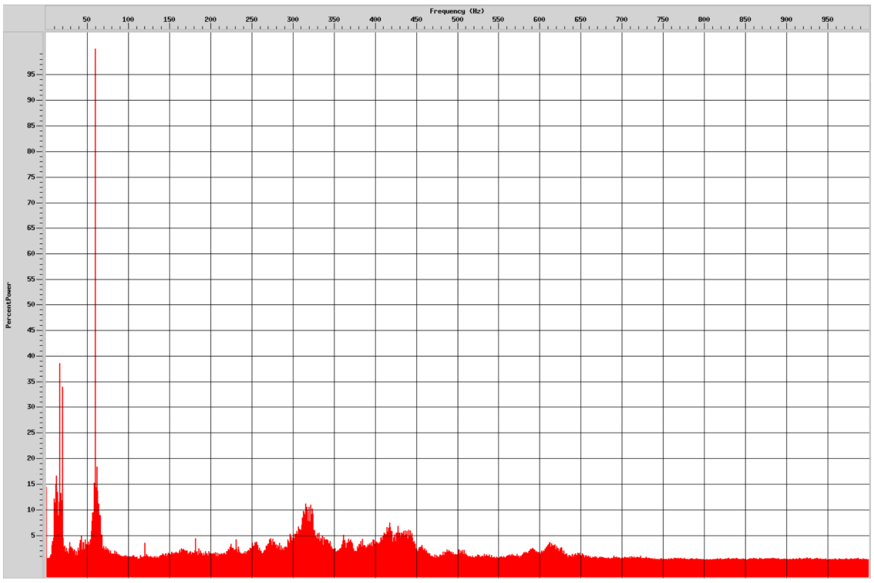

(a) Receiver no. 10

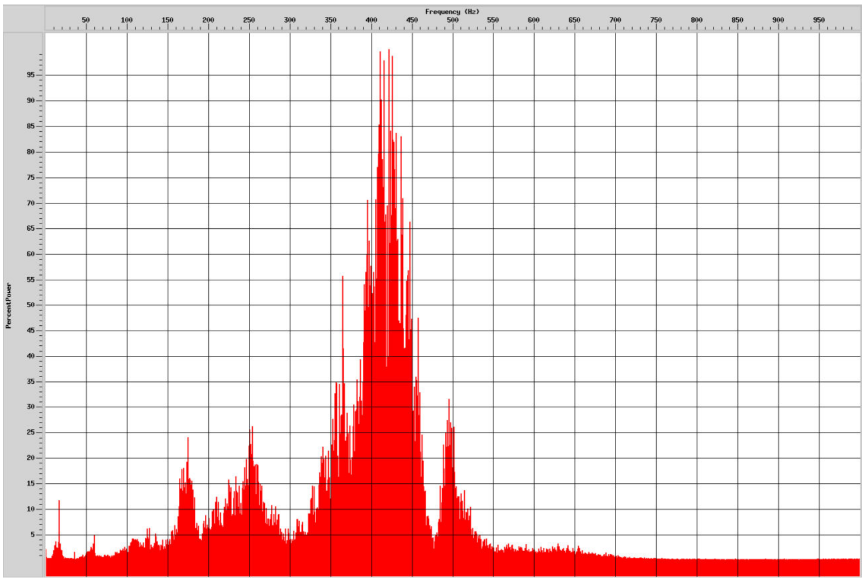

(b) Receiver no. 41

Fig 4-43 Examples of the spectrum analysis for the data of Fig 4-42

To know the characteristic of the tube waves, F-K analysis is applied and the examples of this application are illustrated in Fig 4-44. F-K analysis is performed after the band pass filter ranged 70Hz ~ 700Hz and muting before the direct waves. As seen from the results in Fig 4-44, the tube wave are aligned with the velocity of water, about 1500m/sec, as diamond shapes.

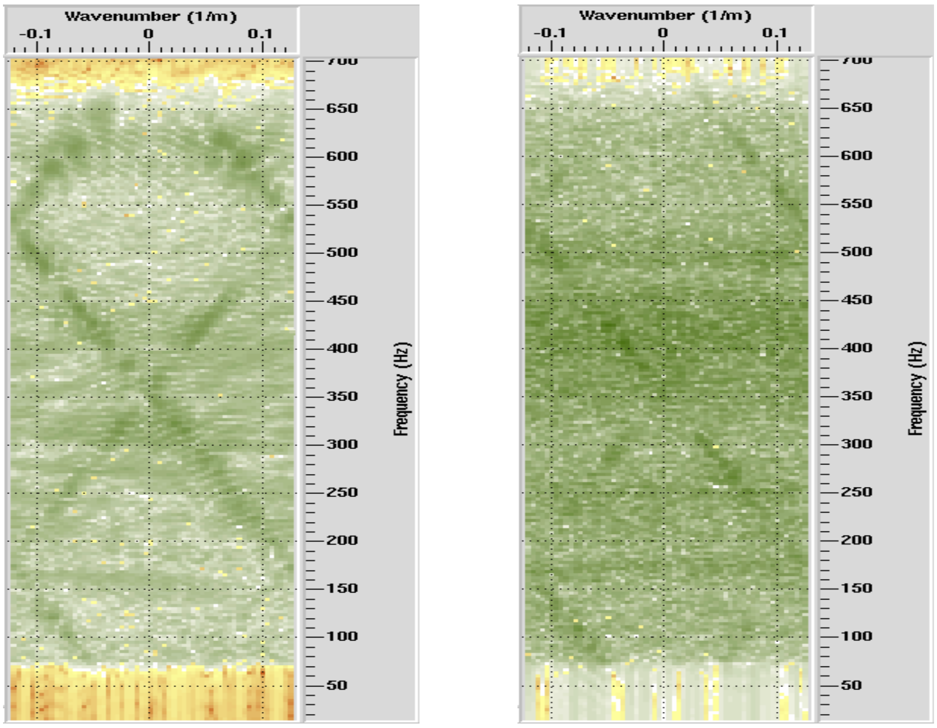

(a) Receiver no. 10 (b) Receiver no. 41

Fig 4-44 Examples of F-K analysis for the data of Fig 4-42

Velocity filter and Eingenvalue filter are applied to remove the tube wave and illustrated in Fig 4-45 and Fig 4-46 respectively. The results for the receiver number 10 and 41 gathers are also illustrated in Fig 4-47 and Fig 4-48. Eigenvalue filter results of Fig 4-46 and Fig 4-48 are followed by the up going wave filter.

As it is known about the velocity filter, almost all of the tube waves are removed, but still some remain. The reflection waves after velocity filtered are also hardly distinguishable from other waves. Only Eigenvalue filter results show similar results with velocity filter but the up-going filter is applied after Eigenvalue filter. Compared with velocity filter results (Fig 4-45 and Fig 4-47) and original records (Fig 4-41), the waves supposed as reflection waves are clearly seen and distinguishable in Eigenvalue filter results with up-going wave.

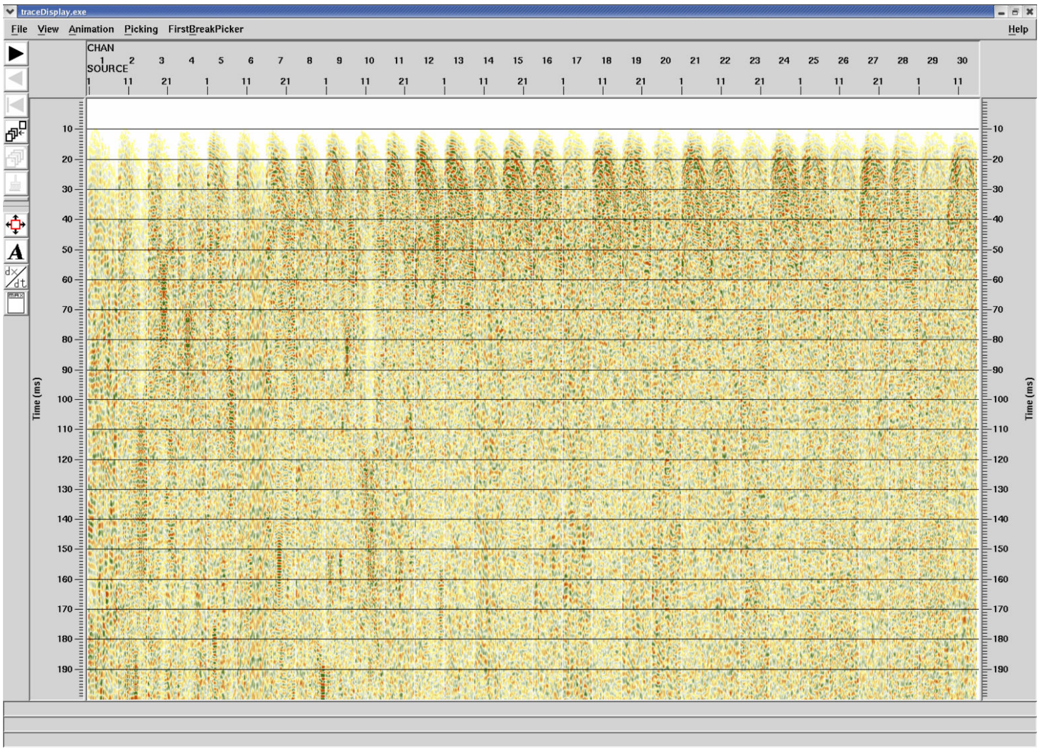

(a) Common receiver gather (receiver no. 1-30)

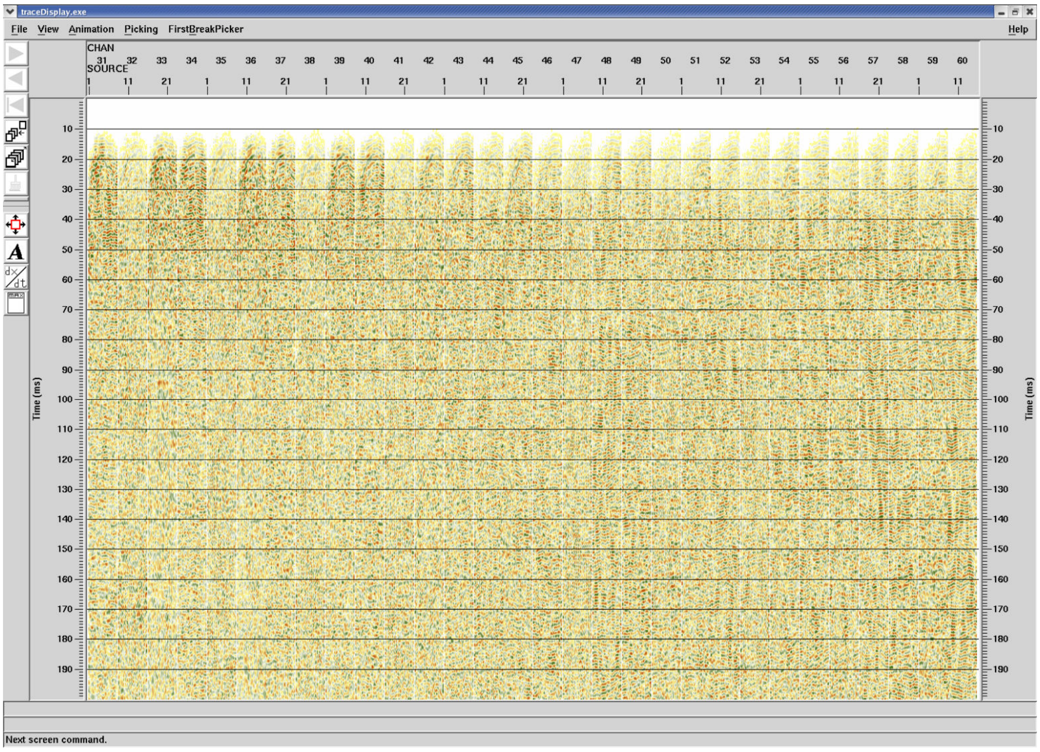

(b) Common receiver gather (receiver no. 31-60)

Fig 4-45 Velocity filter results for the data of Fig 4-41

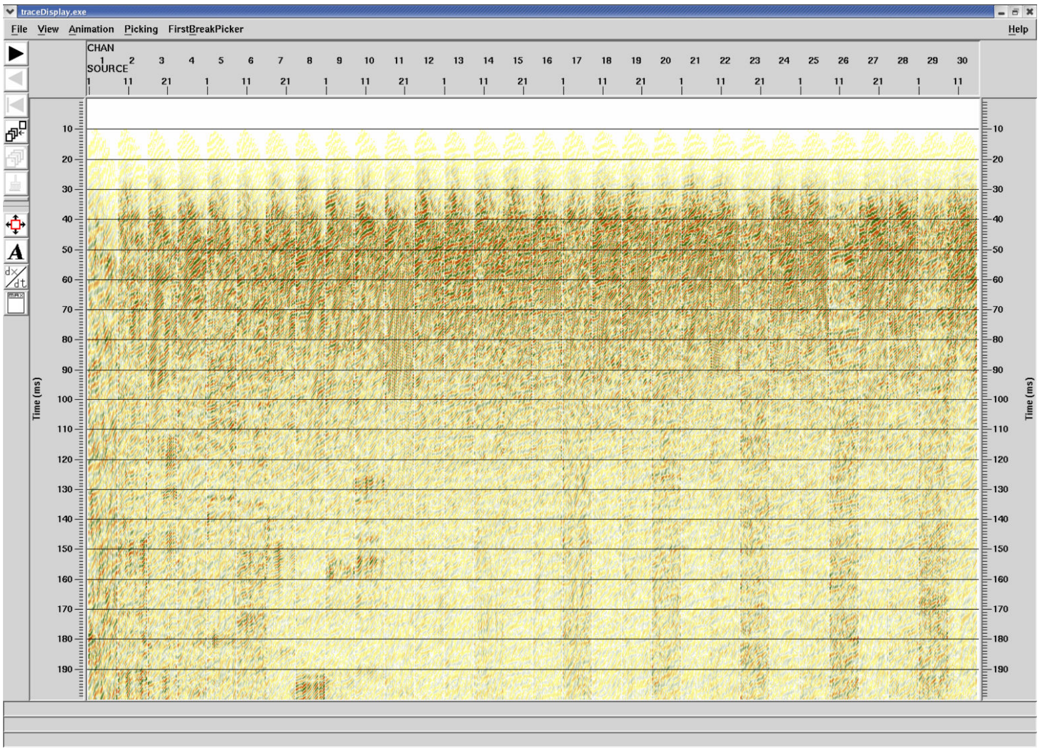

(a) Common receiver gather (receiver no. 1-30)

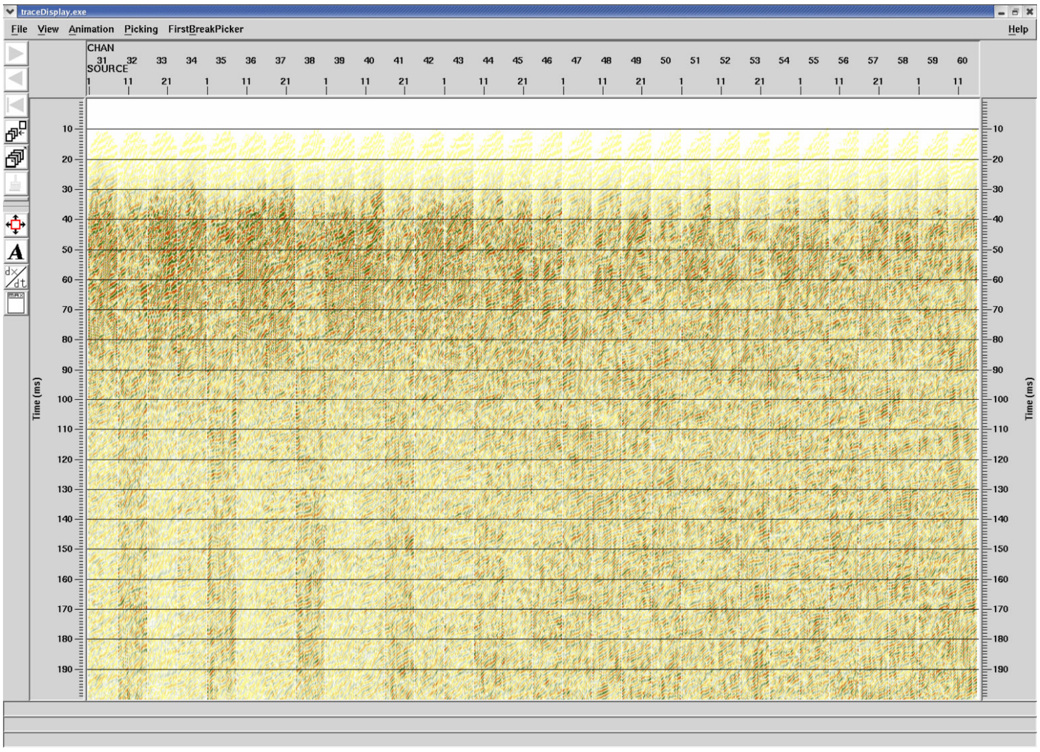

(b) Common receiver gather (receiver no. 31-60)

Fig 4-46 Eigenvalue filter and up going results for the data of Fig 4-41

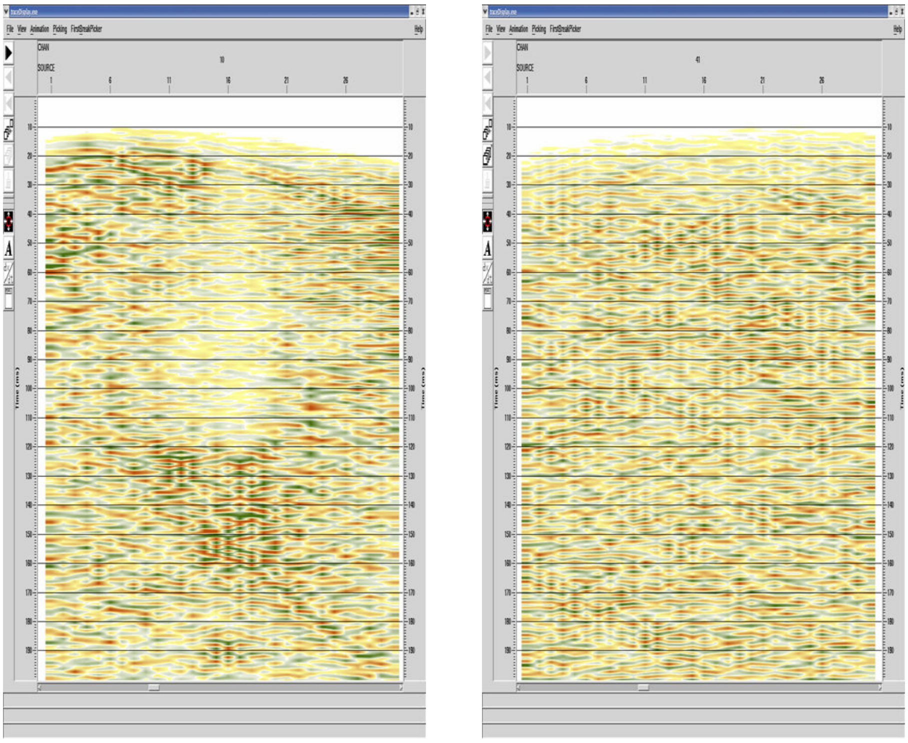

(a) Receiver no. 10 (b) Receiver no. 41

Fig 4-47 Examples of velocity filter results in Fig 4-45

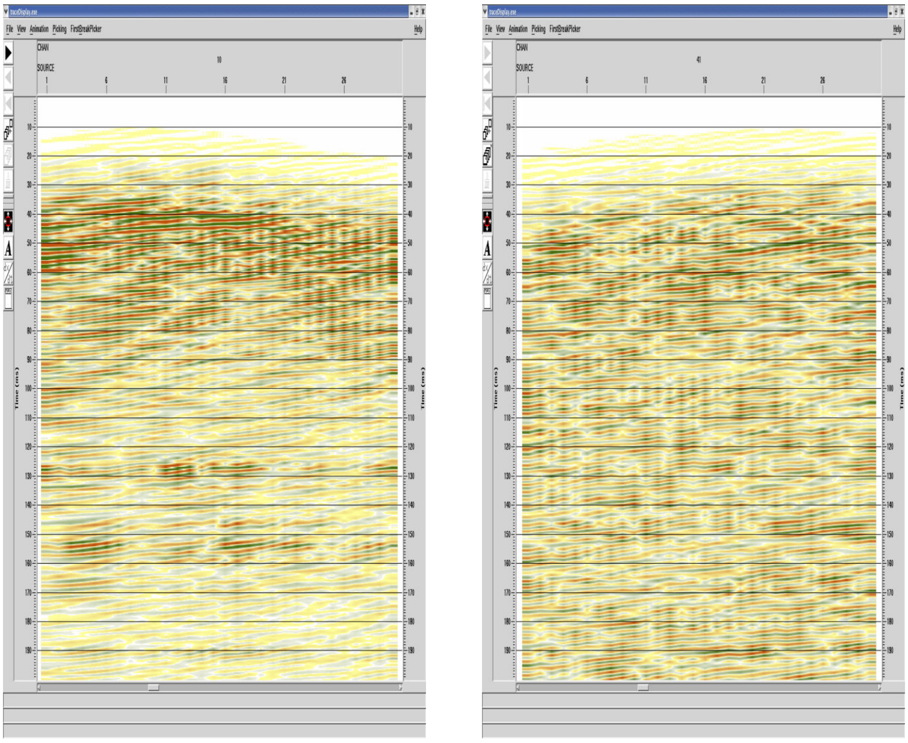

(a) Receiver no. 10 (b) Receiver no. 41

Fig 4-48 Examples of Eigenvalue filter results in Fig Fig 4-46

4.3.3. Imaging

The crosswell reflection imaging or migration is considered as the same way with VSP case because of the geometry of the source and the receiver. The geometry of receivers is same in both of the crosswell and VSP case but the geometry of sources is different, that is, the sources are located in the hole in case of the crosswell but set on the surface in case of VSP survey. In spite of the difference in the source geometry, the source geometry of the crosswell can be considered as the extension of that of VSP.

The results of Kirchhoff migration scheme, which is same to VSP case, using the Eigenvalue filtered data shown in Fig 4-46 are illustrated in Fig 4-49. Two vertical holes located in 100m and around 150m of the figures represent the source hole(right) and the receiver hole(left). Fig 4-46 (a) is the result for the receiver number 10(20m depth) data and Fig 4-46(b) is that for all depth data. The events not concerned with the reflection in one source results (Fig 4-49(a)) are decreased in all sources result (Fig 4-49) by the stacking effect, and the events related to the reflection are increased and enhanced.

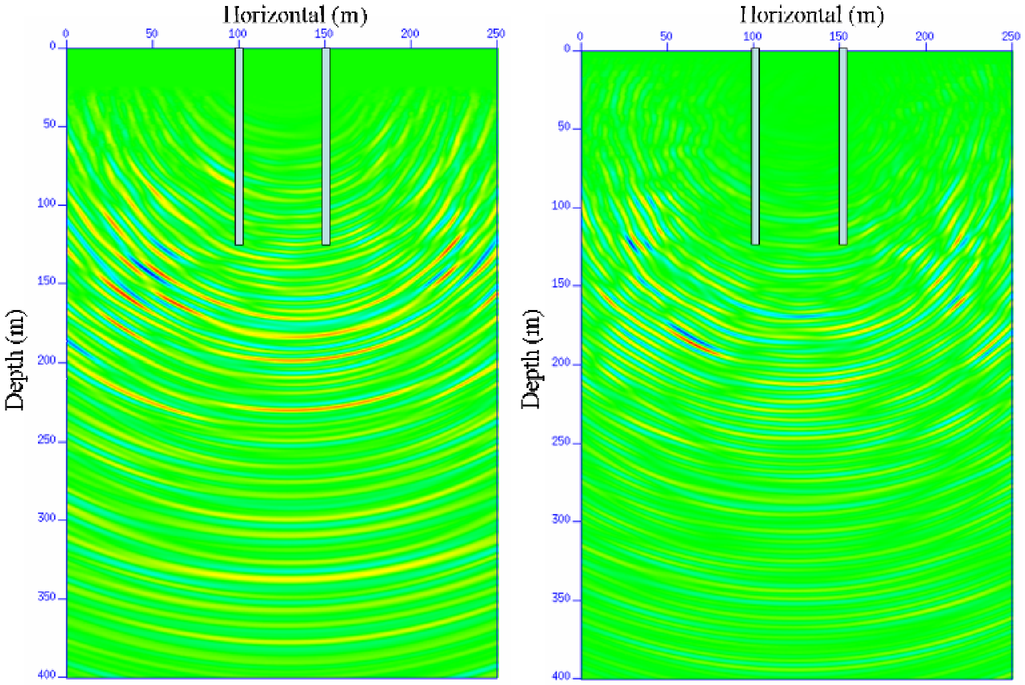

(a) One source at 20m depth (b) All sources

Fig 4-49 Kirchhoff migration results for the data shown in Fig 4-46

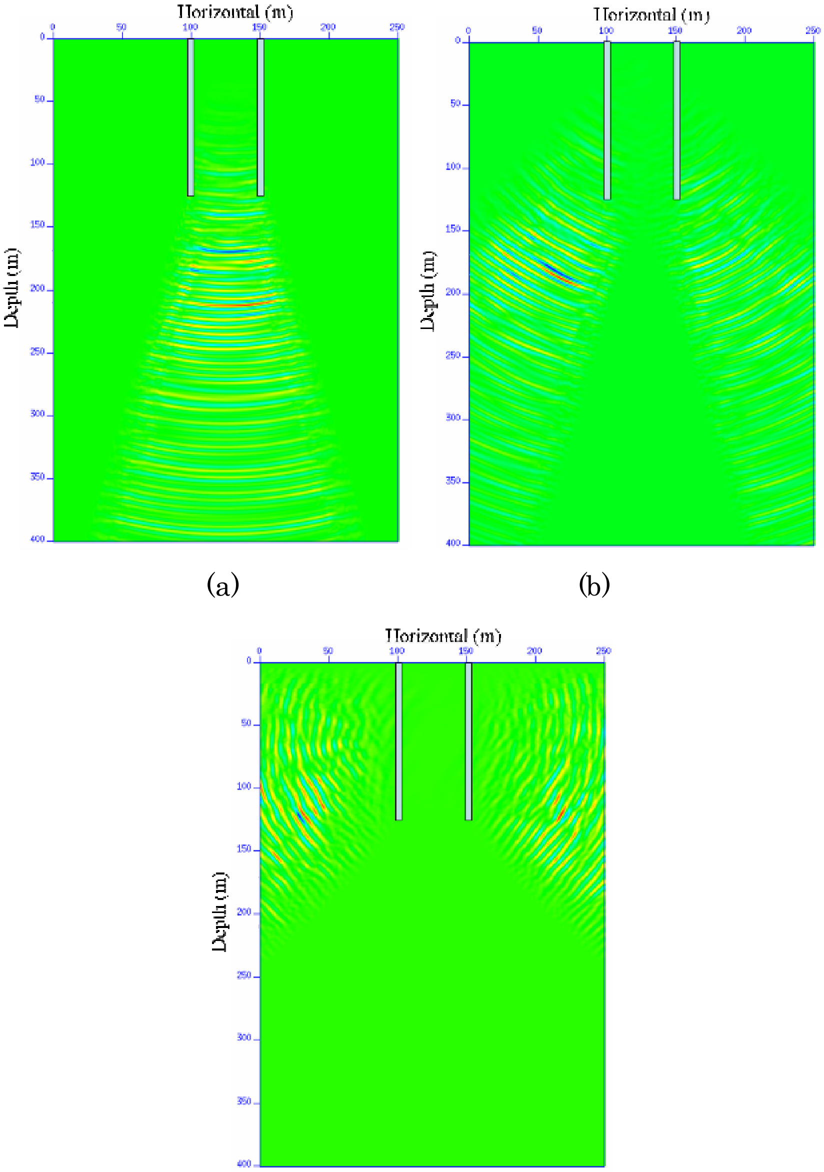

(a) (b)

(c)

Fig 4-50 Kirchhoff migration results for the data shown in Fig 4-46, (a) is the result of the reflection angle under 15 degree, (b) is the angle between 15 degree and 45 degree and (c) is the angle over 45 degree.

The imaging results illustrated in Fig 4-50, are achieved by dividing the reflection angle to three ranges- under 15 degree (a), 15degree ~ 45 degree (b) and over 45 degree (c). The reflection image of Fig 4-50(a) seen around 170m, 210m and 250m of depth, are supposed to be caused by the low dip fractures. The strongest image of Fig 4-50(b) is located in 180m of depth and in 60m of horizontal direction. In Fig 4-50(c), the well focused image is found around 120m of depth and 30m of horizontal. All of these are supposed to be associated with the fractures of the ground. The expected reflection planes through the imaging results are shown in Fig 4-51 and these are three low and almost near to horizontal planes and two dipping planes.

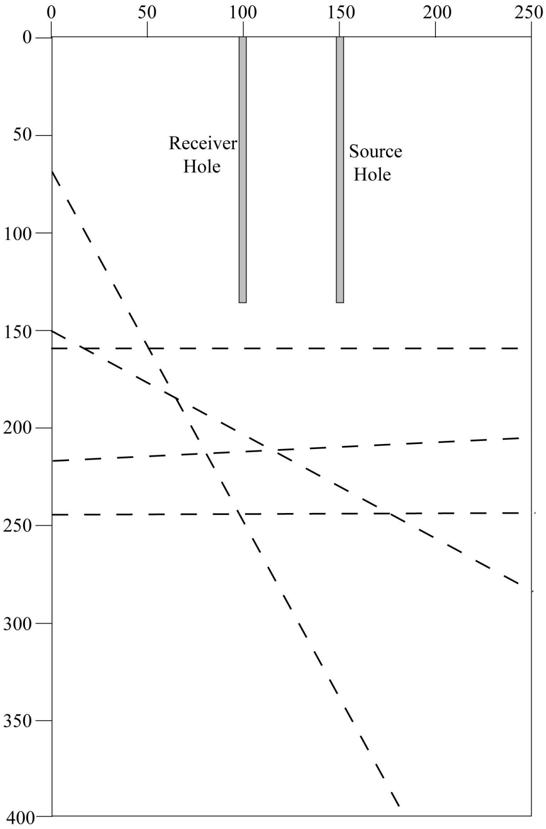

Fig 4-51 Expectation map of the reflection plane

The fractures distribution map is illustrated in Fig 4-52 and is reconstructed using the borehole logging data of the receiver hole. As seen in the fracture map, the dominant fractures are inclined from left to right, highly dip angle between 66 degree and 89 degree and concentrated in 50m depth of the receive borehole. The reflections of these fractures are hardly distinguished from the direct wave because these are too close to the receiver hole and too high dip angles. So, these reflections appear right after the direct wave and have similar shapes of travel time curve of the direct wave. As illustrated in original data (Fig 4-42) and filtered data (Fig 4-48), these waves are not distinguished from the others because they are mixed with the direct waves and the tube waves.

Two low dip angle reflections image of 210m and 250m depth (Fig 4-51) are matched with the fracture distribution map (Fig 4-52). The low dip angle image of 170m depth does not coincide with the fractures distribution map. However moderately dipped fractures about under 45 degree are expected from the fractures distribution map around 170m depth. As the construction of two shaft progresses, more information is available in deeper depth and this reflection is expected whether false or true image.

Two dipping reflection images in Fig 4-51 coincide with the fractures map of Fig 4-20, if little differences in depth and dip angle are acceptable.

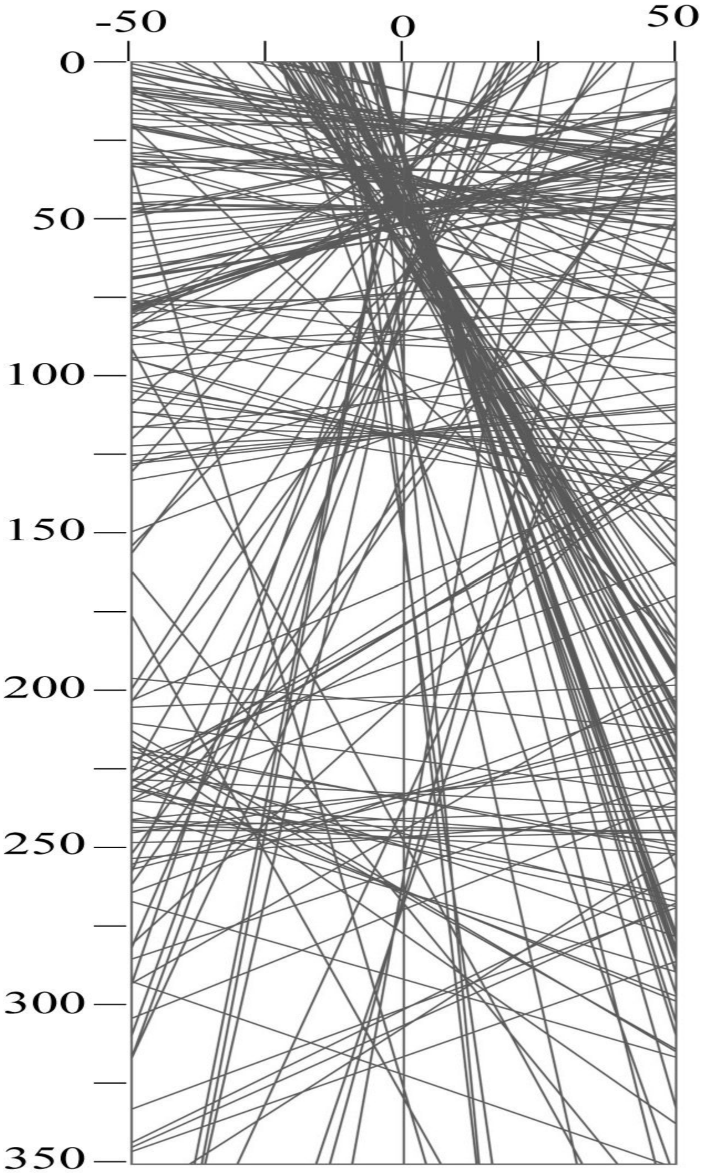

Fig 4-52 Fracture distribution map by the borehole logging data of the receiver hole which is located in the origin

4.3.4. Comparison of the field and simulation data in IP domain

Numerical Modeling

Numerical simulation is conducted for the model illustrated in Fig 4-51 but only two dipping reflectors are considered because the horizontal layer are easily distinguished from others. Geometry of the source-receiver in modeling is opposite to that of the field data acquisition, that is, the sources in numerical modeling are in the receiver holes of the field for the convenience of modeling. Because all processing are carried out in the receiver gather, the numerical results are also called as the receiver gather although those are the source gather for numerical modeling.

The numerical modeling results are illustrated in Fig 4-53 for total records and those of four sources are shown in Fig 4-54. Some numerical noises caused by boundary of the model are evident and the reflections by the surface are also seen after the direct wave which arrived at first. The reflection by two fracture planes are shown as arrows and the line arrows represent the higher dip angle of two fractures and the dashed line ones point the lower dip angle of those.

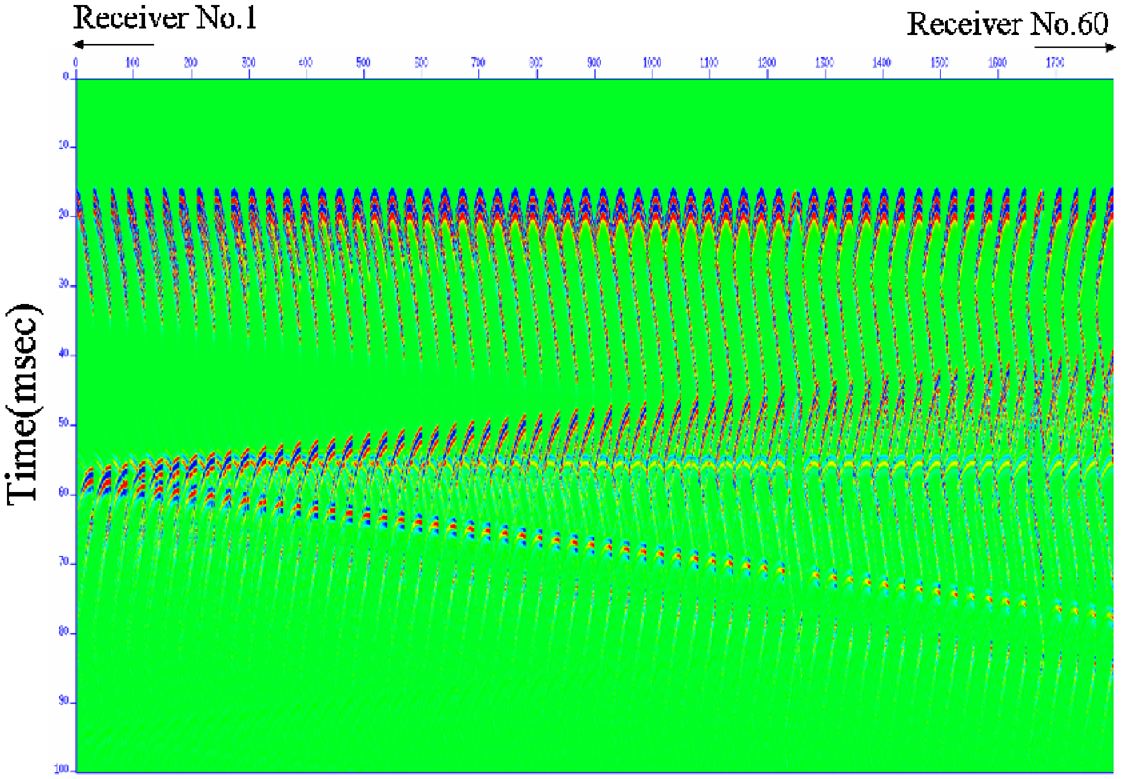

Fig 4-53 Numerical modeling results

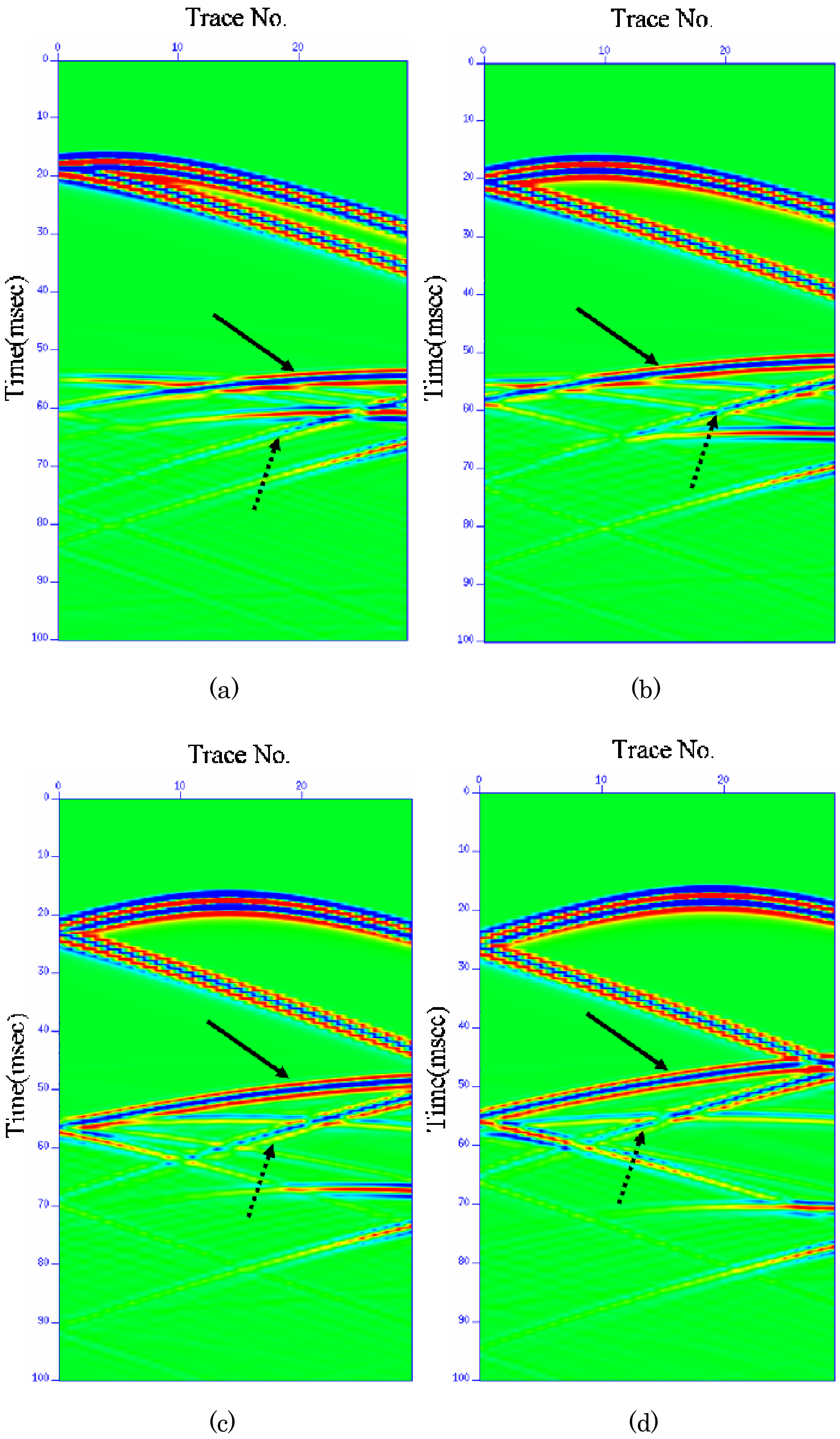

(a) (b)

(c) (d)

Fig 4-54 Examples of numerical results of four sources receiver number 10(a), 20(b), 30(c) and 40(d)

The numerical modeling result is compared and one example of receiver number 30 (the pre-processed wavelets) is illustrated in Fig 4-55. The lines shown in Fig 4-55 (a) are located at the same positions which are the reflections of the numerical result. As seen in the example, the reflection waves of the numerical modeling show agreeable result with the field data.

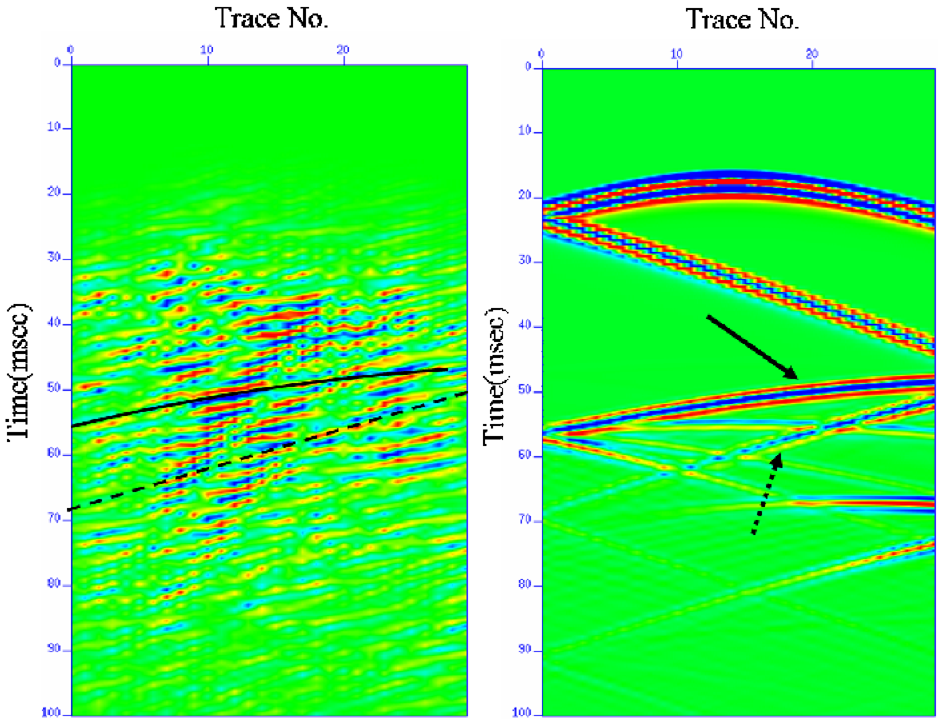

(a) (b)

Fig 4-55 Comparison of field data (a) and numerical data (b) for the receiver number 30

IP transform

To verify the imaging results, IP transform is applied to the both of the field data and the numerical modeling data. Four examples are shown From Fig 4-56 to Fig 4-59. The circles in the figures present the parts of the two reflections in IP domain and the line circles are those of the higher dip of two reflectors.

In the transform results of the numerical data, IPs of the direct waves are seen below the 200m of ρ, but those are not clear in field data because of the pre-processing. The IPs of two reflectors are not completely but considerably matched well with both of the numerical and field data

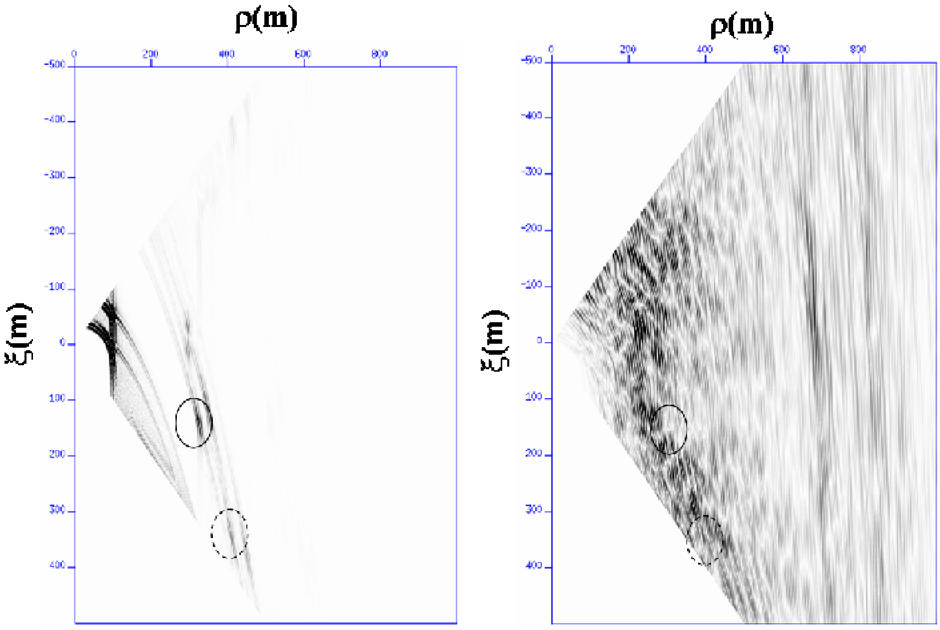

(a) (b)

Fig 4-56 IP transform results for numerical modeling data (a) and field data(b) of receiver number 10

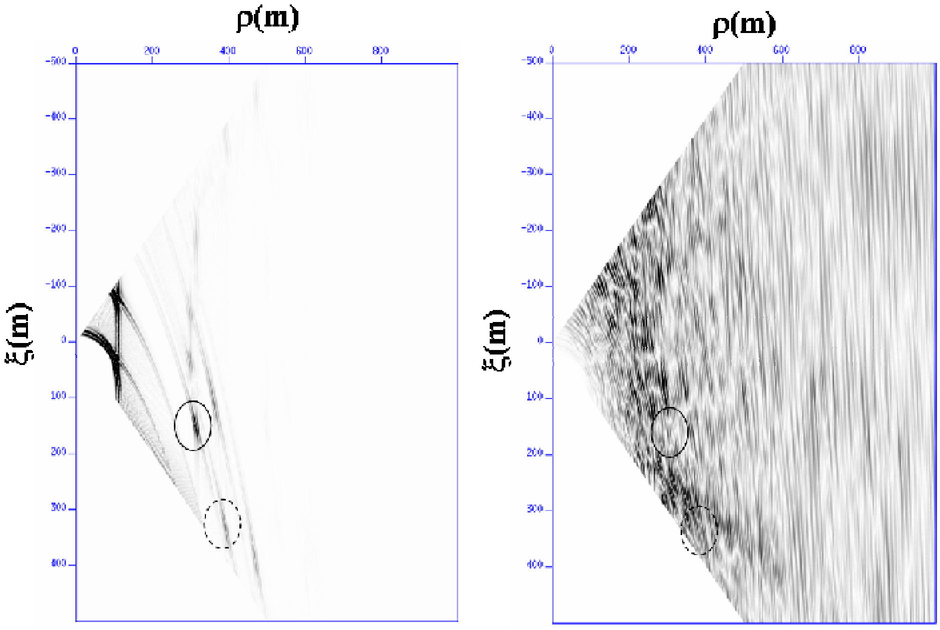

(a) (b)

Fig 4-57 IP transform results for numerical modeling data (a) and field data(b) of receiver number 20

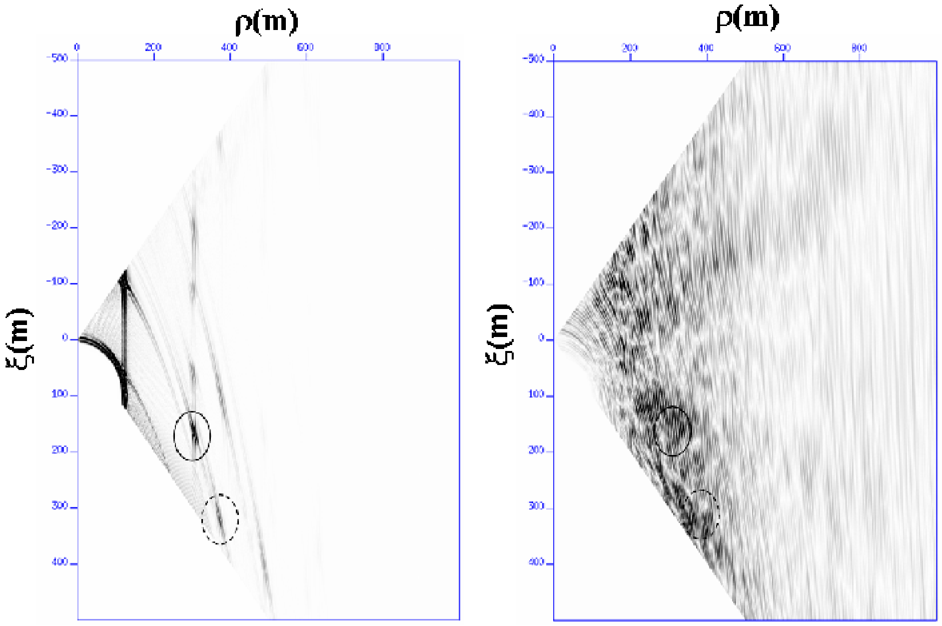

(a) (b)

Fig 4-58 IP transform results for numerical modeling data (a) and field data(b) of receiver number 30

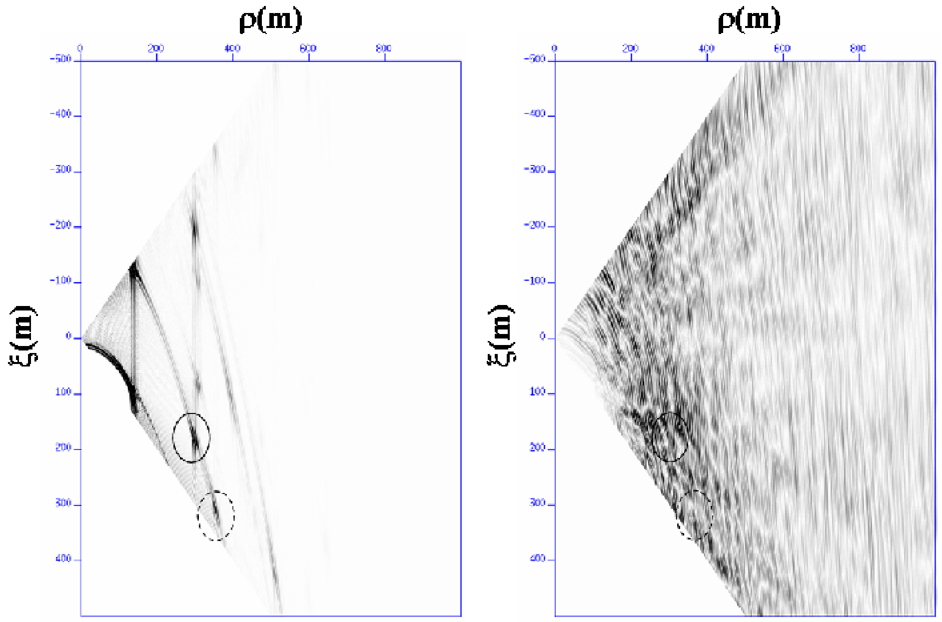

(a) (b)

Fig 4-59 IP transform results for numerical modeling data (a) and field data(b) of receiver number 40

4.3.5. Conclusion

The tube waves in a source well is dominant in crosswell data and it is frequently seen in borehole seismic data as shown in VSP data. The tube waves in a source well have same features of those in a receiver well but difference in the mechanism of generation.

Conventional data processing such as band-pass filter, tube wave remove, wave separation and imaging are applied to get final imaging of the ground. Although the agreeable result with the fracture distribution map is achieved however some difference of both are also seen, it is need to ensure the imaging result and numerical simulation is accomplished.

The model used for the simulation is reconstructed with the imaging results and the fractures distribution map. In comparison with the pre-processed field data and simulation data, it is hard to determine the reflection wave from others in the field data however it is possible in the numerical data. The comparison of reflection waves in IP domain gives a solution of the difficulty in data domain and ensures the validity of the reconstructed image by the conventional processing.

Chapter 5

Conclusion and Future Works

5.1. Conclusion

IP transform is derived from the Radon transform which convert the data of time-space domain to τ-p (intercept time-wave number) domain, but has different integral path. IP transform follows the hyperbolic path whereas Radon transform does the straight line. Therefore, Radon transform converts the hyperbolic reflection wave in time-space to the hyperbolic shape but different in τ-p domain. However, the IP transform converts the reflect waves to points in the IP domain by integrating according the hyperbolic paths

With this basic concept, this research is focused on understanding and distinguishing the characteristics and applicability of the IP transform. These works are done in numerical modeling data of some 2-D models and one 3-D model and three field data of 3-D RVSP, multi-offset VSP and crosswell survey. The results of these works are concluded and summarized as follows.

Application as filters in IP domain

The basic and most important characteristic of IP transform may be said to be concentration and enhancement of the reflection wave by the IP domain. This feature is confirmed through both synthetic and field data of various model and data acquisitions.

As shown in the numerical study of horizontal 2 layer model, the reflection and multiples are easily distinguished not only in original time-space domain but also in IP domain. Moreover, it is also seen that only reflection wave is reconstructed by the inverse transform after removing other multiples in IP domain.

Robustness to the noises should be referred as one feature of IP transform. Random noises like construction noise, human activity and so on which are common in filed data, are minimized and reduced in IP domain and these facts can be confirmed in both numerical and filed study.

Generally, it is difficult for the wave to separate the reflection of the different dip angles if these cross some points, even if they are clearly distinguishable in original records. Whereas they are easily separated in IP domain and therefore are reconstructed by the inverse transform. This filter named dip filter, are useful in field data if there are other information about dips or reflection waves are clear in original data.

Tube waves and multiples are commonly and frequently recorded in field survey as illustrated in VSP and crosswell survey, although many efforts are accomplished to remove or reduce them. F-K filter (a velocity filter) and Eingenvalue filter are generally used in pro-processing step to remove the tube waves. However this processing could be done in IP domain and better filter result will be expected by combination of those filters.

Generalized IP transform

As a special case of the receiver geometry of RVSP, that is, the receivers are located radially, numerical simulation and IP transform is accomplished. Two interesting properties of IP for the two dipping reflector of homogeneous model are found. Firstly, The IPs' ρ -distance from origin to the IP-of reflection does not change according to the radial receiver lines while ξ -apparent position of IP in the receiver line-change. Secondly, the vertical lines of ξ of each line meet one point and the common point lies on the perpendicular line of the strike of the reflector. With these properties, the new transform named generalized IP transform is considered. The IP transform is done in the line which receivers are located in, whereas the generalized IP transform convert the original data located on one line to the arbitrary line. Through IP transform to the arbitrary line(Generalized IP transform) for every line data, the IPs of the reflection are only accumulated when the arbitrary line is perpendicular to the strike of the reflector.

In the field application, it is hard to determine the vertical line to the reflector with only generalized IP transform results, because S/N ratio is slightly low in the original data and there exists too much faults of various dip angles and strikes. But, the generalized IP transform is accomplished to the line which is determined with other information like the borehole loggings, geological survey and surface reflection seismic survey.

Mid-point mapping

Conventional imaging method are originated and modified from the surface reflection seismic schemes such as VSP-CDP mapping and migration. Equal travel time imaging is also applied to the horizontal seismic profiling to get the final image of the tunnel but this scheme are one expanded type of the surface techniques.

As summarized the above and reported by Cosma (1996,2002), IP transform is useful to deal with the original data as filters, but wavelet reconstruction by the inverse transform is necessary to move to the next step and to get final imaging. However, the fact that the mid-point of the IP of reflection wave and the source is located on the reflector make new mapping scheme possible. Conventional imaging method image the reflection points whereas the mid-point mapping images the points lie on the reflector not reflection points. The mapping ability of the mid-point imaging is confirmed with numerical study. By comparison of migration scheme and the mid-point for the VSP field data, it is also found that those two results are agreeable although some differences between two results are also seen.

5.2. Future works

In this research, IP transform can be seen applicable not only in synthetic data but also in field. IP transform is mainly applied in homogeneous cases except for one 3-D RVSP case which is assumed 3-layer model. Other two field cases (VSP, Crosswell) are done in the hard rock so they can be considered as a homogeneous model. The characteristics of IP transform should be investigated in more complicated models and the calculation of ray path of those models should be developed.

3-D RVSP survey is planed in some steps of the Mizunami construction and it is expected to clarify the geometries of the fractures or the faults of the ground. As the field data are accumulated, it may be also valuable to apply the generalized IP transform again to determine the direction of the fracture.

The generalized IP transform of this research is applied to only RVSP case whose geometry of receivers are located radially but that is easily expandable and applicable to other geometry of sources or receivers like an epicenter array and a lattice grid array. The reason is because the generalized IP transform from one line to the other line could be converted to the transform form one point to the other line.

REFERENCES

Aki, K., and Richards, P. G., 1980, Quantitative seismology: W. H. Freeman and Co.

Anger, B. and Portenier, C., 1992, Radon Integrals. Boston, MA: Birkhäuser

Ashida,Y., Matsuoka, T., and Watanabe, T., 1998, Imaging algorithm for looking ahead prediction of near subsurface data: 4th International Symposium —*Fracture Imaging, Society of Exploration Geophysicists of Japan, Proceedings*,129–133.

Biondi, B. and Tisserant, T., 2004, 3D angle-domain common-image gathers for migration velocity analysis, *Geophysical Prospecting*, 52, 575-579.

Chen,G., Peron, J. F., and Canales, L., 2000, Rapid VSP-CDP mapping of 3-D VSP data: Geophysics, 65, 1631–1640.

Claebout, J.F., 1968, Synthesis of a layered medium from its acoustic transmission response: Geophysics, 33, 264-269.

Clayton, R., and Enquist, B., 1977, Absorbing boundary conditions for acoustic and elastic wave equations: Bull. Seis. Soc. Am., 67,1529-1540.

Cohen, J. K. and Stockwell, Jr. J. W., 2001, CWP/SU: Seismic Unix Release 35: a free package for seismic research and processing, Center for Wave Phenomena, Colorado School of Mines. Colorado School of Mines.

Cosma, C and Heikkinen, P., 1996, Seismic investigations for the final disposal of spent nuclear fuel in Finland: *J. Applied* Geophysics., 35, 151-157.

Cosma, C. and Enescu ,N., 2002, Multi-azimuth VSP methods for fractured rock characterization: ISRM 5th Workshop, Toronto, Canada,

Dewangan P. and Grechka, V., 2003, Inversion of multicomponent, multiazimuth walkaway VSP data for the stiffness tensor: Geophysics, 68, 1022-1031.

Dillon, P.B., 1988, Vertical seismic profile migration using the Kirchhoff integral, Geophysics, 53, 786-799.

Freire, S., Ulyrch, T., 1998, Application of singular value decomposition to vertical seismic profiling, Geophysics, 53, 778

Gulati, J. S., Stewart*z* R.R. and Parkin, J. M., 2004, Analyzing three-component 3D vertical seismic profiling dat: Geophysics, 69, 386–392.

Gray, S. H. and May W. P., 1994, Kirchhoff migration using eikonal equation traveltimes, Geophysics, 59, 810-817

Grechka, V. and Mateeva A., 2007, Inversion of P-wave VSP data for local anisotropy: Theory and case study: Geophysics, 72, D69-D79.

Hardage, B., 1983, Vertical Seismic Profiling, Part A: Geophysical Press

Hardage, B., 1992, Crosswell Seismology and Reverse VSP: Geophysical Press

Hilterman, F. J., 1982, Interpretive lessons from three-dimensional modeling: Geophysics, 47, 784-808

Hubral, P., Schleicher, J. and Tygel, M., 1996, A unified approach to 3-D seismic reflection imaging, Part I: Basic concepts: Geophysics, 61, 742-758.

Levander, A., 1988, Forth-order finite-difference P-SV seismograms: Geophysics, 53, 1425~1436.

Matsuoka, T. and Ishigaki, K., 2005, The evaluation of reflection seismic methods in the Mizunami Underground Research Laboratory Project (MIU Project), JAEA REPORT (Japanese)

McCrank, G., 2002, Summary of activities for the Mizunami Underground Research Laboratory Project (MIU Project) – A Final report on a JNC International Fellowship, JAEA REPORT

Mittet, R. and Hokstad, K., 1995, Transforming walk-away VSP data into reverse VSP data, Geophysics, 60, 968-977.

Moser, T. J., 1994, Migration using the shortest-path method: Geophysics, 59, 1110-1120

Sato, T., Mikake, S. Tamai, T., Imazu M. and Sakamaki, M,, 2003, Toward a Depth of 1,000 m from the Ground Surface -Construction Scheme of Mizunami Underground Research Laboratory: JNC Report (Japanese)

Sheriff, R. E., 1984, Encyclopedic dictionary of exploration geophysics: Soc. Explor. Geophys., Tulsa.

Shin, C., 1995, Sponge boundary condition for frequency-domain modeling: Geophysics, 60, 1870-1874.

Shiraishi, K., Matsuoka, T., Matsuoka, T., Tanoue, M. and Yamaguchi, S., 2007, Seismic interferometric imaging from a point source in the ground, Journal of Seismic Exploration, 15, 323-332.

Slawinski, M. A., Wheaton, C. J. and Powojowskiz M., 2004, VSP traveltime inversion for linear inhomogeneity and elliptical anisotropy: Geophysics, 69, 373-377.

Tygel, M., Schleicher, J. and Hubral, P., 1996, A unified approach to 3-D seismic reflection imaging, Part II: Theory: Geophysics, 61, 759-775.

Van Schaack, M., Harris, J. M., Rector, J. W., and Lazaratos, S. K., 1995, High resolution crosswell imaging of a West Texas carbonate reservoir, Part 2—Wavefield modeling and analysis: Geophysics, 60, 682–691.

Wapenaar, K., 2003, Synthesis of an inhomogeneous medium from its acoustic transmission response, Geophysics, 68, 1756-1759.

Wyatt, K. D., and Wyatt, S. B., 1981, Determination of subsurface structural information using the vertical seismic profile: 51st Ann. Internat. Mtg., Soc. Expl. *Geophys., Expanded Abstracts*, 1915–1549.

Yilmaz, O, 1987, Seismic data processing: Processing, inversion, and interpretation of seismic data.

Zhang, Q., Stewart, R. R., and Sun, Z., 1997, 3-D borehole seismic imaging and correlation—*A field experiment: 59th Annual Meeting, European Association of Geoscientists and Engineers*, E048.

Acknowledgments

It is lucky and important to have a chance of meeting Professor Toshifumi Matsuoka and receive his great guidance for three years. He shows me the way and the attitude as a researcher. He also point out my lack and foolish thing sometimes in strict way, sometime in kind and soft way. Without his considerable advices and patience, I couldn’t complete my works and make well in my life of Japan. I will keep in my mind his words as a pointer of my future life.

I should appreciate my committee members Professor Tsuyoshi Ishida and Hitoshi Mikada for their guidance and instruction. They willingly give me priceless time and efforts to read my thesis, understand my works and discuss opinions.

I am grateful to the persons of Japan Atomic Energy Agency, Korea Atomic Energy Research Institute for permitting to use and publish the data I thanks to the peoples of Dia Consultants and Nihon-Chikatansa. Especially, Mr. Masayoshi Tanoue and Dr Jongha Lee of Dia consultants and Mr. Yamaguchi, Mr. Ishigaki and Mr. Yamada share me nice experiences and give me concerns.

I owe my doctoral life in Kyoto to Asiageo Consultants, including my boss Katsumi Sakaguchi. They allow me to continue my academic works and to support to complete my doctoral course.

It is happy and joyful time to spend and share my student life with the people of Engineering Geology Lab. I couldn’t forget their help and kind manners for settling down in Japan and making various memories.

My dear and nice friends Youngtaek Hur, Jaehong Whang, Abbas Khayyer, Jaehoon Lee and Hyundon Kim, we share problems and help each other in hard time. I hope God bless their life of not only a research but a man.

My final thanks should be my mother and sister. I feel so sorry to make them worry about but they endure and support my challenge with a warm heart.